REPUBLIQUE ALGÉRIENNE DÉMOCRATIQUE ET POPULAIRE

Ministère de l'enseignement supérieur et de la recherche scientifique

UNIVERSITÉ AMAR TELIDJI LAGHOUAT

Faculté de Technologie-Département d'Électronique

THESE DE DOCTORAT EN SCIENCE

Présenté en vue de l'obtention du diplôme de doctorat en science
Option : Génie électrique

Thème

Structural, optical and electronic properties of organometal halide perovskites for photovoltaic applications

Présenté par

LAAMARI Mohammed El Mamoun

Devant le jury composé de:

Nom et Prénom	Grade	Etablissement d'origine	Qualité
LEFKAIER Ibn khaldoun	Professeur	Université de Laghouat	Président
GUEDDOUH Ahmed	M.C.A	Université de Laghouat	Examinateur
HELMAOUI Abderachid	Professeur	Université de Bechar	Examinateur
BOUHADDA Youcef	Directeur de Recherche	URAER de Ghardaia	Examinateur
CHEKNANE Ali	Professeur	Université de Laghouat	Directeur de thèse

Année universitaire 2019-2020

For

my wife, my family

and

my friends

Acknowledgments

First of all, I would like to thank my Doctorate supervisor, *Pro. Ali CHEKNANE*. He has put a lot of trust in me from the beginning and was always present to encourage, support and help me to overcome all the challenges I have faced during my doctoral studies.

I also would like to thank *Dr. Ali BENGHIA,* for his unconditional support and the fruitful time he has offered me.

Many thanks to « laboratoire de physique des matériaux » for providing me with CASTEP,v 8.0 license to do all the calculations.

I also would like to thank the members of my thesis jury committee: *Pr. Ibn Khaldoun LEFKAIER, Pr. Abderachid HELMAOUI, Dr. Ahmed GUEDDOUH* and *Research Director Youcef BOUHADDA,* for their decision to accept reviewing my doctorate thesis, their time to review my work and their constructive criticism.

Abstract

Organometallic perovskites (OMHP) based solar cells; with higher than 25% of power conversion efficiency (PCE), attract special attention. Using calculations, the first task confirms earlier experimental findings and determines optimal properties for the studied ($MAPbX_3$) (X=I,Br,Cl) family. Values of energy band gap, density of states, absorption coefficient α, refractive index n, dielectric constant ε and elastic constants c_{ij} of orthorhombic methylamunium lead halides ($MAPbX_3$) (X=I,Br,Cl) are all calculated using Density Functional Theory (DFT) method with generalized gradient approximation (GGA). The stiffness of ($MAPbX_3$) (X=I,Br,Cl) is investigated by calculating Young 's moduli E constants. Among the series, $MAPbI_3$ is the stiffest material with E_x=57.2 GPa. These perovskites are characterized by their tuned energy band gap: Eg $MAPbI_3$, $MAPbBr_3$, $MAPbCl_3$=1.626, 2.207 and 2.748 eV, respectively. They also exhibit a remarkable absorption coefficient ($\alpha_{MAPbX3}=10^5$ cm^{-1}) over a wide energy range, particularly in the visible spectrum [1.65–3.26 eV]. The anisotropy of optical properties ($MAPbX_3$) (X=I,Br) is proven in the near and middle ultraviolet [3.1–5 eV] energy band. In the second task, the effect of Ag and Cd atoms substitution on $MAPbI_3$ structural and optoelectronic properties is studied, based on the ab-initio DFT method. Properties of $MAPbI_3$ and $MAAB_xPb_{1-x}I_3$(B_x=$Ag_{0.17}$ or $Cd_{0.5}$) perovskites, in their orthorhombic phase, are described. The energy band gaps are calculated here with PBE-GGA and HSE06 methods. The $MAPbI_3$ is characterized by its high absorption coefficient over the visible spectrum [1.65–3.26 eV] compared to $MAAg_{0.17}$ $Pb_{0.83}$ I_3 ($\alpha=10^4$–$0.6\times10^5 cm^{-1}$), and $MACd_{0.5}$ $Pb_{0.5}I_3$ ($\alpha=1.5\times10^4$–$0.4\times10^5 cm^{-1}$). Low anisotropic electron and hole effective masses are found for all compounds in the range of 0.043 m_0-0.188 m_0. The anisotropy in optical properties for $MACd_{0.5}$ $Pb_{0.5}I_3$, such as the α, ε and n, is noticed. Enhancement in refractive index n of $MAAg_{0.17}$ $Pb_{0.83}I_3$ is also observed. The calculated values for n are 2.90, 2.75 and 2.00 for $MAAg_{0.17}$ $Pb_{0.83}I_3$, $MAPbI_3$ and $MACd_{0.5}Pb_{0.5}I_3$, respectively, at 2.5 eV energy peak value. The values for κ are 1.4, 1.8, and 1.2 for $MAAg_{0.17}$ $Pb_{0.83}I_3$, $MAPbI_3$ and $MACd_{0.5}Pb_{0.5}I_3$, respectively, at 3.5 eV energy peak value.

Keywords: Perovskites,DFT,Optical absorption,Band gap tuning,Stifness, Effective mass.

ملخص

الخلايا الشمسية القائمة على المركبات العضوية المعدنية الهالوجينية ذات بنية البيروفسكايت (OMHP) جذبت انتباها خاصا لامتلاكها على كفاءة تحويل الطاقة (PCE) عالية وصلت إلى 25 ٪. باستخدام الحسابات، المهمة الأولى هي تحديد الخصائص المثالية لعائلة ($MAPbX_3$) (X = I، Br، Cl) . بتأكيد النتائج التجريبية السابقة حيث يتم حساب جميع قيم فجوة نطاق الطاقة ، وكثافة الحالات ، ومعامل الامتصاص α ، ومؤشر الانكسار n ، وثابت العزل الكهربائي ε وثوابت المرونة cij للمركبات ($MAPbX_3$) (X = I، Br، Cl) باستخدام نظرية دالية الكثافة الوظيفية (DFT) مع طريقة تقريب التدرج المعمم (GGA) . تم التدقيق في حساب صلابة المركبات ($MAPbX_3$) (X = I، Br، Cl) من خلال حساب معامل يونغ. من بين المركبات ، يعد $MAPbI_3$ الأكثر صلابة ب E_x = 57.2 GPa . تتميز هذه المركبات بفجوة نطاق طاقة متكيفة: على سبيل المثال $MAPbI_3$ $MAPbBr_3$ و $MAPbCl_3$ لها و 1.626 و2.207 و 2.748 eV ، على التوالي. كما أنها تظهر معامل امتصاص ملحوظ ($\alpha_{MAPbX3} = 10^5$ سم$^{-1}$) على مدى واسع من الطاقة خاصة الطيف المرئي [1.65–3.26 الكترون فولت]. ثبت تباين الخواص البصرية (X = I) ($MAPbX_3$، Br) في نطاق الطاقة القريب والأوسط فوق البنفسجي [3.1–5 الكترون فولت]. في المهمة الثانية ، تمت دراسة تأثير استبدال ذرات Ag و Cd على الخواص البنيوية والإلكتروضوئية على $MAPbI_3$ ، استنادًا إلى طريقة DFT . يتم وصف خصائص $MAPbI_3$ و $MAAB_xPb1_xI_3$ ($B_x = Ag_{0.17}$ $Cd_{0.5}$)، في الطور orthorhombic الخاص بها . يتم حساب الفجوات في شريط الطاقة هنا باستخدام طرق PBE-GGA و HSE06 . يتميز $MAPbI_3$ بمعامل امتصاص عالي في الطيف المرئي [1.65–3.26 eV] مقارنةً بـ المركبات الأخرى. تم العثور على كل فعالة صغيرة و متباينة لجميع المركبات. لوحظ تباين الخواص البصرية لـ $MACd_{0.5}Pb_{0.5}I_3$ ، مثل α و ε و n. لوحظ أيضًا ارتفاع في معامل الانكسار n $MAAg_{0.17}Pb_{0.83}I_3$. القيم المحسوبة لـ n هي 2.90 و 2.75 و 2.00 لـ $MAAg_{0.17}Pb_{0.83}I_3$ و $MAPbI_3$ و $MACd_{0.5}Pb_{0.5}I_3$، على التوالي عند ذروة الطاقة 2.5 الكترون فولت. قيم κ هي 1.4،1.8 و 1.2 لـ $MAAg_{0.17}Pb_{0.83}I_3$ و $MAPbI_3$ و $MACd_{0.5}Pb_{0.5}I_3$ على التوالي عند الذروة 3.5 الكترون فولت.

كلمات مفتاحية: بيروفسكايت، نظرية دالية الكثافة الوظيفية (DFT) ، الامتصاص الضوئي ، نطاق الطاقة ،صلابة، كتلة فعالة.

Résumé

Les cellules solaires à base de pérovskites organométalliques (OMHP); avec plus de 25% du taux de conversion d'énergie (PCE), attirent une attention particulière. En utilisant le calcul, la première tâche est de confirmer les résultats expérimentaux antérieurs et déterminer les propriétés optimales de la famille étudiée ($MAPbX_3$) (X=I, Br, Cl). Les valeurs de la largeur de bande interdite, de la densité d'états, du coefficient d'absorption α, de l'indice de réfraction n, de la constante diélectrique ε et des constantes élastiques cij des valeurs de la famille orthorhombiques ($MAPbX_3$) (X=I, Br, Cl) sont toutes calculées à l'aide de la théorie de la fonctionnelle de la densité (DFT) avec l'approximation du gradient généralisé (GGA). La rigidité de ($MAPbX_3$) (X=I, Br, Cl) est étudiée en calculant les constantes de module de Young E. Parmi les matériaux de la série, le $MAPbI_3$ est le matériau le plus rigide avec E_x = 57.2 GPa. Ces perovskites sont caractérisées par leurs bandes interdites ajustables: par exemple, $MAPbI_3$, $MAPbBr_3$, $MAPbCl_3$ = 1,626, 2,207 et 2,748 eV, respectivement. Ils présentent également un coefficient d'absorption remarquable (α_{MAPbX3}=105 cm^{-1}) sur une large bande d'énergie, en particulier dans le spectre visible [1,65–3,26 eV]. L'anisotropie des propriétés optiques ($MAPbX_3$) (X=I, Br) est démontrée dans la bande d'énergie ultraviolette proche et moyenne [3,1–5eV]. Dans la deuxième tâche, l'effet de la substitution d'atomes Ag et Cd sur les propriétés structurales et optoélectroniques de $MAPbI_3$ est étudié à l'aide de la méthode DFT. Les propriétés des pérovskites $MAPbI_3$ et $MAAB_xPb_{1-x}I_3$ (B_x=$Ag_{0.17}$ ou $Cd_{0.5}$), dans leurs phases orthorhombiques, sont décrites. Les bandes interdites d'énergie sont calculées avec les méthodes PBE-GGA et HSE06. Le $MAPbI_3$ se caractérise par son coefficient d'absorption élevé dans le spectre visible [1,65-3,26eV] par rapport à $MAAg_{0,17}Pb_{0,83}I_3$ (α=$0,6\times10^4$–$10^5 cm^{-1}$) et $MACd_{0,5}$ $Pb_{0,5}I_3$ (α=$1,5\times10^4$–$0,4\times10^5 cm^{-1}$). Tous les composés ont des masses effectives anisotropes et petites pour les électrons et les trous de l'ordre 0,043m_0-0,188 m_0. L'anisotropie des propriétés optiques pour $MACd_{0.5}Pb_{0.5}I_3$, telles que α, ε et n, est remarquée. Une augmentation de l'indice de réfraction n de $MAAg_{0.17}Pb_{0.83}I_3$ est également observée. Les valeurs calculées pour n sont respectivement 2,9, 2,75 et 2 pour $MAAg_{0,17}Pb_{0,83}I_3$, $MAPbI_3$ et $MACd_{0,5}Pb_{0,5}I_3$ à une valeur crête de 2,5 eV. Les valeurs de κ sont 1,4, 1,8 et 1,2 pour $MAAg_{0,17}Pb_{0,83}I_3$, $MAPbI_3$ et $MACd_{0,5}Pb_{0,5}I_3$, respectivement, à une valeur crête de 3.5 eV.

Mots clés: Perovskites, Absorption, DFT, bandes interdites agiles, Rigidité, Masse effective.

Table of Contents

List of Abbreviations

OMHP : Organo-Metallic Halide Perovskite.

PSC: Perovskite Solar Cell.

PCE: Power Conversion Efficiency.

PV: Photovoltaic.

ETM: Electron Transporting Material.

HTM: Hole Transporting Material.

ITO: Indium-Doped Tin Oxide.

FTO: Fluorine-Doped Tin Oxide.

DSSC: Dye-Sensitized Solar Cell.

HOMO: Highest Occupied Molecular Orbital

LUMO: Lowest Unoccupied Molecular Orbital.

LED: Light Emitting Diode.

UV: Ultraviolet.

NIR: Near Infrared.

RH: Relative Humidity.

List of Figures

List of Tables

INTRODUCTION

Introduction

Demand of electricity in Algeria knows historic and unprecedented rates regarding to the industrial activity growth and habitation power supply. For these reasons, as our country is a gas exporter, the liberation of the local need to gas based electricity and avoiding the global warming emissions due to energy production are urgent priorities.

Solar energy uses in Algeria still have a bashful presence because of the expensive cost of mono-crystalline and multi-crystalline silicon wafer based PV technologies that contribute to 94% of solar energy production over the world. This fact opens new material opportunity on the horizon to investigate high solar cells conversion efficiency, long term stability and clean energy.

Organometallic halide perovskites PV (OMHP- PV) are among the best materials, with a high power conversion efficiency that surpassed 25% for single junction perovskite solar cells. This remarkable result sets great expectations for perovskite to enter the market in the coming years. OMHP -PV have a prosperous future and became one of the front runners emerging PV absorbers as they have interesting optoelectronic features, such as high absorption coefficient, tunable band gap energy in the visible range, long range electron-hole transport lengths and high carrier mobility. They are cheap to produce and easy to manufacture.

This work comes up with the idea of addressing a single junction perovskite solar cells project at the “laboratoire des semi-conducteurs et materiaux fonctionnels, universite de Laghouat”. The first step of this project deals with the knowledge of the peculiar physics and chemistry of the perovskite layer for solar energy applications.

Methylamunium lead iodide ($MAPbI_3$) is one of the striking absorber materials, although its main drawback rises when it degrades and decomposes in the presence of elevated moisture, temperature and illumination which hampers its performance and stability inside the PSC. So, finding and investigating its alternatives or even pseudo alternatives require firstly understanding deeply the structural, optoelectronic and mechanical properties of PMHP materials. In order to design high performances PSC,

these tasks are of importance as the perovskite is an adhesive and strongly dependent active layer with respect the other layers constituting the PSCs.

$MAPbI_3$ of ABX_3 perovskite structure can change its structural phase from orthorhombic to tetragonal and then to cubic one under increased temperatures. The best approach to investigate OMHP material as absorber layers in photovoltaic systems is to study and investigate the structural, electronic, optical and mechanical properties of $MAPbI_3$ and then to broaden the examination to other organometallic perovskites. These last perovskites have been designed carefully through total or partial substitution in the ABX_3 sites (A, B, X) and should respect a strict formability and phase conditions such as the tolerance and the octahedral factors t, μ respectively, they also should offer attractive optoelectronic properties as well as more stability regarding the soft nature of $MAPbI_3$.

The thesis is titled structural, optical and electronic properties of organometal halide perovskites for photovoltaic applications. It deals with the outline of OMHP materials and OMHP solar cell in one hand and the results obtained from CASTEP software simulation in another hand. This dissertation is organized into four chapters.

The first one expresses the state of art of perovskites materials. It presents firstly the historical progress of the perovskite solar cell (PSC). Then, it introduces the structure, the formability and the phase transition of such organometal halide perovskites (OMHP). After that the chapter describes the effect of doping in each ABX_3 site on the perovskite material opto-electronic properties and also on the power conversion efficiency (PCE). Next, the chapter presents the fundamental PCS architectures used in the photovoltaic systems and describes the functioning principles of such PSC. Then, the important perovskites synthesis methods are described. It deals also with other applications concerning the perovskite materials. Chapter one reveals the great problems confronting the large scalable PSCs commercialization. It also contains the state of art of PSCs stability issues where detailed argumentation of the PSC system degradation is presented. For instance, the effect of moisture, temperature, UV light, intrinsic perovskite atomic composition, fabrication technique and the other layers materials effects. Lastly, the most reported PSC stability approaches are cited.

The next chapter is devoted to the important basics of DFT method. The main approximations to derive the Khon-Sham equations are discussed. Then, the concept of electronic density in those equations is introduced. Moreover, the most recent exchange-correlation functionals are presented. Finally, some of the newest studies on DFT investigation of organo-metallic halide perovskites electronic properties are cited.

The third chapter is a result and discussion chapter, titled: optimized opto-electronic and mechanical properties of orthorhombic methylamunium lead halides ($MAPbX_3$) (X=I, Br and Cl) for photovoltaic applications. There are the lattice parameters and the elastic constants of orthorhombic ($MAPbX_3$) (X=I, Br and Cl) to begin with, then electronic band gap, density of states electronic charge distribution and Mullikan population analysis are all calculated. After that, obtained absorption coefficients, dielectric constants and refractive indices are eventually introduced.

The last chapter is also a resulting one, titled: effect of metal (Ag and Cd) substitution on methylammonium lead iodide perovskite $MAPbI_3$ optoelectronic properties for photovoltaic applications. There are usually the lattice parameters of orthorhombic ($MABI_3$) (B=Pb, $Ag_{0.17}Pb_{0.83}$, $Cd_{0.5}Pb_{0.5}$) to start with, next the result of electronic band gap, density of states electronic charge distribution and Mullikan population analysis as well as the effective masses are presented. After that, absorption coefficients, dielectric constants and refractive indices are lastly calculated.

CHAPTER 1

State of the Art of Perovskite Materials and their Stability Issues

1. Introduction

Until now, monocrystalline and multicrystalline silicon wafer based PV technologies dominate the world solar energy market with a contribution of about 94%. The installed capacity of photovoltaics (PV) expected to reach 900 GWp in 2021 [1]. In the meantime, organometallic halide perovskites PV (OMHP- PV) show unprecedented rapid improvement power conversion efficiency (PCE) of 25.2 % in very short time in comparison to the other existing data results of established PV technologies, which needed much time to achieve similar efficiency advances [2]. In fact, (OMHP- PV) thin film technologies exhibit promising benefits compared to wafer technology; including high efficiency thinner absorber layers and many opportunities for low cost production and module manufacturing.

In this first chapter, a state-of-the-art of perovskites materials is presented. Firstly, it mentions a historical progress of the perovskite solar cell (PSC). Then, it introduces the structure, the formability and the phase transition of such organometal halide perovskites (OMHP). After that, the chapter describes the effect of doping in each ABX_3 site on the perovskite material opto-electronic properties and also on the power conversion efficiency (PCE). Next, the chapter presents the fundamental PCS architectures used in the photovoltaic systems. Then, the important perovskites synthesis methods are cited. It deals also with other applications concerning the perovskite materials. In the end, the chapter reveals the great problems confronting large scalable PSCs commercialization.

2. Perovskite solar cells historical progress

Historically, OMHP solar cells knew a progressive improvement at the scale of the perovskite absorber layer itself as well as the other layers constituting the solar cell system such as the hole, the electron transporting materials (HTM and ETM) and electrodes.

OMHP were initially appeared in dye sensitized solar cells and then as a p -type absorber [3] in April 2009, when Miyasaka from the University of Tokyo, was the first to

prove that $MAPbI_3$ and $MAPbBr_3$ could convert sunlight photons into electrical energy as light absorbing materials through dye-sensitized solar cell structures. Obtained PCE of 3.81% and 3.13 % for $MAPbI_3$ and $MAPbBr_3$ respectively in active area of 0.24 cm^2 opened up the first perovskite solar cell based on mesoporous TiO_2 photo anode [4,5].

In 2012, with SpiroMETAD on mesoporous TiO_2, on top of $MAPbI_3$ as light absorber, Michael Gratzel from the Swiss Federal Institute of Technology, Lausanne (EPFL) and Nam-Gyu Park in south Korea synthesised the solid state perovskite photovoltaic devices, the PCE was enhanced to the 9.7% [4,5]. Later, in the same year, the structure named meso-superstructured solar cell (MSSC) was invented by Snaith from the University of Oxford in England in collaboration with Miyasaka where the n-type mesoporous TiO_2 were replaced for the first time by an inert Al_2O_3 scaffold and the PCE increased to 10.9% [4,5].

In 2013, Liu and Snaith boosted more the efficiency to 15.4% via the vapour deposition heterojunction solar cell without electron conduction scaffold [4,5] and furthermore, they demonstrated that perovskite materials can themselves transport electron charges to the solar cell electrodes. Since that, a race to higher PCE has been launched over the perovskite community. The most reported PCE are 15.6%, 15.9%, 16.7%, 19.3%, 20.1% [5] and lastly, 25.2% [2].

3. Organomatallic halide perovskites (OMHP) structure

3.1. Crystal structure description

In this section, the description is focused on a main layer which is OMHP absorber. Known that the mineral $CaTiO_3$ was discovered by the geologist Gustav Rose in the Ural Mountains in 1839, and it was named perovskite to honor Count Lev Alexevich von Perovski, a russian mineralogist celebrity. After that, the description “perovskite” refers to any compound that has ABX_3 formula [6].

Generally, perovskite materials have the ABX_3 formula, in the ideal cubic system, for example, as shown in Figure.1, the A cation is located at the corner positions (0,0,0),

cation B is at the centre (1/2,1/2,1/2) and monovalent anion X is at the centre of the six planes (1/2,1/2,0), where an octahedron of X ions surrounded the B ion: A metal ion B^{2+} with six neighbouring halide anions X^- share $[BX_6]^{4-}$. Furthermore, each organic cation A^+ is coordinated by twelve X^- halide anions. (Figure.1) [7].

The perovskites can be grouped into two main classes: metallic and organometallic halide perovskites (OMHP) [5]. OMHP are the most widely used ones for photovoltaic applications. Organic cations at A sites are frequently amine derivatives like methylammonium (MA: $CH_3NH_3^+$), formamidinium (FA: $CH(NH_2)_2^+$), ethylammonium (EA: $C_2H_8N^+$) or other ionic organic compound. Wide range of metal cations like Pb^{2+} at B sites, and halide anions (Cl, Br, I) at X sites.

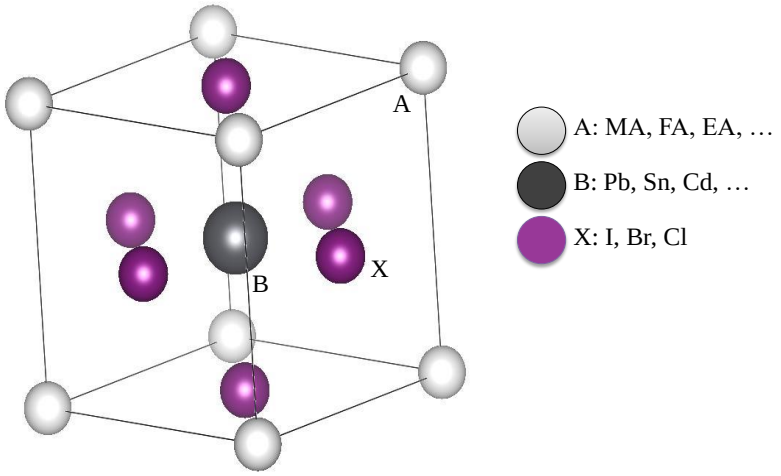

Figure.1. Cubic organo-metallic halide perovskite structure.

$MAPbI_3$ is the famous studied OMHP as absorbing material, but many other perovskites absorbers can be synthesized in order to investigate and discover their photovoltaic suitability, two substitution approaches are possible:

1. Homovalent substitution where the divalent cations of stable oxidation state +2 are suitable to replace Pb^{2+} in the perovskite structure. For instance, the elements (Ge^{2+},Sn^{2+}), alkaline earth metals (Be^{2+}, Mg^{2+}, Ca^{2+}, Sr^{2+}, Ba^{2+}), transition metals (V^{2+}, Mn^{2+}, Fe^{2}, Co^{2+}, Ni^{2+} ,Pd^{2+} ,Pt^{2+}, Cu^{2+}, Zn^{2+}, Cd^{2+}, Hg^{2+}), lanthanides (Eu^{2+},Tm^{2+},Yb^{2+}) and p-block elements (Ga^{2+}, In^{2+}) can be considered as an alternative lead free perovskites. However,

some of these candidates are not appropriate candidates for photovoltaic applications because of their large band gaps (Be, Ca, Sr, Ba), their toxicity, radioactivity (Cd, Hg), or their instability at the +2 oxidation state. Thus, the most promising candidates are Sn^{2+}, Ge^{2+}, Mg^{2+}, V^{2+}, Mn^{2+}, Ni^{2+}, Zn^{2+}, and Co^{2+} [8].

2. Heterovalent substitution is a second approach based on the replacement of the divalent lead cation with a cation in a different valence state such as a mono, tri or tetravalent cation Cu^{+}, Ag^{+}, Bi^{3+}, Sb^{3+}, and In^{3+}.... This substitution can be accompanied by a considerable structure change from ABX_3 type to $A_3B_2X_9$ type perovskites which is aimed at maintaining charge neutrality [9].

3.2.Formability

With various cations/anions in the perovskite structure, there are different lattice parameters. However, it is not always suitable to have random combinations of cation A, B, and anion X for photovoltaic perovskites. The crystallographic stability and probable structure can be governed by evaluating the Goldschmidt's tolerance factor *t* [10].

$$t= (r_A+r_X)/\sqrt{2}\ (r_B+r_X) \qquad (1)$$

Where r_A, r_B, and r_X are the effective ionic radii of the ions in the A, B, and X sites, respectively. The factor allows to estimate the degree of distortion of perovskite crystal structure compared to the ideal case where $t = 1$. As, it has been found that when $t = 0.75–1.00$ is not a sufficient condition for the prediction and formation of the perovskite structure [11], an additional indicator is required to examine the BX_6 octahedra in the perovskite structure and it is called the octahedral factor μ, defined as:

$$\mu = r_B/r_X \qquad (2)$$

The octahedral factor (μ) is an additional parameter for the perovskite formability. Thus t and μ parametes of stabilized perovskite range between $0.813 \leq t \leq 1.107$ and $0.442 \leq \mu \leq 0.895$ [7].

3.3. Phase transition

Most of perovskites structures are close to an ideal cubic structure, however, lower symmetry such as orthorhombic, tetragonal, rhombohedral, trigonal systems are present due to the frequent distortion, either by cation displacements, tilting of BX_6 octahedra such as Jahn-Teller (JT) effect [12] or distortion in the shape of the X group [13]. These lattice distortions as a result of temperature, pressure, chemical composition, and in some cases, electric field effects. Consequently, a phase transition offers a variety of interesting opto-electronic, electro-mechanical and conductive properties, which form the basis for many potential applications [14].

Table 1. Temperature dependent structural data of $MAPbX_3$ (X = CI, Br, I) [18].

Phase	Temperature (K)	Crystal system
$MAPbCl_3$		
α	178.8	Cubic
β	172.9-178.8	Tetragonal
γ	<172.9	Orthorhombic
$MAPbBr_3$		
α	236.9	Cubic
β	155.1-236.9	Tetragonal (I 4/mcm)
γ	149.5-155.1	Tetragonal (P 4/mmm)
δ	<149.5	
$MAPbI_3$		
α	327.4	Cubic
β	162.2-327.4	Tetragonal
γ	<162.2	Orthorhombic

To give insights into perovskites phase transitions, $MAPbI_3$, as an example, transits from α to β (tetragonal phase) to γ (orthorhombic phase) at 327 and 160 K respectively (Table.1) [15]. Although the temperature ranges vary from a perovskite to another, they show the similar structure phase transitions: from cubic to tetragonal to orthorhombic structure [16] which was confirmed by reported X-ray diffraction (XRD) data [17]. It has been noted that when rising temperature, the perovskites tend to undergo higher symmetry transformations [5].

In another way, doping the bromine (Br) or chlorine (Cl) into the $MAPbI_3$ lead effectively to phase transition from tetragonal to cubic structure because of the variation of the structural composition of $MAPbX_3$ (X = CI, Br) under temperature effect [19] as illustrated in Table.1.

4. Organomatallic halide perovskites properties

The photovoltaic properties of OMHP solar cells are strongly dependent on the crystal structure of the perovskite active layer, the fabrication process, the hole transporting layer, the electron transporting layer, the nanoporous layer and interfacial micro-structures [20]. The main concern in designing a photovoltaic solar cell is to increase its efficiency towards the electromagnetic energy reaching the absorber and to maintain it stable over the time against environmental conditions [5].

Recently OMHP based solar cells are promising photo-absorption materials, because they mainly combine the advantages at both synthesis and intrinsic levels; they are characterized by low cost processing, band gap tuning from the near-infrared to the visible spectra, efficient light emission and high carrier mobility [21-23], the continuous improvements in the control of synthesis techniques and in the understanding of the underlying physics boost up the efficiency to reach 25.2% in 2019. OMHP are also described by their important qualities such as high extinction coefficient, low exciton binding energies, long exciton diffusion lengths, high dielectric constants, and intrinsic ferroelectric polarization as well as improved carrier relaxation time [7,24].

4.1.Electronic properties

4.1.1. Band gap tuning

OMHPs represent a large class of semiconductors and display intriguing optical and electronic properties. The energy band-gap of these semiconductor perovskites can be easily tuned across a wide range of energy band-gap by modifying either the dimensionality (2D and 3D perovskites) or the organic-inorganic sites selective doping or the perovskite synthesis process [25].

Conventionally, structural dimensionality has been used as one of the criteria to account for photovoltaic properties and device performances of pervskite absorbers [26]. Until now, organic-inorganic 3D metal halide perovskite materials have become the appropriate candidates and are found to improve the solar cell efficiency [27].

In another side, lead free perovskites show continuous and monotonic variation of the energy levels in the case of tin (Sn); as the Sn concentration in the perovskite is increased [28]. In addition, the band-gap of such organic perovskite is affected by synthesis process, the size of organic cation, metallic ion and in halide ion. For instance, band-gap of $MAPbI_3$, $MAPbBr_3$, $MAPbCl_3$, $MAPbI_{3-x}Cl_x$ are 1.49–1.61 eV, 1.95 eV, 2.46 eV and 1.59 eV respectively [5]. So, broadening the range of solar irradiation absorption to the near-infrared spectrum could further enhance the performance of halide perovskite solar cells. Although, non-monotonic band-gap behavior in the perovskites is of great character and is of fundamental interest in the semiconductor field [29].

4.1.2. Density of states

Density of states (DOS) and partial charge density (PDOS) plots of OMHPs showed that almost Pb-p (metallic cation) and I-p (halide anion) states contribute to build the band-gap energy edges VBM and CBM respectively. In some perovskite materials, a coupling between Pb-s/p exists. Thus organic part/ion does not play a direct role to determine an effective electronic behavior, but effects the perovskite stability and changes its structure morphology, its size and its lattice constants [5].

4.2. Optical properties

It has been found that experiments on OMHP have shown that $MAPbI_3$, for example, exhibits ε' of about 6.5 at optical frequencies under the polarization of valence band electrons. The dielectric constants are important since ε', in particular, strongly influences the exciton binding energy (E_b) [3], a high exciton binding energy arises from a low permittivity. A comparable E_b of perovskite materials (29–50 meV for $MAPbI_3$, 35–98 meV for $MAPbCl_{3-x}I_x$) to thermal energy (~25 meV) at room temperature have been noted in many reports [7].

4.3.Partial and total doping

Doping of perovskite absorbent layer seems to be an efficient way to enhance both the stability and the performance of a perovskite solar cell. The doping can be performed on sites A, B and X or can be also into the electron transport layer or the other layers in order to obtain high a low cost OMHP solar cell [10].

4.3.1. Doping at site A

Site A is always occupied by MA, FA or EA.... or any long alkylammonium chains generally (Figure.1). The spherical shape, rapid rotation and hydrogen bonding to the halides X in the inorganic network B–X of the organic cations constitute a complex and distorted structural dynamics in OMHP [30]. Almost there is no overlap between the electron clouds of A and B–X due to the large unit cell, the electric neutrality due to Van-Der Waals force is maintained. However, the radius of ion A affects mandatory the symmetry of the perovskite structure which in turn affects the electron properties, thus the orientation of the A cation can influence the dielectric constant of OMHP materials [4]. In addition, improvements in the intrinsic stability of perovskites is enhanced [31].

In early work by Snaith in January 2014 [40], the FA is used to replace MA and formed $FAPbI_3$, it helped to decrease the absorption band-gap at about 1.48 eV and the PCE of $FAPbI_3$ based solar cell reached 14.2%. In the same year, Park fabricated $FAPbI_3$ on the substrate of mesoporous TiO_2/FTO and obtained device PCE of up to 16% [4].

Lastly, much more effective photon absorption has been obtained through mixed organic cations $(MA)_x$ $(FA)_{1-x}PbI_3$, a PCE has reached up to 14.9% due to the changing band gap. However, when doping the mixed organic cations with small amount of Cs, For example, $Cs_{0.2}FA_{0.8}PbI_{2.84}Br_{0.16}$ hybrid device PCE over 17% was reported as well as an excellent stability in ambient air compared to $FAPbI_3$ [4].

4.3.2. Doping at site B

Over the perovskite community researches, the ideal element which suits the organic-inorganic perovskite absorbers at site B is Pb (Figure.1), but many other atoms in the same group elements can be easily referred to. For example,

doping/replacing/substituting Pb^{2+} with Sn^{2+}, Ge^{2+}, Sr^{2+}, Cd^{2+}, and Ca^{2+} ... has detected hidden properties in OMHP crystalline phase, band structure, absorption and optical characteristics, hence it allows to develop many possible applications.

The importance of doping at site B appears when further improvements in photovoltaic performance can be achieved by the enlargement of light absorption. Since $MAPbI_3$ only absorbs light at wavelengths below 800 nm. So, substituting totally or partially Pb within OMHP has been found to increase light harvesting in the NIR region up to 1000 nm and, at the same time, reduce the toxicity issue related to Pb [32].

4.3.3. Doping at site X

From the perspective of OMHP materials design, the site X is occupied by halogen atoms (Figure.1), most famously the iodine at the beginning and can be replaced by Br or Cl effectively to tune the band gap of perovskite structures. Then, the absorption band gaps of $MAPbI_3$, $MAPbBr_3$ and $MAPbCl_3$ increase with the decrease of halogens atomic number; the greater the absorption band-gap, the lower the amount of sunlight that can be absorbed. Therefore, OMHP can be tailored to achieve many interesting applications [4].

With mixed halogens doping, many researchers have reported that doped $MAPbI_{3-x}Cl_x$ at the tetragonal phase and $MAPbI_{3-x}Br_x$ were attempted to improve both their diffusion length and carrier lifetime as well as their stability [4].

5. The perovskite solar cell (PSC) architectures

Organo-metallic halide perovskite based photovoltaics can be grouped into three structures: the mesoporous PSCs, regular type planar PSCs and inverted type planar PSCs, as shown in Figure.2.

The mesoporous PSCs have started from a typical dye-sensitized solar cell using the liquid electrolyte which was invented by the Miyasaka group in the first time [33]. After that, the solid state sensitized solar cell is synthesized by replacing the dye molecules with lead halide perovskite.

Currently, the use of a mesoporous metal-oxide layer (like TiO_2 and Al_2O_3) as the scaffold for depositing perovskites in this configuration, as illustrated in Figure.2.(a) [3]. For instance, a mesoporous solar cell structure with PCE of 20.2% [4], based on fabrication order includes: FTO: Fluorine Tin Oxide as (conductive glass substrate) / TiO_2 compact layer / mesoporous TiO_2 as (electron transporting material) / $MAPbI_3$ as (perovskite absorber) / PTAA: Poly[bis(4-phenyl)(2,4,6-trimethylphenyl) amine as (hole transporting material) / Au as electrode

The main disadvantage of the mesoporous configuration for photovoltaic solar cells is the negligible light absorbance at Near-Infrared wavelengths. Moreover, required high temperature annealing of the mesoporous layer deposition is an inconvenient for fabricating large area devices on large sized FTO substrates [33].

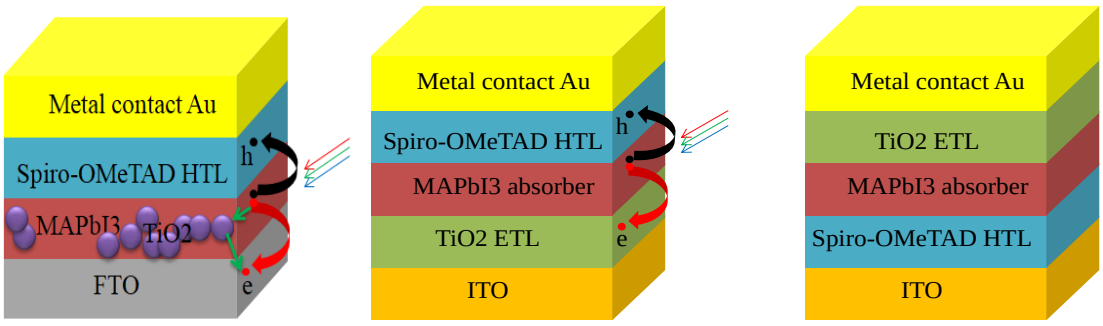

(a) (b) (c)

Figure.2. Illustration of $MAPbI_3$ PSCs structures (a) mesoporous (b) regular (conventional) planar type (c) inverted planar type.

Other emerging configurations that offered high efficiencies, such as the planar PSCs structures, have attracted more attention. Shortly after the widespread of mesoporous PSCs, the planar structure and the metal oxide free solid state interlayers processing dominate the OMHP studies [3].

A planar perovskite based solar cell is constituted of three main functional layers sandwiched between two conducting electrodes. The fundamental scheme for a planar heterojunction perovskite based solar cell is: back electrode / hole transporting material (HTM) / Perovskite absorber / electron transporting material (ETM)/ transparent

electrode. The concept of planar PSCs is derived from an experimental study in which the Al_2O_3 based mesoporous PSC is synthesized. It has been concluded from that study the perovskite absorber itself can be a by trap of electrons, hence the mesoporous TiO_2 electron conducting is not necessary suggested for PSC high performances, which makes the metal oxide free PSCs convenient for low temperature fabrication [5].

The common planar PSC configurations are either the p-i-n (inverted) or n-i-p (regular) hetero-junction PSCs types, both types are inserted between two conductive electrodes. The process sequence of a regular type organic photovoltaic structure is: ITO or FTO, ... conductive glass / PEDOT:PSS, Spiro-OMeTAD,...(HTM) / $MAPbI_3$ perovskite (absorber) / PCBM, TiO_2 ... (ETM) / Au, Al, ...(electrode) which exhibited more than 17% efficiency. In another side, as inverted type example of process order: ITO conductive glass / TiO_2 / $MAPbI_{3-x}Cl_x$ perovskite absorber / Spiro-OMeTAD /Au has exhibited a PCE of 19.3% [4].

Generally, planar PSCs are characterized by easy fabrication process for the regular type, thin perovskite layer less than 400 nm thick due their extremely high absorption coefficient and elevated PCE, although the planar PSCs are described with much worse J–V hysteresis compared to the mesoporous ones [4].

In addition to the absorber layer, to obtain optimal PSC performance; electron and hole transporting materials are necessary materials to investigate in most PSC configurations not only to achieve high efficiency PSCs, but also to provide better stability for them. Basically, the first property should ETM and HTM own is a long carrier diffusion length. The detailed literature concerning the frequently used ETM and HTM in PSCs as well as their alternatives to enhance their performances and stability are presented in this chapter.

6. Functioning principles of perovskite solar cells (PSCs)

In such PSC, the perovskites are considered as absorbers. Under light stimulation, perovskites are excited which create an electron-hole pair. The process is effectively a p-n junction behavior that leads to a built-in electric field that allow the charges

separation where the photo-generated electrons diffuse through the perovskite absorber to the continuous electron transport material (ETM), or do so via the mesoporous scaffold if present and made out of suitable ETM like the widespread ETM (TiO_2), subsequently, the electrons are collected at the electrode and the photo-generated holes diffuse also through the perovskite absorber to reach the hole transporting material (HTM), from where they being collected at the metal electrode (Figure.3).

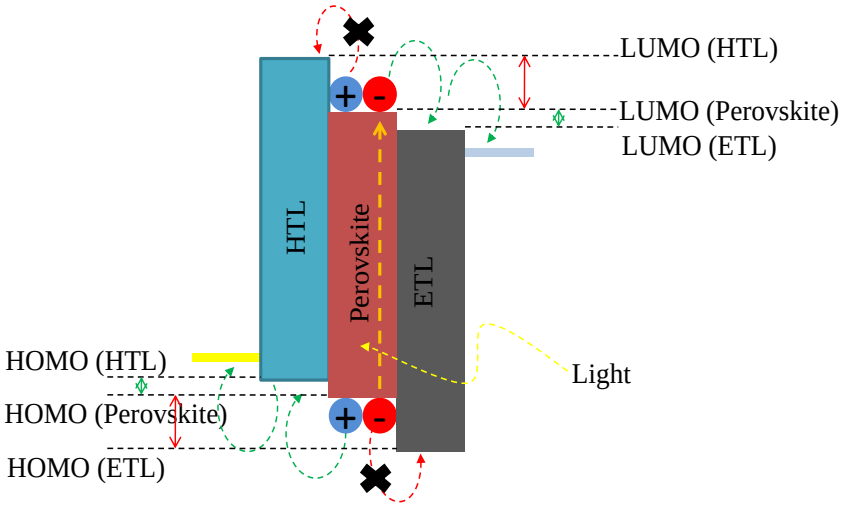

Figure.3. Functioning principles and schematic energy levels of PSC.

Electron and hole transporting materials are charge selective layers, they are important parts of PSCs as they prohibit or permit charges to reach the electrodes. This role is determined by the right selection of the energy levels of ETM and HTM with respect to those of the perovskite absorber [41]. The HTM material should have its lowest unoccupied molecular orbital (LUMO) for above that of perovskite. At the same time, its highest occupied molecular orbital (HOMO) should be just slightly above perovskite valence band. The opposite conditions are required for ETM material (Figure.3).

During the extraction of photo-generated charges, unwanted reactions can be appeared such as exciton annihilation by photoluminescence; non-radiative recombination (heat loss) and charge recombination that occur at defects in the perovskite, or at interfaces, grain boundaries or in impurities of the perovskite [42].

7. Perovskite absorber layer synthesis methods

Almost all the OMHPs experimental studies emphasise the important role of processing techniques in enhancing the PCE of perovskites by changing the fabrication process, solvent engineering, or precursor solution. Different structure and morphology of perovskites result from different synthesis approaches which affect greatly the perovskite absorbing layer and the stability of the PSCs.

Despite the fact that of OMHPs are described by their low formation energy, low Young's modulus and high thermal expansion coefficients, this soft nature does not only enable perovskite thin films to be fabricated via low temperature deposition methods but also presents rich opportunities to design high quality thin films to obtain the specific needs of a such PSC device type and architecture [34] by tailoring the desired electronic band-gap, optical constant and absorption spectrum [35].

Various methods have already been subject to intense investigation and have been suggested for the fabrication of high quality perovskite layers for PSCs. This part of this chapter takes a glance on the most existing fabrication methods of perovskite films for PSCs applications.

The synthesis and fabrication of OMHP films are broadly classified into two types such as; solution processing techniques and vapour processing techniques.

7.1. Solution processing techniques

Solution processing techniques include the one step deposition (OSD) method where all the precursors constituting the perovskite layer are deposited simultaneously onto the substrate and the sequential deposition method (SDM) where each precursor is deposited sequentially or separately onto the substrate. Solution processing of perovskite films is low cost and easy process to produce high quality perovskite thin films [35]. There are many solution processing techniques such as spin coating, screen printing and dip coating [36]. In this thesis, more analyses are devoted to the basic spin coating deposition technique because it is easy, more reliable and reproducible for high efficiency PSCs.

7.1.1. One step spin coating deposition (OSD) method

One step spin coating is considered the easiest method for preparing perovskite films since Kojima successfully in 2009 arrived at the fabrication of the first methylammonium lead iodide ($CH_3NH_3PbX_3$) based PSC and the investigation of its optical properties [34].

In the one step method, the synthesis of the perovskite films principally is the direct intercalation of the organic halide into the metallic halide [33]. For instance, the precursors (sources) CH_3NH_3X and (PbX_2) (MAI and PbI_2 or FAI and SnI_2...) are mixed together in a solution and simultaneously dissolved in a polar solvent such as dimethylformamide (DMF), dimethylsulfoxide (DMSO), γ-butyrolactone (GBL) inside a nitrogen glove box [34], following the reaction.

$$CH_3NH_3X + PbX_2 \longrightarrow CH_3NH_3PbX_3$$

An illustration of the OSD technique for the perovskite absorber layer is shown in Figure.4, where a $CH_3NH_3PbX_3$ film is deposited by spin coating of the $CH_3NH_3PbX_3$ precursor. Firstly, the precursor solution is dropped onto a spinning TiO_2 layer. Then, a dense layer of $CH_3NH_3PbX_3$ is shaped by increasing gradually the spinning rate coating which helps to remove the excess solution from the substrate through centrifugal force [34]. In last, as a post processing, the perovskite films is annealed until the evaporation of the remaining solvent [35].

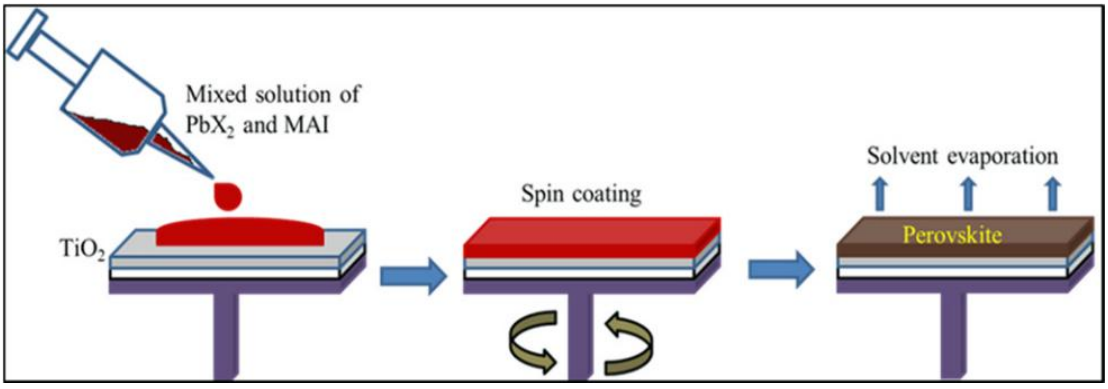

Figure.4. One step spin coating deposition method steps [35].

Depending on the perovskite crystallization mechanism, many focused literatures cited two strategies to deposit high quality perovskite films: the first one consists in retarded

crystallization, when the formed precursor film is followed by a slow perovskites crystallization and the second one consists in rapid crystallization, when the nucleation/crystallization of perovskite film is processed before the solvent evaporation is finished [33].

The thickness and morphology of resulting film are controlled by different parameters, such as the solution viscosity, temperature and spinning velocity [36]. Also, the presence of high density defects such as pinholes of the developed perovskite films has been noted in many studies which prevent PSCs enhancement and would be another challenge for the OSD method. These defects have been basically referred to the film shrinkage during the perovskite crystallization process at the removal of solvent [33].

Arguably, in one hand, the OSD spin coating method is low cost, fast processing and allows the possibility of multilayer depositing and small quantities of solution needed for covering large substrate area. On the other hand, their drawbacks rise in the incompatibility with roll to roll processing [36]. In addition, the poor coating of the film leads to the short circuits due to the contact between the upper and lower electrodes [4].

In order to control the kinetics of crystal growth and film quality, the anti-solvent dripping (ASD) method is considered an advanced OSD and has been proposed as an attempt to push the advantages of OSD through the above mentioned issues [35]. A schematic illustration of anti-solvent processing for OSD technique is represented in Figure.5. In the ASD method, shortly after forming the perovskite on the substrate by spin coating, the anti-solvent (toluene...) is dripped during spin coating and the substrate is annealed at high temperature as shown in Figure.5 [35].

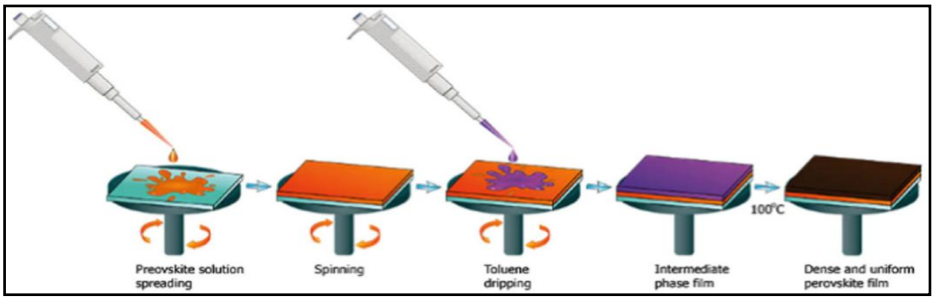

Figure.5. Aniti-solvent one step spin coating method steps [35].

Figure.6 shows a comparison of the surface morphology of the $CH_3NH_3PbI_3$ absorber on the top surface of the TiO_2 layer obtained by OSD and ASD. In Figure.6(a), the non uniformity of the planar $CH_3NH_3PbI_3$ has been observed. In contrast, a dense and smooth layer has been upon the ASD treatment, as shown in Figure.6(b). In 2017, an increase of PCE to 22.1% has been achieved by Yang due to the enhancement of surface morphology of perovskite film given by ASD treatment [35].

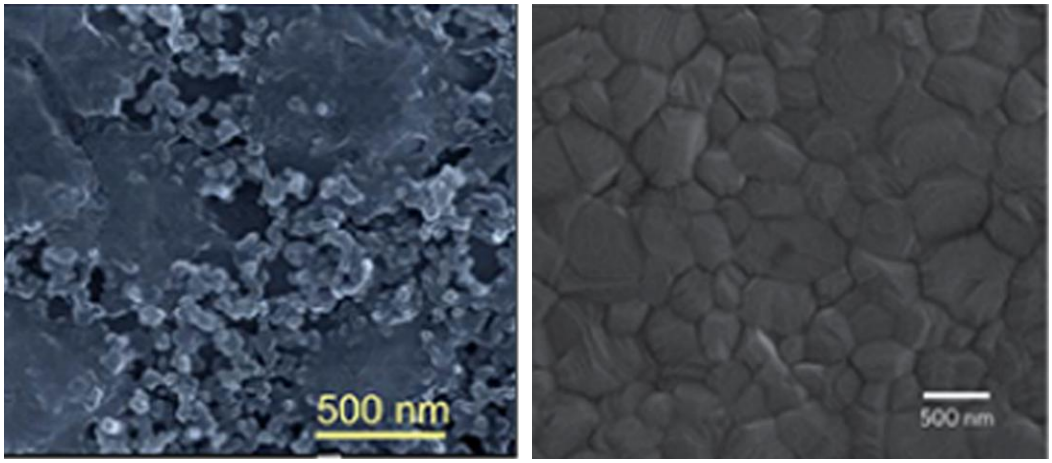

(a) (b)

Figure.6. Comparison of $MAPbI_3$ surface morphology between one step and anti-solvent one step spin coating deposition methods [35].

7.1.2. Two-step spin coating deposition method

The main inconvenient in the one step deposition methods is that the naturally crystallized perovskite films mostly posses a poor film uniformity and low perovskite crystallinity [33], whereas the grain size of perovskite crystallization can be directly regulated using two step deposition methods.

The two step deposition (sequential deposition method (SDM) method) of perovskite film is firstly reported by Mitzi [35], in which the MAI intercalates into the PbI_2 precursor film to form $MAPbI_3$ perovskite by dipping PbI_2 film in MAI solution. Then, Gratzel was the first to arrive at fabricating a mesoporous PSC with two steps deposition [33]. In a typical two step method, for example the formation of $MAPbI_3$ perovskite is the intercalation of MAI into the PbI_2 layer. The method benefits greatly from the uniform and compact PbI_2 layer obtained by solution or vapor deposition of PbI_2 precursor which

allows easy intercalation of ammonium. The intercalation process is characterized by the MAI diffusion rate on top of PbI_2; in the mesoporous structure, it takes only a few seconds for the complete conversion of PbI_2 into perovskite using TiO_2 mesoporous films in. In contrast, for preparing planar perovskite configuration, it takes many hours for the complete conversion of compact PbI_2 into perovskite on planar substrates [33,34].

So, in the two steps deposition, the morphology of the obtained perovskite film is intensely depended on the PbI_2 layer and the complete conversion rate is via the diffusion of MAI into the PbI_2 layer. These features describe two challenging problems in this method which are $MAPbI_3$ volume expansion and MAI diffusion into the PbI_2 layer [33].

Many approaches have been suggested to untangle the problem of intercalating MAI into the PbI_2 layer. Firstly, Gratzel has developed the pre-wetting technique to fabricate a PSC of 14% PCE [33]. It consists of pre-wetteing the PbI_2/TiO_2 coating layer in isopropanol (IPA) before dipping in the MAI solution step as shown in Figure.7 [33].

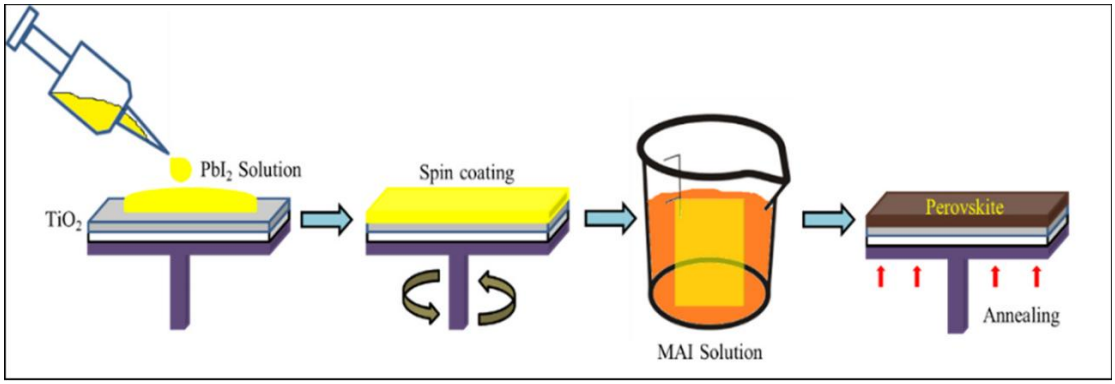

Figure.7. Sequential (two step) deposition method using pre-wetting technique [35].

Another presented technique is the tow-step spin coating method which was mostly proposed by Huang [35] and Park [33] as a modified sequential deposition method (SDM) method, to resolve the issue caused by the dipping method; in the tow-step spin coating method, the size of $MAPbI_3$ is well controlled by varying the MAI concentration during the 2^{nd} step of spin coating as shown in Figure.7 [35].

Figure.8 illustrates the two-step spin coating deposition technique for fabricating $CH_3NH_3PbI_3$ perovskite. In the first step, the PbI_2 layer is spin coated over the top of the

TiO_2 substrate and then dried. After cooling at room temperature, the CH_3NH_3I solution in (IPA) is loaded again on top of the PbI_2/TiO_2 coated layer, spin coated and then dried again to finally obtain the perovskite film [35].

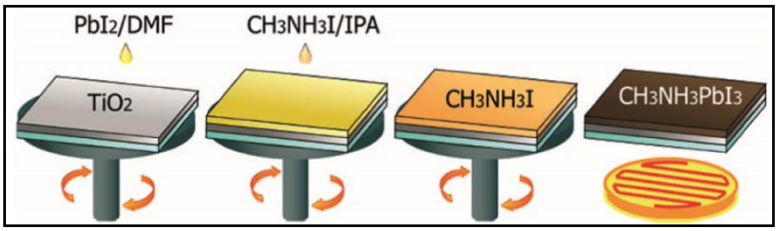

Figure.8. Two-step spin coating method [35].

It has been found that the $MAPbI_3$ crystal growth is also affected by the MAI concentration, such as low MAI concentrations produce large cuboid crystals, which have gaps between themselves and show enhanced PCE because of enhanced internal light scattering [35].

Recently, one other technique, the intra-molecular exchange method has been reported by Seok to deal with the volume expansion issues, in which negligible volume expansion with large crystal grains has been observed, resulting in pinhole free perovskite films. The PSC using this method has achieved a PCE of 20.1% [33].

7.2. Vapor assisted processing (thermal evapration)

Vapor processing techniques are divided into vapor assisted solution process (VASP), thermal vapor deposition (TVD) method, chemical vapor deposition (CVD) and microwave irradiation process (MIP) [35,36].

7.2.1. Vapor assisted solution process (VASP)

Vapor assisted solution process (VASP) is a two step heterogenous solid/vapor deposition approach (also known as two step hybrid deposition) and it is first adopted by Yang [33] and Snaith [34] as a modification of the SDM to fabricate high quality, pinhole free planar $MAPbI_3$ films. This method has been used to avoid incomplete dissolution associated with the solid/liquid interface and as an alternative to replace either the regular MAI solution soaking or dipping steps (second step of two-step deposition method).

The VASP method steps are depicted in Figure.9, in which the PbI_2 films is deposited firstly by spin coating over the top of the TiO_2 substrate from solution precursor and then, the PbI_2 layer is subjected to MAI vapor by spraying MAI over the layer area and heating the container at high temperature [34]. Consequently, the morphology and uniformity can be more controlled by this method via solid/vapor crystallization [35].

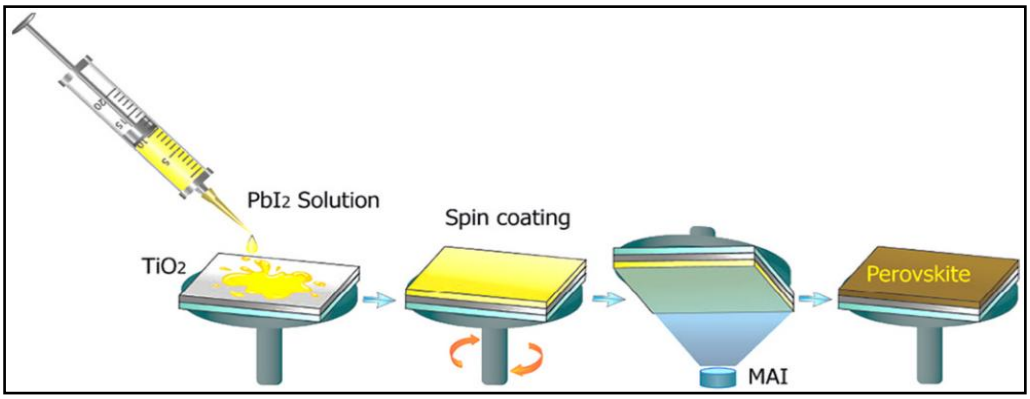

Figure.9. Vapor assisted solution processing steps [35].

The VASP shows many properties dedicated to PV applications [35] but it has been considered a slow technique when much time is required for a complete reaction between the PbI_2 underlayer and MAI [34]. One of the highest achieved PCE via the VASP method in last year's was 12.1% [34,35].

7.2.2. Thermal vapor deposition (TVD)

In this method, MAI and PbI_2 are simultaneously deposited by thermal evaporation from two different and separate sources at definite molar ratios under high vacuum as shown in Figure.10. Finally the perovskite film is obtained after annealing process [35].

Although the uniform thickness and surface morphology of perovskite films gained by single and dual source co-evaporation in TVD method, simultaneous evaporation has been faced the deposition rate control challenge. For that reason, the sequential thermal evaporation (sequential vapor deposition) has been suggested, in which a brute force evaporation of the MAI onto heated PbI_2 substrate is used [34]. This method used to produce a planar $MAPbI_{3-x}Cl_x$ PSC with a PCE of 15.4% [35].

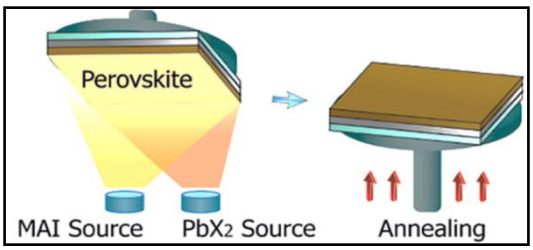

Figure.10. Thermal vapor deposition steps [35].

7.2.3. Chemical vapor deposition (CVD)

The CVD method has mainly headed towards the industrial technology for the production of perovskite films. There are wide variations of CVD method including tubular CVD, metal-organic CVD, plasma-enhanced CVD and photo-initiated CVD. In addition, hybrid CVD (HCVD) and low pressure CVD (LPCVD) are widely used CVD methods for perovskite deposition. However, some of the CVD methods such as, in situ tubular chemical vapor deposition (ITCVD) and aerosol-assisted chemical vapor deposition (AACVD) need complex equipment and are not very accessible [35].

7.2.4. Microwave irradiation process (MIP)

This method has been firstly experimented by Ahn. As illustrated in Figure.11. PbI_2, MAI, and DMSO are mixed in dry DMF solution to obtain the $MAPbI_3$ precursor which is followed by a spin coating on the TiO_2 substrate, in the same time the diethyl ether $(C_2H_5)_2O$ is dropped on the spinning substrate, which is then undergone microwave annealing [35]. The MIP is a rapid and simple method with controllable crystallization.

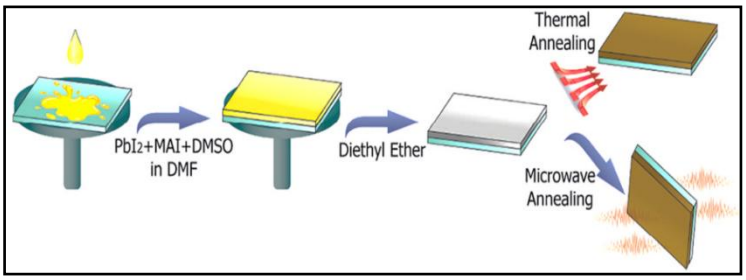

Figure.11. Microwave irradiation processing steps [35].

7.3.Solid state reaction

In this technique, the planar $MAPbI_3$ perovskite result from two thin layers: MAI and PbI_2 solid precursors, which are brought into contact with each other via thermally accelerated diffusion, as presented in Figure.12. The perovskite films obtained by solid state reaction fabricated showed soft surface coverage and great optical absorption [33].

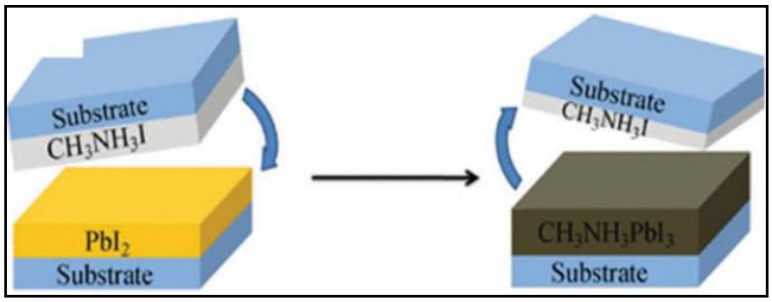

Figure.12. Solid state deposition steps [33].

8. Large area PSCs processing towards marketing

Most of the previous cited techniques aimed at enhancing the PSCs efficiency and have been developed to target the highest setting for small area PSCs [34]. In recent attempt, a planar hybrid PSC fabricated via spin coating method has achieved 12% over 100 cm^2 area. The solar cell consists of an inverted configuration of ITO/PEDOT:PSS/$MAPbI_3$/PCBM/Au, but, unfortunately, it cannot be applied for extra large surfaces because an interesting amount of the precursor solution is wasted during the spinning [33]. Therefore, they are generally unsuitable for large scale processing [34].

The high remarkable improved PCE of 3rd PSCs generation and their simple fabrication methods make the transfer from the laboratory PSCs toward scaling-up PSC designs and hence to marketed products to be a requirement. Several upsizing techniques have been suggested for large scale fabrication, two basic methods such as doctor-blading and spray coating (also their variations: slot die coating; also called slot casting or split casting, roll-to roll method, meniscus-assisted solution printing, soft-cover coating) and (inkjet printing) respectively [34] are outlined in the thesis.

8.1. Doctor-blading.

Doctor-blading or blade-coating is a solution chemistry deposition common to spin coating technique in which a moving blade removes the excess solution over the substrate, as shown in Figure.12. The doctor-blading is a rapid process and avoids lead contamination. With the use of this technique, Deng and Huang have fabricated small-area (7.5 mm^2) PSCs with PCE over 20% and large-area modules (33, 57.6 cm^2) with 15% PCE [33,34].

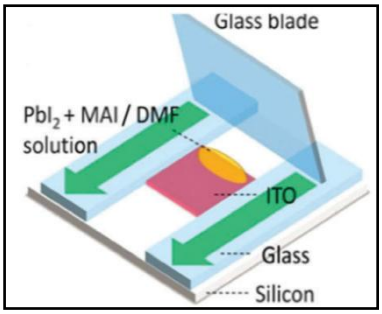

Figure.13. Illustration of conventional doctor-balding technique [33].

8.2. Slot-die coating

Slot-die coating (slot-casting/slit-casting) differs from doctor-blading when the precursor solution is spread onto the substrate by a die that serves as a print head. Low PCE has been obtained by Schmidt (4.9%) and Cotella (9%) in a very small area using this process [34].

8.3. Roll-to-roll method

This method is considered as sequential slot-die coating and has been demonstrated to produce efficient PSCs. In this method, after the slot-die coating, a gas-quenching process is used to evaporate the precursor solution of PbI_2 substrate [33].

8.4. Meniscus-assisted solution printing

This technique is a mixture of blade-coating and slot-die coating methods. A $FA_{0.85}MA_{0.15}PbI_{2.55}Br_{0.45}$ based PSC reaches a PCE of about 20%, which is cited among the highest efficiencies in scalable processing methods [34].

8.5. Soft-cover coating

This technique is quite comparable to MASP, it refers to soft-cover deposition in which the precursor solution is dropped onto a heated substrate. Then, it is covered by a flexible sheet (such as polyimide) to distribute the solution upon the substrate. Large-area PSCs of 1 cm^2 have been produced via this technique that has attained a PCE of >17%, not as high as MASP, but it is faster than it [34].

8.6. Spray-coating

Spray-coating has the advantage of coating large-area substrates without losing material precursors; furthermore patterned substrate is allowed [33]. In this technique, a perovskite ink or precursor solution is ejected through a nozzle, as shown in Figure.13. The PSCs using this method have attained 18% PCE [33,34].

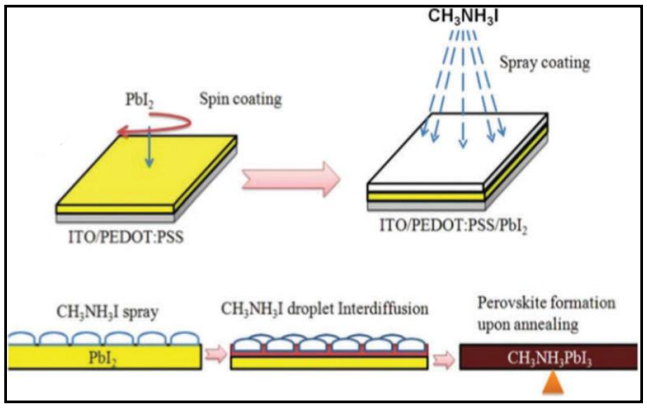

Figure.14. Spray coating method steps [33].

8.7. Inkjet printing

In inkjet printing technique, the resulting jet is steered drop by drop in order to achieve perfect patterns. This approach has led to a PCE of 17% [34].

At the scale-up level, companies like Oxford Photovoltaics Ltd, Saule Technologies, Greatcell Solar, and Panasonic [1] are developing conventional and flexible perovskite modules for manufacturing and commercializing perovskite solar technologies.

9. Other OMHPs applications

Organometal metal halide perovskites are additionally promising candidates for other applications, as they also exhibit intense photoluminescence, they find uses in light emitting devices (LEDs), laser, field effect transistor (FET), as well as high performance photo-detectors (visible/infrared, X-ray and gamma-ray), nonlinear optics and spintronics [7,15,22,33,34,37].

10. Issues and challenges

So far many challenges related to OMH-PSCs need to be investigated, although the fast development at the research scales over the last years towards high PCEs. In fact, these obstacles prohibit this emerging photovoltaic technology to compete with the existing solar cell markets in power grid applications [35], these include device long-term stability of OMH-PSCs against high temperature [38] and moisture sensitivity (relative humidity) [39] which are considered the main factors facing their actual widespread application and have to be fully examined especially for $MAPbI_3$ perovskite. In addition, the environmental concerns with the inclusion of Pb and Sn when upscaling to large-area modules [26].

Until now, organometallic lead halides (OMH) based perovskite solar cells (PSCs) have shown limited operating life times due to degradation not only of the perovskite materials, but of all the layers of PSC devices such as electron transport material (ETM), hole transport material (HTM) and electrodes.

$CH_3NH_3PbI_3$ ($MAPbI_3$) is fluently considered as an ideal candidate absorber and preserve the excellent absorption and charge transport properties, while it should be thermodynamically stable and environment friendly. The inherent instability of $MAPbI_3$ (degradation when exposed to water, oxygen, UV-light, high temperature) and its toxicity (presence of lead) hinder further development of perovskite-based solar cells on the long term but opens up the possibility towards the improvement of the PSC perfection in term of high efficiency of one side and long term stability in another side.

In this chapter, the state of the art of PSCs stability is presented. The function and the principle of a perovskite as a p-i-n junction are explained. Then, the most factors intrinsic or extrinsic effects influencing the stability and the efficiency of PSC in which the degradation of different layers mechanisms are described and the latest stability enhancement strategies are reported.

11. Degradation mechanisms of the perovskite solar cells (PSCs)

Improvements toward stable PSCs require understanding the device as a whole and interference layered compound, not concerning only the stability of the individual layers independently. Basically, the issues related to the stability of PSCs can be divided into intrinsic stability factors such as the atomic composition and the structure of the perovskite absorber itself and many other factors considered as extrinsic effects on the stability of PSCs such as relative humidity (RH) (also referred to moisture), temperature (T), oxygen (O_2), UV light, fabrication and deposition methods of PSCs [42]. Additionally, the impact of the layers constituting the PSC like ETM, HTM and electrodes influences also the stability of PSCs. In this work, the factors that cause the degradation of the PSCs are detailed as well as the recent approaches to improve their stability are cited.

11.1. Effect of atomic composition and structure of the perovskite absorber

$MAPbI_3$ perovskite based PSCs are attractive due their high PCEs. But, compared to silicon (Si) which is reported to have a mean degradation of 0.8% per year, it has been studied that all perovskites need long term stability. So, considerable efforts were made toward stability in PSC devices.

The Goldschmidt's tolerance factor t defined as $t = \frac{(R_A + R_X)}{\sqrt{2}(R_B + R_X)}$ [43] is one of the aspects that expresses the formability of such ABX_3 perovskite structure. Thus, partial or total substitutions of the chemical composition of perovskites adjust t and significantly affect their intrinsic stability.

In fact, the tolerance factor t, fails to explain the relative stabilities of the distorted phases for the same ABX_3 perovskite. Hence, further stability descriptor for cubic

perovskites is identified, it is expressed as: $(t + \mu)^{\eta}$, where t, μ and η are the tolerance factor, the octahedral factor (defined as the ratio of the radii of B site cation and the X site anion) and the atomic packing fraction (AFP) respectively.

It has been found, by investigating the stability of titled halide perovskites ABX_3 (A = Cs, Rb and K; B = Pb and Sn; and X = I, Br, and Cl), that the stabilization energies which is the energy differences between cubic and the most stable tilted phases of different perovskites are linearly correlated with the stability descriptor $(t + \mu)^{\eta}$ [44] . So, the atomic packing fraction is crucial factor to understand the stability of perovskites in their ideal and tilted phases.

The atomic composition importance raises in the atomic substitution of any compound constitutes the ABX_3 perovskite. Despite the attractive absorption of $MAPbI_3$, its degradation process is strongly faster under higher light intensity and temperature. It was found that $MAPbI_3$ film degraded after exposure to 100 suns for 60 min under temperature of 45-55℃. However, the reported lower efficiencies with devices with $MAPbBr_3$ and $MAPbI_2Br$ based PSCs as light absorbing material, they showed better stability compared to $MAPbI_3$. This improvement is attributed to the bonds strength and their crystalline structure of $MAPbI_2Br$ and $MAPbBr_3$ [45].

It was observed that $CsPbBr_{1.5}I_{1.5}$ could be an alternative solution for stable perovskite quantum dots (QDs). The photovoltaic devices made from $CsPbBr_{1.5}I_{1.5}$ showed power long term stability. This PCE is also the highest among other PV results for QDs with $CsPbBr_{1.5}I_{1.5}$ composition [46].

A study cited that FAI perovskite films were stable when exposed to temperatures up to 150℃ in air; this is unlike $MAPbI_3$, which was shown to undergo a structural phase change at 55℃. To overcome this stability problem, 10% of Cs is substituted into the A cation position, forming a new absorber: $FA_{0.9}Cs_{0.1}PbI_3$. An increase in PCE, from 14.9% to 16.5% is reported. This was attributed to a reduction in recombination due to a reduced trap state density. Under ambient conditions (RH < 40%), the $FA_{0.9}Cs_{0.1}PbI_3$ devices degraded at a slower rate than $FAPbI_3$, due to better intrinsic thermal and moisture stability of the absorber. Although the stability is improved, both devices degraded to less than 20% of their initial PCE within an hour [47].

Using triple (or multiple) perovskites with mixed cations and halides has recently attracted attention. For example, $(Cs_{0.05}(MA_{0.17}FA_{0.83})_{0.95}Pb(I_{0.83}Br_{0.17})_3$ perovskite solar cells (referred to CsMAFA), with PCE of 22.85%, exhibited a stabilized efficiencies to more under operational conditions (maximum power point tracking under full illumination held at room temperature). Tuning the Cs^+ content also helps preventing halide segregation. The triple cation perovskite films are thermally more stable and less affected by external surrounding factors such as temperature, solvent vapours or heating protocol [48-50].

An astonishing stability resulted by four cations (Rb/Cs/MA/FA) perovskite device with 21.6% PCE, that maintained 95% of initial PCE after 500 h at 85℃ under full solar illumination and maximum power point (MPP); poly (triarylamine) (PTAA) was used as HTM. Very recently, some of the highest efficiency for non-MA compositions, stabilized $RbCsFAPbI_3$ and CsFA, were reported 20.35% and 21.1% of efficiency respectively [51][51]. Moreover, stability was found to improve when part of the I is partially substituted by thiocyanate (SCN) [52].

Using two dimensional (2D) hybrid perovskite absorbers can also enhance the stability of PSCs. It has been cited that the solar cells containing $(PEA)_2(MA)_2(Pb_3I_{10})$, where $(PEA = C_6H_5(CH_2)_2NH_3^+)$, as an absorber did not suffer any decomposition even after 46 days when it is exposed to 52% of relative humidity indicating greater moisture resistance compared to the cells based on $MAPbI_3$ that degraded after 4-5 days under the same condition [45].

In order to avoid the harmful toxicological issues of lead, the most appropriate element to replace Pb is tin (Sn) [53]. $MASn(IBr_2)$ absorber encapsulated with Surlyn films in a nitrogen filled glove box was investigated, the device efficiency dropped to 36% of its initial (almost PCE: 6%) value after 24 h. This decay was affected by Sn^{2+} ions oxidation [47].

11.2.Effect of relative humidity (RH) (moisture)

The effect of water molecule on the chemical stability of $MAPbI_3$ material is represented by a series of chemical reactions under different conditions. Reactions for the moisture catalyzed decomposition of the perovskite layer are written below as [45]:

$CH_3NH_3PbI_3$ (s) ⟶ PbI_2 (s) + CH_3NH_3I (aq) (1)

CH_3NH_3I (aq) ⟶ CH_3NH_2 (aq) + HI (aq) (2)

4HI (aq) + O_2 (g) ⟶ $2I_2$ (s)+ $2H_2O$ (l) (presence of oxygen) (3)

2HI (aq) ⟶ H_2 (g)+ I_2 (s) (under UV light) (4)

The water molecules hydrolyze the perovskite $CH_3NH_3PbI_3$, this reaction leads to bonds rupture rendering back the two precursors (Reac (1)). Then, the CH_3NH_3I decomposes to produce HI (Reac (2)), which afterwards degrades in the presence of oxygen (Reac (3)), or after the exposition to UV light (Reac (4)). Due to this fact, the fabrication of PSC should be assisted inside a glove box filled with an inert gas (normally N_2) to avoid the perovskite to hydrolyze and in order to achieve high performance [41].

The irreversible degradation of the perovskite layer is a problem for the life time performance of the photovoltaic cell besides the solubility of PbI_2, in water which could cause significant eco-toxicological problems in the field. Based on experimented results, exposition to higher RH values (98%) in only 4 h extremely dropped the $MAPbI_3$ film absorption to half of its original value [47]. Another side, for 20% RH, the perovskite was stable for 10,000 h. The experiment was carried out using different carrier gases, like N_2 and air, it has been concluded that the moisture is the fundamental factor of PSC film degradation at normal atmosphere [54].

In another experiment, it has been observed that when $MAPbI_3$ is exposed to RH (70%) at room temperature for 60 h, its band gap increases until 3.1 eV by forming $MAPbI_3 \cdot H_2O$ that could return to the original structure after being exposed to a dry atmosphere. In addition, the photovoltaic performance of solar cell stored in 90% of humidity revealed a fast performance decrease from 12% to less than 0.7% in three days. The cells stored at 50% and 0% humidity showed higher stability with the total loss of less than 5% in 21 days [41,45].

Despite the damaging effect of moisture on the perovskite, it has been noted in many reports the beneficial side of the humidity rate during the crystallization of the perovskite. Experience showed that, less than 30% of humidity during cell fabrication improves the morphology of crystal and enhances the performance of the device which avoids the presence of pinholes and grain boundaries that brakes charge transport and induces the

recombination at dry environment. Therefore, the pre-heating of the substrates is recommended before PbI_2 deposition to achieve best device performances. It has been found that in a 50% humidity environment when substrates were pre -heated at 50℃, a PCE of 15.76% was reported [41]. Thus, the pre-heating step is responsible for a better porous filling and surface coverage of the perovskite.

11.3.Effect of temperature (T)

Multiple researches have studied the effect of temperature on the perovskite layer, the performance of the perovskite based PV devices has been found to be higher at 39℃[55]. In ambient conditions, PSCs have to be subjected to elevated temperatures which can affect greatly the perovskite layer performance. The starting point is crucial whereas the perovskite layer requires an annealing temperature processing.

Low temperature annealing is normally used in the fabrication process of perovskite thin films for solar cells. It has been found that the annealing temperature has critical impact on the morphology of perovskite films, stability and photovoltaic performance of the devices. Experiments indicated that a minimum temperature of 80℃ is required to completely transform the precursor of MAI and PbI_2 to $MAPbI_3$. However, further increase of the annealing temperature would lead to the change of the $MAPbI_3$ perovskite morphology and formation of larger crystalline particles [45]. For instance, under dry environment, to isolate exclusively the effect of temperature on the film degradation, the influence of high temperatures on both $MAPbI_3$ and $MAPbI_{3-x}Cl_x$ films has been experimented. As a result, after heating the films at 100℃ for 20 min, a noticeable degradation of both perovskites was observed. Further heating at 200℃ led to the complete decomposition films into PbI_2. Very low thermal conductivity in both structures was reported. It has been explained that when heating up the device, the heat is not spread quickly enough and may cause mechanical stress decreasing the life time of the PSC device [47]. The PSC devices were really exposed to real conditions of temperature and UV light in Jeddah (Saudi Arabia) during one week. The same PCE was maintained and good stability after 7 days was exhibited [45]. The devices were made in filtrating the perovskite solution into a mesoporous TiO_2/ZrO_2 scaffold coated with carbon black back

contact and encapsulated with a glass sheet glued by Surlyn and epoxy resin for avoiding moisture penetration.

In another experiment, the effect of precursors such as PbI_2 and $PbBr_2$ for preparing the perovskite materials is studied and the results are compared. It has been found that $MAPbI_3$ device showed decomposition after 60 min between 44℃ and 55℃, in the same time $MAPbBr_3$ device did not suffer any degradation. This thermal stability can be attributed to the shorter and stronger bonds of Pb-Br compared to Pb-I [45]. The use of organic precursors is also tested, it has been noted that $FAPbI_3$ perovskite just decomposed at 290℃. Then, thermal stability of FA based devices is higher than that $MAPbI_3$ perovskite.

The thermal stability is usually linked to material's ability to endure high temperatures. To avoid the decomposition due to the high temperature, the best option is the use of thermal resistant materials, inorganic precursors use play an important role in the thermal stability of the device. Recently, it has been suggested that the use of Cs as a cation making a triple cation perovskite solar cells; like $Cs_{0.17}FA_{0.83}Pb(I_{0.83}Br_{0.17})_3$ and $Cs_{0.05}(MA_{0.17}FA_{0.83})_{0.95}Pb(I_{0.83}Br_{0.17})_3$ enhances the thermal stability and reproducible high efficiency (PCE of 18.3%) [43,51,54], while in latest approach, the use of single walled nano-tubes of carbon (SWNTs) fixed in non-conducting polymer matrix is recommended to hinder thermal degradation [54].

11.4.Effect of light illumination and ultra-violet light (UV) light

11.4.1. Effect on the perovskite absorber

Instability issues related to the continuous illumination of perovskites lie in two main processes such as the phase segregation and the photo-dissociation. According to (Reac(4)), all $MAPbX_3$ perovskites suffer a photochemical decomposition under UV light, which leads to the instability of PSCs. So, charge traps induced by the intrinsic defects can attract the photo-excited charge carriers and create localized trap states around the grain boundaries. Then, accumulated trap states under continuous illumination polarize the crystal system and form irregular electric fields, which increase the coupling between charge carriers and crystal lattice. An experiment test on $MAPbI_3$ layer, putted under continuous illumination and in vacuum for 24 h, has shown the change from one

single PL peak into double peaks, indicating the light induced phase segregation of and photo-dissociation of perovskites. It has been suggested that tuning the perovskite composition and select the appropriate substitution of A site cations with FA and Cs can annihilate induced phase segregation and improve the photo-stability of perovskites [43]. In addition, in order to reduce the UV induced oxidation of the perovskite, fluorinated perovskites have been suggested to use as absorber layers [45].

11.4.2.Effect on the electron transport material (ETM)

UV light can also lead to significant reduction of stability of PSCs by generating electrons-holes in TiO_2 layers that can react with oxygen absorbed at surface oxygen vacancies, which then develop into deep trap states leading to charge recombination.

It is well known that TiO_2 is a good photo-catalyst for oxidizing water and organic compounds and due to its 3.2 eV band gap it absorbs in the UV spectrum. Thus, several degradation mechanisms have been proposed based on the photo-activity of TiO_2 under UV illumination. Mesoporous TiO_2 incorporates trapping sites and surface defects working as electron donating sites. Electrons localized in these trapping states bind with oxygen and generate O_2^-. After illumination with UV light an electron-hole pair forms in the TiO_2 and the hole recombines with the electron at the oxygen adsorption site. Then, the oxygen desorbs, leaving an unoccupied site that could serve as a trap state for photo-induced electrons from sensitizers and holes in HTM may recombine with trapped electrons [41].

The tests realized on the TiO_2 layer for PSCs, under 1 sun (AM 1.5 G) within 5 h of illumination, showed that it is subjected to UV induced degradation. The measured efficiencies were investigated for TiO_2 based devices with and without encapsulation and a UV filter. The results showed that the encapsulated cell degraded very quickly compared to non encapsulated one [47].

To overcome the trap states problem, a Sb_2S_3 blocking layer at the TiO_2 / $MAPbI_3$ interface was proposed to reduce UV induced degradation. The inclusion of the Sb_2S_3 buffer layer improved the stability and maintained 65% of its initial efficiency after exposure to the 12 h compared to $MAPbI_3$ that decomposed into PbI_2 [47].

Many strategies were additionally proposed to overcome the instability originated by UV illuminated TiO_2 layer. The easiest one considered by insertion of UV filter [41]. Another consisted of using mesoporous insulating Al_2O_3 into PSCs instead of the TiO_2 nano-particles. This proposition reported long term stability of more than 1000 h at 40℃. However, PCE sharply decreased to 50% of its initial value in the first 200 h [54]. Alternatively, the Zn_2SnO_4 material used as ETM, which enhanced the crystallization of perovskite layer and annulled the UV spectrum; PSC device with Zn_2SnO_4 exhibited promising high stability without encapsulation over one month but accompanied with low PCE of 13.3% [41].

Recently, PSC included one dimensional photonic crystal (1DPC) to effectively eliminate the UV absorption in the TiO_2 layer of the PSCs [56].

11.5.Effect of deposition method

PSCs can be fabricated and processed through many techniques. The fabrication method can influence effectively the performances and the stability of PSCs.

In ambient conditions, the blade coating based planar PSC method enhanced its stability and photovoltaic performances which was attributed to the formation of large crystalline domains and uniform coverage of the perovskite thin film on TiO_2 film substrate. The perovskite films prepared by doctor blading showed better light absorption and stability compared to those processed by spin coating, measurement in air revealed that a reduction in photovoltaic performance associated with degradation of perovskite films fabricated by the spin coating method.

Moreover, $MAPbI_3$ film based PSCs made by hybrid chemical vapour deposition exhibited high efficiency of 11.8% and retained the same efficiency after 1100 h storage in dark and dry N_2 gas. The high temperature (above 160℃) used to make the film evaporated completely the excess of MAI and water which lead to less sensitivity to moisture and consequently the high stability of the cells [45].

Another method concerns alternating layer by layer vacuum deposition has reported a conservation of 91% of PCE of its initial value after 62 days of storage under ambient conditions. This high stability is related to the formation of compact and dense perovskite

film with full surface coverage that prevents moisture contamination. It has been signalled that solar cells used $Pb(OAc)_2$ as precursor showed lower stability with respect to those $PbCl_2$ as precursor for the preparation of $MAPbI_3$ [45].

11.6.Effect of electron transporting material (ETM)

The type of ETM can affect the stability and performances of PSC. It has been revealed that the solar cell with nano-rod based film combined with $TiCl_4$ post-treatment retained 60% of the initial efficiency after 55 days while the TiO_2 planar solar cell was found to shift from 12.1% initial value to 1% within 300 h. It has been suggested that this difference in stability is due to the crystallinity and chemical stability of the mesoporous nano-rod layer which assists more protection against humidity because of the blocking effect of the HTM above. In contrast, the rapid degradation in the planar structure was attributed to wide surface exposure to moisture, indicative to the decomposition into PbI_2. In other research, solar cells with TiO_2-ZrO_2 mesoporous layer showed a good stability of 1008 h at room temperature under AM 1.5 simulated sunlight. The rudimentary device architecture was FTO /mesoporous TiO_2 /$MAPbCl_3$ /Spiro-OMeTAD/Au, it demonstrated faster degradation after 30 days [45].

The mesoporous PSCs performances, using TiO_2 as ETM, can be reduced according to the presence of no-stoichiometric defects, such as oxygen vacancies and Ti interstitials that generate deep sub-band gap trap states. The passivity of these trap states consist of doping TiO_2 with Al using a sol gel deposition method is proposed. Low doping levels promoted to a decrease of trap states. Thus, an augmentation of Al-doped TiO_2 cell performances. Additionally, the stability of encapsulated devices was significantly improved with Al-doping.

Another attempt consists of replacing TiO_2 with SnO_2 nano-particles using spin coating method, annealed at 200℃ for 1 h. Using this layer in the PSC, an efficiency reached 13%. In term of stability, the SnO_2 solar cell resisted 700 h which was significantly more stable than the TiO_2 based devices, though, both SnO_2 and TiO_2 based devices degraded quickly only within 8 h under light soaking over long time exposure. In addition, the SnO_2 layer exhibited several advantages for thin film PSCs, such as good antireflection, suitable band edge positions and high electron mobility [47].

ZnO has also been recommended as effective ETM for high efficiency PSCs, the ZnO compact layer allows to enhance the stability of the perovskite layer.

11.7.Effect of hole transporting material (HTM)

Currently, the most widely used HTM is the Spiro-MeOTAD. It has been experienced that not only the perovskite itself suffers the degradation under moisture, temperature or illumination, but the widely used HTM, spiroOMeTAD, also does. So, many alternative HTMs have been adapted in PSCs where attempts to improve the stability of PSCs as a multilayer system, containing such HTM is needed.

Inorganic materials offer the potential for low cost and better stability for PSCs. It has been noted that the solar cells using CuI as inorganic HTM have exhibited better stability than those containing spiro-OMeTAD under continuous 2 h illumination, but with low efficiency. It has been also demonstrated that PSCs using carbon material as HTM and back contact retained 80% of their efficiency for 1008 h under 1 sun illumination in ambient air. The hydrophobic nature of the carbon toward moisture is the responsible cause for the high stability of the devices [45].

In early work, spiro-OMeTAD has been changed by a polymer functionalized single wall carbon nanotube (SWCNT). The efficiency FTO/TiO_2/Al_2O_3+$MAPbI_{3-x}Cl_x$ /PTAA/SWCNT-PMMA/Ag architecture reached 15.3%, this alternative showed excellent thermal stability and resistance to water of PSC devices. The presence of polytriarylamine polymer (PTAA) thin layer as HTM prevents unwanted metal migration effect into the perovskite layer. Thus, a reduction in the degradation enables the device stability [51].

Alternatively, this effect can also be mitigated by using buffer layers [48]. It has been demonstrated that the processing by atomic layer deposition (ALD) technique of ultrathin compact Al_2O_3 layer either beneath or above the spiro-OMeTAD HTM enhanced the stability of PSCs. A very thin layer of Al_2O_3 increased the quantum tunnelling of the holes which augmented the charge collection. Thus, solar cell of FTO/ TiO_2 /$MAPbI_3$ /spiro/Al_2O_3/Ag structure has been suggested to improve the stability. It has been concluded that the Al_2O_3 layer protected the perovskite materials from degradation by

moisture and sunlight as it acts as an insulator barrier between TiO_2 and HTM and retarding the electron recombination process.

Using C_{60} as HTM in PSC has been also tested to enhance the stability [45]. The device with ITO/polythiophene(PT)/$MAPbI_3$/C_{60} structure exhibited excellent stability and enhanced the efficiency after exposure to illumination of 100 mW/cm^2, AM 1.5 G irradiation in N_2 filled glove box at temperature of 25-35℃ over 816 h.

PEDOT:PSS and Spiro-OMeTAD possess high charge extraction character. However, poly(3,4-ethylenedioxythiophene) polystyrene sulfonate (PEDOT:PSS) has been found to reduce the performances of PSCs and Spiro-OMeTAD suffers low conductivity which result in device instability. In fact, Spiro-OMeTAD need dopants or additives like lithium salt to increase its conductivity, while the salts are very sensitive to moisture, the inclusion of O_2 and H_2O was found to act like p-type dopants and induce the Fermi level shifts toward the HOMO of Spiro-OMeTAD which would possibly resulting in the further performance degradation [43]. Hence, Doping HTM with bis(trifluoromethane) sulfonimide lithium salt (Li-TFSI) or tetra-thiafulvalene derivative (TTF-1), is required to allow high performance. However, it has been found that the doped Spiro-OMeTAD devices with about 11% degraded 3 times quicker than the un-doped ones.

It has been found that using p-type NiO_x and n-type ZnO nano-particles as HTM and ETM, in the PSC devices reached a PCE of 16.1% and retained 90% of this initial value for 60 days of storage in air at room temperature. For example, the structure made of glass/(ITO)/NiOx/perovskite/ZnO/Al showed a good stability in ambient conditions, thus isolating the perovskite and Al layers and preventing degradation [41].

An investigation on the influence of the cheap poly(3-hexylthiophene) P3HT, and poly-bis(4-phenyl)(2,4,6-trimethylphenyl) PTAA as HTMs instead of Spiro-OMeTAD showed that a rapid degradation of the perovskite film was observed. The polycarbonate (PC), as an insulator combined with (SWNTs) has been suggested to enhance the conductivity, thus the stability of the devices. Indeed, devices fabricated with P3HT/SWNT - PC as HTLs increased the efficiency from 13.3% to 14.3% with an exposure time of 96 h [47].

In reported experiment, a thin polythiophene (PT) film of 5 nm, deposited by electrochemical polymerization, is proposed to replace PEDOT:PSS [47]. The efficiency

for PT/$MAPbI_3$ based devices achieved 15.4%, and remained stable for 816 h when tested under constant illumination in a nitrogen filled glove box.

Different approach to replace the unstable Spiro-OMeTAD consists of the synthesis of a conductive oligothiophene, DR3TBDTT, as a HTM in a planar PSC [47]. This material is characterised by higher intrinsic hole mobility, removing the necessity of p-type doping proposed previously. Additionally, this material is hydrophobic and characterized by the large water contact angle. Adding a small amount of polydimethylsiloxane (PDMS) to the proposed HTM allowed smoothing its poor surface coverage. The device performance of planar PSCs including a (DR3TBDTT+PDMS) HTM was (8.8%). It has been noted that the increased hydrophobicity of (DR3TBDTT + PDMS) HTM devices enhanced its stability (from 8.8% to 8% only) after 3 days.

11.8.Effect of encapsulation

Encapsulation of the PSC devices play a main role in the commercialisation of perovskite solar cells as it prevents the contact of different solar cell with moisture; hence, it avoids perovskite material degradation. The principle of encapsulation resides in the use of epoxy as encapsulant for the improvement of PSCs stability and performance. The first encapsulation test is applied when the Sb_2S_3 layers were inserted at the interface between TiO_2 ETM and $MAPbI_3$ perovskite where inorganic CuSCN worked as HTM. It has been remarked that PCE of the PSC were improved with Sb_2S_3 layers but the encapsulated cell was dropped to zero efficiency in just 12 h [57].

In an investigation study, it has been demonstrated that the use of 50 nm Al_2O_3 layer through ALD technique on top of PSCs as an encapsulant enhanced the stability of PSCs by preventing moisture spread. Under (45℃-85% RH), the PSC structure Al_2O_3 encapsulate perovskite/HTM/Au devices deteriorated after 72 h which demonstrate the effectiveness of Al_2O_3 as a suitable moisture barrier [56].

In recent work, exposure of the fabricated PSCs such as (PET-IZO-TiO_2-$MAPbI_3$-SM-Au) devices to ambient humid room temperature exhibited that the encapsulated device is more stable compared to the un-encapsulated one. It has been found the initial PCE of 12 % was maintained over 500 h while the non-encapsulated PSC deteriorated rapidly and badly performed in just 100 h [59].

At the industrial level, different types of sealing procedures based on thermal plastics and light resistant resins are studied. It has been found that, (Kapton, DuPont, United States) that used an adhesive encapsulation procedure is among the best ones compared to the light curable glue (Henkel, Germany) or the UV curable glue (ThreeBond, United States) as edge sealant [41]. These devices resulted only a 2% PCE decrease after 170 h. At most, it is due to thermal degradation of spiroOMeTAD, as well as the UV degradation of different layer constituting the PSC. (Viewbarrier, Mitsubishi Plastic, Japan) proposed, for flexible PSCs, a plastic barrier sealant adhesive that was laminated at 100℃ onto the flexible device back contact [41]. More recently, carbon conductive tapes back contact is laminated above the perovskite layers with good adhesion. It had two main functions in the same time; being back contact and sealant, which reduces the fabrication costs of the device.

11.9.Effect of electrodes

Generally, high efficiency PSCs used gold as electrode material. So finding costless electrode materials is required. Ag material has been suggested as an alternative electrode choice. It has been demonstrated that Ag failed to replace the gold as an electrode in either for its worse environmental stability or low PCE. It has been demonstrated that exposure of PSCs using Ag electrode to humidity (50% RH) led to the decomposition of the perovskites layer and then to the formation of AgI [47].

The effect of electrodes deposition method is important in the transition towards PSCs scalable processing. For example, the triple layer device, including mesoporous TiO_2/ZrO_2, $(5\text{-}AVA)_x(MA)_{1-x}PBI_3$ / carbon layer, The carbon layer was a 10 mm thick deposited using a screen printing technique. This device structure displayed to a certified efficiency of 12.84% as well as an excellent stability for 1008 h under ambient conditions and exposure to AM 1.5G simulated sunlight. It has been indicated that the thick carbon layer provided excellent protection. However, high temperature processing (450℃) of this device architecture is harmful for the desired mass production [47].

The progress of carbon layer deposition has attracted more interest for electrodes in PSCs. Inclusion of thermoplastic carbon film in a device removed the need for the HTM and metal electrode. $MAPbI_3$ based device achieved high PCE of 13.53% under 1 sun

illumination. The 40 mm carbon layer behaved as a form of encapsulation which protects the cell from moisture, the study revealed that the device showed an excellent when the PCE of the device with this carbon electrode only reduced from 13.53% to 12.87% after 20 days of storage, in the dark, under ambient conditions [47].

In recent study, to hinder the degradation of the perovskite layer, hydrophobic materials used to efficiently inhibit the moisture. Thus, these materials could be integrated into the fabrication process. It has been found that the good choice of the counter electrode further reduced the rate of deterioration of the devices, because metal electrodes can easily subjected to oxidation and formation of halides in the presence of moisture. In the commonly used Au electrodes, the redox I / I^- system is reactive with Au forming AuI_3^- /AuI_3 reactants. It has been proposed that Cr/Cr_2O_3 interlayer could protective the metal counter electrode from chemical reactive reaction caused by iodine liberated from the $MAPbI_3$ perovskite layer. Buffered devices that included the Cr/Cr_2O_3 layer exhibited better stability than devices without the layer [59].

12. Conclusion

The organometallic halide perovskite OMHP are among the best photovoltaic materials; their electronic properties such as electronic band gap, density of states,... can be tuned through doping on sites A, B and/or X in the perovskites structure ABX_3. The OMHPs are also characterized by their high absorption coefficient which makes them appropriate candidates to include in the PV solar cells.

The OMHPs are materials appear to be sensible for temperature gradient and can undergo different phase transitions from low temperature orthorhombic system to tetragonal and then high temperature cubic system, which provides many scopes to apply them beside the photovoltaic application.

Organometallic halide perovskite solar cells (OMH-PSCs) are considered as one of the rising PV technology due to their high efficiency, low-temperature processing, and easy fabrication techniques where the most cited are the one step deposition (OSD) method and sequential deposition method (SDM), vapor assisted solution process (VASP),

chemical vapor deposition (CVD), thermal vapor deposition (TVD) method, and microwave irradiation process (MIP)...

In another hand, some methods are devoted to the issue of large scale processing such as doctor blading, slot die coating, roll-to-oll coating, meniscus-assisted solution printing, soft-cover coating, spray coating and inkjet printing.

In this chapter, the mechanism of the $MAPbI_3$ perovskite as p-i-n junction is briefly explained to understand the PSC as unit device and dependent layered system which allows to describe precisely the PSC performances and stability.

The PSC is constituted basically of perovskite absorber material, ETM, HTM and electrodes. A summary of the most important factors pertaining to PSC degradation is presented. These effects can be related to the perovskite absorber itself or to the other solar cell device layers. In this work, the causes affecting the stability of PSC are not grouped into intrinsic and extrinsic factors but in such a way to fully describe the device stability as interference system. The most reported factors are the atomic composition and the perovskite structure, moisture (humidity), temperature, UV illumination, fabrication methods, the types of used ETL, HTL and electrodes and the encapsulation effect.

The examination of all cited results discussing PSC stability reveals that the sensitivity to moisture is the primary concern of $MAPbI_3$ rapid decomposition under high RH. From this point, multiple attempts have been proposed to design the best stable alternative perovskite materials. The trivial strategy to improve the inherent instability of $MAPbI_3$ is by atomic substituting with respect to the stability descriptor; t, μ, $(t+\mu)^n$,...of the ABX_3 structure. It has been found that the inclusion of Br and Cl instead of I or the combination of both in the X site can enhance the stability of the PSC. In addition, insertion of FA, CsFAMA, CsFA, CsFAMA and RbCsFAMA in the A site has greatly improved the efficiency and long term stability of PSCs. Meanwhile lead free PSC failed to select Sn as environmentally stable perovskite. Another approach towards the stability consists of the dimensionality of the perovskite when the (2D) PEA instead of MA has been suggested to enhance the stability of the PSC. Atomic substitution also helps to improve the perovskite absorber stability and performances against thermal degradation, phase segregation and photo-dissociation caused by UV irradiation elevated temperatures.

Different stress factors, including with UV irradiation and thermal decomposition, also affect greatly non absorber layer such as ETM, HTM and electrodes. Mainly, the perovskite absorber is sandwiched between the charge transport materials ETM and HTM that should be hydrophobic and should not react with the perovskite absorber. They can be an insulator barrier and encapsulate the PSC to protect it from the decomposition under moisture, temperature or UV irradiation.

In order to enhance the PSC stability, it has been found that the widely used TiO_2 as ETM can be substituted by SnO_2 or ZrO_2 materials or doped with small amount of Al. Encapsulation using insulting layers which are Sb_2S_3 or Al_2O_3, Zn_2SnO_4 as well as including 1D photonic crystals has excellently improved the stability and the efficiency of the PSC.

In another side, the commonly used HTM is Spiro-OMeTAD. It has been concluded that it is characterised by low conductivity. Suggested approaches consist of replacing it with CuI, SWCNTor NiO_x , DR3TBDTT materials as HTM to increase the PSC long time durability. Spiro-OMeTAD can be also encapsulated by Al_2O_3 or C_{60} buffer layers.

Also, to overcome the reactive system AuI_3^-/AuI_3 in the electrodes, a Cr/CrO_3 protecting layer is used at the interface. In addition, the Au alternatives should be cost effective and stable. It has been found that the thermo-plastic carbon is a good choice since it functions as HTM and electrode whist Ag electrode doesn’t reach the desired PCE.

Perovskite solar cell design is of importance, because it includes the mesoscopic structure or the planar structure. Moreover, the PSC device fabrication method has been evolved as an important factor influencing the stability and performances of the perovskite solar cell. It has been cited that perovskite absorber synthesis through blade coating, hybrid chemical vapor processing or alternating layer by layer deposition helps to enhance the PSC stability. Furthermore, the ALD technique has been used in encapsulated solar cell devices.

13. References

[1].P. Billen, E. Leccisi, S. Dastidar d, S. Li d, L. Lobaton, S. Spatari, A. T. Fafarman, V. M. Fthenakis, J. Baxter. Comparative evaluation of lead emissions and toxicity potential in the life cycle of lead halide perovskite photovoltaics. 2019. Energy. Elsevier.

[2].Best Research-Cell Efficiencies. NREL Transfonming Energy. 2019.

[3].Q. Lin A. Armin, P. L. Burn, and P. Meredith. Organohalide Perovskites for Solar Energy Conversion. 2015. Accounts of Chemical Research. ACS Publications.

[4].S. H. Chang, HM Cheng, S. Hui Chen and K. F Lin. Optical, Excitonic, and Electronic Properties of CH3NH3 PbI3 Thin Films and Their Application in Photovoltaics. 2016.Nanoelectronics and materials development. Intech.

[5].B. M. Soucase, I. G. Pradas and K. R. Adhikari. Numerical Simulations on Perovskite Photovoltaic Devices. 2016.Nanoelectronics and materials development. Intech.

[6].N. F. Atta, A. El-Ads. Perovskite Nanomaterials – Synthesis, Characterization, and Applications. 2016.Nanoelectronics and materials development. Intech

[7].H. Kim, K. G. Lim, T. Lee. Planar Heterojunction Organometal Halide Perovskite Solar Cells: Role of Interfacial Layers. 2015. Energy & Environmental Science. RSC Publishing.

[8].S. F. Hoefler, Gregor Trimmel and Thomas Rath. Progress on lead-free metal halide perovskites for photovoltaic applications: a review. 2017. Monatsh Chem. Springer.

[9].H. Fu. Review of lead-free halide perovskites as light-absorbers for photovoltaic applications: From materials to solar cells. 2019. Solar Energy Materials and Solar Cells. Elsevier.

[10].K. Shen, H. L Sun, G. Ji,Y. Yang, Z. Jiang and F. Song. Fabrication and Characterization of Organic–Inorganic Hybrid Perovskite Devices with External Doping. 2016.Nanoelectronics and materials development. Intech

[11].C. Li, X. Lu, W. Ding, L. Feng, Y. Gao and Z. Guo. Formability of ABX_3 (X = F, Cl, Br, I) halide perovskites. 2008. Acta ceystallographica B. V64. Pp 702-707.

[12].P. G. Fernandez, J.A. Aramburu, M.T. Barriuso, and M. Moreno. Key Role of Covalent Bondin g i n Octahedral Tilting in Perovskites. 2009. The Journal of Physical chemistry Letters. ACS Publications.

[13].A. S. Verma and V. K. Jindal. Perovskites: Structure, Properties and Uses ; Abx3-type oxides and halides: their Structure And physical properties. 2010. Nova Science.

[14].H. Zhang, X. Qiao, Y. Shen, T. Moehl, S. Zakeeruddin, Michael Graetzel and M. Wang. Photovoltaic Behaviour of Lead Methylammonium Triiodide Perovskite Solar Cells Down to 80 K 2015. Journal of Materials Chemistry A. The Royal Society of Chemistry.

[15].C. Roiland. G. Trippé-Allard, K. Jemli, B. Alonso, J. Ameline, Régis, Gautier,T. Bataille, L. Le Pollès, E. Deleporte, J. Even, C. Katan. Multinuclear NMR as a tool for studying local order and dynamics in $CH_3NH_3PbX_3$ (X = Cl, Br, I) hybrid perovskites. 2016. Physical Chemistry Chemical Physics. Royal Sociaty of Chemistry.

[16].P. Umari, E. Mosconi and F. D. Angelis. Relativistic GW calculations on $CH_3NH_3PbI_3$ and $CH_3NH_3SnI_3$ Perovskites for Solar Cell Applications. 2014. Scientific reports. Nature.

[17].E. Mosconi, A. Amat, Md. K. Nazeeruddin, M. Gratzel, and F. D. Angelis. First-Principles Modeling of Mixed Halide Organometal Perovskites for Photovoltaic Applications. 2013. The Journal of Physical Chemistry C. ACS Publications.

[18].A. Poglitsch and D. Weber. Dynamic disorder in methylammonium trihalogenoplumbates (II) observed by millimeter-wave spectroscopy. 1987. The Journal of Chemical Physics. American Institute of Physics.

[19].D. Luo, L. Yu, H. Wang, T. Zou, L. Luo, Z. Liu and Z. Lu. Cubic structure of mixed halide perovskite $CH_3NH_3PbI_{3-x}Cl_x$ by thermal annealing. 2015. RSC Advances.

[20].T. Oku, T. Matsumoto, A. Suzuki and K. Suzuki. Fabrication and Characterization of a Perovskite-Type Solar Cell with a Substrate Size of 70 mm. 2015. Coatings. MDPI.

[21].M. Cadelano, M. Saba, N. Sestu, V. Sarritzu, D. Marongiu, F. Chen, R. Piras, F. Quochi, A. Mura and G. Bongiovanni. Photoexcitations and Emission Processes inOrganometal Trihalide Perovskites. 2016. Nanoelectronics and materials development. Intech

[22].B. A. Rosales, L. Men, S. D. Cady, M. P. Hanrahan, A. J. Rossini, and J. Vela. Persistent dopants and phase segregation in organolead mixed-Halide Perovskites. 2016. Chemistry of Materials. ACS Publications.

[23].E. Ivano, C. Garcıa-Lastra, S. Kristian. Thygesen, and Karsten W. Jacobsen. Bandgap calculations and trends of organometal halide perovskites. 2014. APL Materials 2, 081514

[24].C. S. Ponseca Jr. Charge Carrier Dynamics in Organometal Halide Perovskite Probed by Time-Resolved Electrical Measurement. 2016.Nanoelectronics and materials development. Intech.

[25].C. C Stoumpos, C. D. Malliakas, and M. G. Kanatzidis. Semiconducting Tin and Lead Iodide Perovskites with Organic Cations: Phase Transitions, High Mobilities, and Near-Infrared Photoluminescent Properties. 2018. Inorganic chemistry. ASC Publications.

[26].Z. Xiao, W. Meng, J. Wan, D. B. Mitzi, and Y. Yan. Searching for promising new perovskite-based photovoltaic absorbers: The importance of electronic dimensionality. 2016. Materials Horizons. Royal Society of Chemistry.

[27].N. K. Kumawat, M. N. Tripathi, U. V. Waghmare, and D. Kabra. Structural, Optical and Electronic Properties of Wide Bandgap Perovskites: Experimental & Theoretical Investigation. 2016. The journal of Physical Chemistry A. ACS Publications.

[28].E. Mosconi, P. Umari, F. D. Angelis. Electronic and optical properties of mixed Sn / Pb organohalide perovskites: A first principles investigation. 2014. Journal of Materials Chemistry A. Royal Sociaty of Chemistry.

[29].J. Im, C. Stoumpos, H. Jin, A. Freeman, and M. G. Kanatzidis. Antagonism between Spin-Orbit Coupling and Steric Effects Causes Anomalous Bandgap Evolution in the Perovskite Photovoltaic Materials CH3NH3Sn1-xPbxI. 2015. The Journal Physical Chemistry Letters.ACS Publications.

[30].J. J. Choi and J. Simon. L. Billinge. Perovskites at the nanoscale: from fundamentals to applications. 2016. Nanoscale. Royal Society of Chemistry.

[31].L. Z. Robert. E. Riley. Brandt, A. Osherov,V. Stevanovic SamuelD.Stranks, W. B. Mark. Wilson, H. Kim, Austin J. Akey. John D. Perkins, R. Kurchin, J.R. Poindexter, N Evelyn. M. G. Wang,. B.V. Bulovic. and T. Buonassisi. Methylammonium Bismuth Iodide as a Lead-Free,Stable Hybrid Organic–Inorganic SolarAbsorber. 2016. CHEMISTRY. Wiley.

[32].S. Qing, O. Yuhei, T. Taro, Y. Kenji and H. Shuzi. Optical Absorption, Charge Separation and Recombination Dynamics in Pb and Sn/Pb Cocktail Perovskite Solar Cells and Their Relationships to the Photovoltaic Properties. 2016.Nanoelectronics and materials development. Intech

[33].Y. Zhao and K. Zhu. Organic–inorganic hybrid lead halide perovskites for optoelectronic and electronic applications. 2015. Chem. Soc Rev. Royal Society of Chemistry. V.45, 655-689.

[34].W. Dunlap-Shohl, Y. Zhou, N. P. Padture, and D. B. Mitzi. Synthetic approaches for halide perovskite thin films. 2018. Chemical Reviews. ACS Publications.

[35].M.S. Jamala,b, M.S. Basharb, A.K. M Hasana, Z. A. Almutairi, Hamad F. Alharbic, N. H. Alharthi, M. R. Karime, H. Misranf, N. Amin, K. Bin Sopian, Md. Akhtaruzzaman. Fabrication techniques and morphological analysis of perovskite absorber layer for high-efficiency perovskite solar cell: A review. 2018. Renewable and Sustainable Energy Reviews. Elsevier. V.98. 469-488

[36].M. Petrovic, V. Chellappan, S. Ramakrishna. Perovskites: Solar cells and engineering applications – materials and device developments. 2015. Solar Energy. Elsevier.

[37].P. Tanaji. Gujar and M. Thelakka. Highly reproducible and efficient perovskite solar cells with extraordinary stability from robust $CH_3NH_3PbI_3$ towards large area devices. 2016. Energy Technology. Wiley.Online Librery.

[38].A. R. bin Mohd Yusoff, and M. K. Nazeeruddin. Organohalide Lead Perovskites for Photovoltaic Applications. 2016. The Journal of Physical Chemistry Letters. ACS Publications.

[39].N. Park. Perovskite solar cells: an emergingphotovoltaic technology. 2015. Materials Today. V18. N2, Elsevier.

[40].G. Eperon, S. D. Stranks, C. Menelaou, M. B. Johnston, L. M. Herz and H. J. Snaith. Formamidinium lead trihalide: a broadly tunable perovskite for efficient planar heterojunction solar cells.2014.V7.982-988. Energy and Environmental Science.

[41].Mesquita I, Andrade L, Mendes A. 2018. Perovskite solar cells: Materials, configurations and stability. Renewable and Sustainable Energy Reviews. vol 82. 2471-2489.

[42].Domanski K. 2018. The Quest for Stability of Perovskite Solar Cells: Understanding degradation, improving life time sand towards experimental standards. École polytechnique fédérale de Lausanne. These n (8106).

[43].Yang J, Luo Y, Bao Q, Li Y, and Tang J. 2018. Recent advances in energetics and stability of metal halide perovskites for optoelectronic applications. 2018. Advanced Materials and Interfaces. 1801351-18013576.

[44].Shojaei F and Jian Yin W.2018. Stability trend of tilted perovskites. Journal of Physical Chemistry. 15214-15219.

[45].Shahbazi M, Wang H. 2016. Progress in research on the stability of organometal perovskite solar cells. Solar Energy. Vol 123. 74-87.

[46].Ghosh D, Yusuf Ali Md., Chaudhary D., Bhattacharyy S. 2018. Dependence of halide composition on the stability of highly efficient all-inorganic cesium lead halide perovskite quantum dot solar cells. Solar Energy Materials and Solar cells. Vol 185. 28-35.

[47].Wang D, Wright M, Elumalai N, Ashraf Uddin. 2016. Stability of perovskite solar cells. Solar Energy Materials and Solar Cells. Vol 147. 255-275.

[48].Saliba M, Matsui T, Domanski K, Seo J, Ummadisingu A, Zakeeruddin S., Baena J, Tress W., Abate A, Hagfeldt A, Grätzel1M. 2016. Incorporation of rubidium cations into perovskite solar cells improves photovoltaic performance. Solar cells. Vol 354.

[49].Saliba M, Matsui T, Seo J, Domanski K, Baena J, Khaja Nazeeruddin M, Zakeeruddin S, Tress W, Abate A, Hagfeldt A, and Grätzel M. 2016. Cesium-containing triple cation perovskite solar cells: improved stability, reproducibility and high efficiency. Energy and Environmental Science.

[50].Rehman W, McMeekin D., Patel., Milot R., Johnston M., Snaith H and Herz L.2016. Photovoltaic mixed-cation lead mixed-halide perovskites: links between crystallinity, photo-stability and electronic properties. Energy and Environmental Science.

[51].Holzhey P, Yadav P, Turren-Cruz S, Grätzel M, Hagfeldt A, Saliba M. 2017. A chain is as strong as its weakest link – Stability study of $MAPbI_3$ under light and temperature. Materials Today.

[52].Körbel S, Marques M and Bott S. 2018. Stable hybrid organic-inorganic halide perovskites for photovoltaics from ab-initio high-throughput calculations.. Journals of Materials Chemistry A.

[53].Fujihara,T. Terakawa,S. Matsushima T., Qin,C. Yahiro M. and Adachi C. 2017. Fabrication of high coverage $MASnI_3$ perovskite films for stable, planar hetero-junction solar cells. Journal of Materials Chemistry C.

[54].Salhi B., Wudil Y.S., Hossain M.K. , Al-Ahmed A., Al-Sulaiman F.A. 2018. Review of recent developments and persistent challenges in stability of perovskite solar cells. Renewable and Sustainable Energy Reviews. Vol.90. 210-222.

[55].Adhikari K. Gurung S, . Bhattarai B, and Marí B.2015. Dependence of perovskite solar cells performance on temperature and solar irradiation.

[56].Zheng L, Xuan Y. 2018. Suppressing the negative effect of UV light on perovskite solar cells via photon management. Solar Energy. Vol 173. 1216-1224.

[57].Ito S, Tanaka S, Manabe K, and Nishino H.2014. Effects of surface blocking layer of Sb_2S_3 on nanocrystalline TiO_2 for $CH_3NH_3PbI_3$ perovskite solar cells. The Journal of Physical Chemistry C.

[58].Choi Y, Kim J, Limc S , Han E , Anita Ho-Baillie W.Y. , Park N.2018 . Enhancing stability for organic-inorganic perovskite solar cells by atomic layer deposited Al_2O_3 encapsulation. Solar Energy Materials and Solar cells. Vol 188. 37-45.

[59].Popoola I., Gondal M., Qahtan T. Recent progress in flexible perovskite solar cells: Materials, mechanical tolerance and stability.

CHAPTER 2

DFT for Perovskite Materials Modeling

1. Introduction

The underlying mechanisms that govern the physics and chemistry of organo-metallic halide perovskites (OMHP) are investigated by describing their structural, electronic and other fundamental properties. These properties are not trivial to find and a lot of computational studies within the latest years are focusing on establishing the accurate results when compared to the experimental ones. Specific modeling approaches provide the calculation of many interesting OMHP properties, where the density functional theory (DFT) is considered a modern method and one of the best powerful approach for modeling perovskite materials. The first sight of this chapter aims principally at illustrating the DFT by giving the physical meaning behind the DFT equations. The other sight is devoted to the recent results of electronic bad gap structures of some OMHP which are obtained using new DFT functionals with an without inclusion of spin orbit coupling and Van Der Waals interactions.

2. DFT over the time

Density functional theory (DFT) is considered among the very effective methods in computational modeling of materials from first principles. It is useful in studying molecules, nanostructures, solids, surfaces and interfaces, by directly solving approximate versions of the Schrödinger equation [1]. In this thesis, some historical passages as important foundations in the development of DFT are especially worthy of notice:

- Density functional theory is founded firstly by Hohenberg and Kohn theorem in 1964. Then, the Kohn-Sham equations are formulated using the concept of density functional by Kohn and Sham in 1965.
- The density functional theory is extended to include relativistic effects, it is approved by Von Barth and Hedin in 1972, shortly afterwards by Rajagopal and Callaway in 1973. The theory finds applications in magnetic materials investigation.

➢The beginning of DFT calculations for real materials, when the local density approximation (LDA) for the exchange and correlation energy is modeled as a function of density by Ceperley and Alder in 1980, then by Perdew and Zunger in 1981.

➢The DFT is extended from the stationary case formulae (energy ground state) to the excited states including time-dependent density functional theory. The theory is conceptualized by Runge and Gross in 1984 and has offered the possibility to study the optical properties of materials.

➢Density functional perturbation theory is introduced in 1987 by Baroni, Giannozzi and Testa which was applied on the of phonon dispersion calculations and describing vibrational properties.

➢The generalized gradient approximation (GGA) is applied to density functional and approved by Perdew, Burke and Ernzerhof in 1996 where the density first derivative (gradient) is added in the density functional form of the exchange and correlation energy. The accuracy of the total energy of systems is improved from 1 eV in the case using LDA to 0.1 eV using the GGA.

3. Material modeling derivation

3.1. Many-body Schrodinger equation:

As the derivation source of DFT models came out of the Schrödinger equation, the aim of this chapter is to show the key ideas related to the quantum theory of materials and to stimulate an intuitive physical sense to the sequencing of DFT derivation rather than plunging into the details and complications of the mathematic tools governing the DFT theorems and equations.

Many existing models describe the wave-particle duality, where the Schrödinger equation is considered the famous one. The time-independent Schrödinger equation for stationary electronic states of the many body wavefunction is principally described as [1]:

$$H\Psi = E_{tot}\Psi \qquad (3)$$

where H is the Hamiltonian operator and E_{tot} is the total energy eigenvalue of the system in the quantum state and Ψ is the many-body wavefunction.

The Hamiltonian function is the sum of the kinetic energy (T) and the Coulomb potential energy (V). It can be written as [1]:

$$H=T+V \tag{4}$$

If $$T=-\sum_i \frac{\hbar^2}{2m_e}\nabla_i^2 - \sum_I \frac{\hbar^2}{2M_I}\nabla_I^2 \tag{5}$$

and $$V=\frac{1}{2}\sum_{i\neq j}\frac{e^2}{4\pi\varepsilon_0}\frac{1}{|r_i-r_j|}+\frac{1}{2}\sum_{I\neq J}\frac{e^2}{4\pi\varepsilon_0}\frac{Z_I Z_J}{|R_I-R_J|}-\sum_{i,I}\frac{e^2}{4\pi\varepsilon_0}\frac{Z_I}{|r_i-R_I|} \tag{6}$$

then, the expression of many-body Schrödinger of (eq.3) is rewritten as [1]:

$$\left[-\sum_i \frac{\hbar^2}{2m_e}\nabla_i^2 - \sum_I \frac{\hbar^2}{2M_I}\nabla_I^2 + \frac{1}{2}\sum_{i\neq j}\frac{e^2}{4\pi\varepsilon_0}\frac{1}{|r_i-r_j|}+\frac{1}{2}\sum_{I\neq J}\frac{e^2}{4\pi\varepsilon_0}\frac{Z_I Z_J}{|R_I-R_J|}-\sum_{i,I}\frac{e^2}{4\pi\varepsilon_0}\frac{Z_I}{|r_i-R_I|}\right]\Psi = E_{tot}\Psi \tag{7}$$

With m_e, is the electron mass from i (electron) to N (electron) at positions $r_1, r_2, \ldots r_i, \ldots r_N$ in the system and M is the nucleus mass from I (nucleus) to M (nucleus) at coordinates $R_1, R_2, \ldots R_i, \ldots R_M$ in the system

Taking an easy example that describes the electrons/nuclei interactions in the silicon (Si). The volume of the unit cell of silicon (Si) in the diamond structure is a $(\frac{a^3}{4})$ with a=5.43 Å. In one hand, if the mesh spacing is $\Delta x \sim 0.1$ Å. Hence, $N_{\text{points}}=(\frac{a^3}{4})/(\Delta x^3)\sim 46{,}000$ points (volume element). In other hand, the silicon unit cell of (2 atoms) has 4 valence electrons for each atom, so $N+M=(2\times4)$(electrons)+2(nuclei)=10 particles. In last, for a complete many–body quantum state $\Psi_{Si}(r_1, \ldots r_8; R_1; R_2)$, the obtained low energy states number is $(N+M)^{Npoint} = 10^{46}$) complex numbers which is obviously impossible to get. As a result, the size of the system creates an exponential wall [1], which increase the complexity to resolve the many-body Schrödinger equation.

In quantum mechanics, the many-body Schrödinger equation (eq.7) is commonly expressed with the sophisticated Hartree atomic units [1] as:

$$\left[-\sum_i \frac{\nabla_i^2}{2} - \sum_I \frac{\nabla_I^2}{2M_I} + \frac{1}{2}\sum_{i\neq j} \frac{1}{|r_i - r_j|} + \frac{1}{2}\sum_{I\neq J} \frac{Z_I Z_J}{|R_I - R_J|} - \sum_{i,I} \frac{Z_I}{|r_i - R_I|}\right]\Psi = E_{tot}\Psi \quad (8)$$

3.2. Clamped nuclei approximation

The first concept towards DFT derivation rises from the solid nature of crystals and molecules adsorbed on solid surfaces where the nuclei typically remain fixed. According to the heavy weights of nuclei with respect to electrons, the approximation assumes that the nuclei are clamped in known positions [1].

Applying the clamped nuclei approximation, M_I=∞, implies that the kinetic energy of the nuclei is neglected ($\sum_I \frac{\nabla_I^2}{2M_I} \approx 0$) and the Coulomb repulsion between nuclei ($\frac{1}{2}\sum_{I\neq J} \frac{Z_I Z_J}{|R_I - R_J|} = constant$) is a constant. As well as naming $V_n(r)$ as the Coulomb potential of the nuclei experienced by the electrons such as:

$$V_n(r_i) = -\sum_I \frac{Z_I}{|r - R_I|} \quad (9)$$

Therefore, the fundamental equation of electronic structure theory is defined as

$$\left[-\sum_i \frac{\nabla_i^2}{2} + V_n(r_i) + \frac{1}{2}\sum_{i\neq j} \frac{1}{|r_i - r_j|}\right]\Psi = E\Psi \quad (10)$$

3.3. Mean field approximation

Now, taking the Coulomb repulsion into account, when a distribution of electronic charge $n(r)$ generates an electrostatic potential called Hartee potential $V_H(r)$, it is the effective field (not local but averaged) experienced by each electron, it is defined as [1]:

$$V_H(r) = \int dr' \frac{n(r')}{|r - r'|} \quad (11)$$

This second step towards DFT derivation is qualified as the mean-field approximation.

For a single-particle representation, the expression of (eq.10) can be expressed as [1]

$$\left[-\frac{\nabla^2}{2} + V_n(r_i) + V_H(r)\right]\Phi_i(r) = \varepsilon_i \Phi_i(r) \quad (12)$$

where $n(r) = \sum_i |\Phi_i(r)|^2$ (13)

with Φ_i is the lowest energy (ε_i) single particle wavefunction.

3.4. Hartree-Fock equations

The description of materials according to the mean field approximation lacks the quantitative accuracy required to investigate materials at the atomic scale because it needs, at the quantum level, to interpret the exchange interaction between identical particles as well as the electronic correlation when an electron moves and influenced by other electrons.

The best feature of Hartree-Fock equations provides that the electron can be treated as quantum [2] in which the non-local potential $V_X(r,r')$, called Fock exchange potential, is added to (eq.11). The Fock exchange potential is written as [1]:

$$V_X(r,r') = -\sum_j \frac{\Phi_j^*(r)\Phi_j(r)}{|r-r'|} \quad (14)$$

(Eq14) shows that the physical meaning of the potential V_X arises from Pauli's exclusion principle which prevents two electrons of wavefunction $\Phi(r)$ and antisymmetric wavefuntion $\Phi^*(r)$ from occupying the same quantum state.

Then, by replacing (eq.14) in (eq.12), the Hartree-Fock equations for single particle is[1]:

$$\left[-\frac{\nabla^2}{2} + V_n(r_i) + V_H(r)\right]\Phi_i(r) + \int dr' V_X(r,r')\,\Phi_i(r') = \varepsilon_i \Phi_i(r) \quad (15)$$

3.5. Kohn-Sham equations

The final step towards DFT equations is by considering the effect of the correlation between electrons. Inversely to the independent electrons approximation [3], within the Coulomb repulsion, the probability of finding electron 1 at position r_1 and electron 2 at r_2 is less than the product of the individual probabilities of finding each electron at the position r_1, r_2 respectively [4].

This wavefunction correlation character allows to add a new component which is the correlation potential $V_c(r)$ to the potential $Vn(r)+V_H(r)+V_X(r,r')$ in the single-particle equations (eq.15). In another hand, $V_X(r,r')$ is replaced by the so named local (simplified) exchange potential $V_x(r)$, only depends on one space coordinate. Then (eq.15) of is a single-particle immersed in Coulomb potential at the atomic scale is arranged as [1]:

$$\left[-\frac{\nabla^2}{2} + V_n(r) + V_H(r) + V_x(r) + V_c(r)\right]\Phi_i(r) = \varepsilon_i\Phi_i(r) \qquad (16)$$

(Eq.16) is the Kohn-Sham description of electrons Coulomb interactions and is considered the backbone of first-principles materials modeling.

4. Projection of density functional concept on Khon-Sham equations

Since the foundation of Khon-Sham equations in 1965, many developed approximations have been attempted to specify $V_x(r)$ and $V_c\ (r)$. Form the Hohenberg-Kohn theorem (1964) which states that the ground-state electron density $n(r)$ of a quantum system with N electrons is uniquely determined by the electron density $n(r)$ [5]. More precisely, if E is the lowest possible energy (energy of the ground state) of the system, then E expression is a functional of the electron density only [1]:

$$E = F[n(r)] = \int dr\, n(r)V_n(r) - \sum_i \int dr\Phi_i^*(r)\frac{\nabla^2}{2}\Phi_i(r) + \frac{1}{2}\int\int dr\, dr'\, \frac{n(r)n(r')}{|r-r'|} + E_{xc}[n(r)] \qquad (17)$$

In (eq.17), the only unknown terms are the exchange-correlation energy $E_{xc}[n(r)]$ and nature of the electron density nature $n(r)$. Unfortunately, Hohenberg-Kohn variational principle [1] which demonstrates the existence of a ground state density,n_0 for which the total energy $E = F[n(r)]$ (eq.17) is minimized such as:

$$\left.\frac{\delta F[n]}{\delta n}\right| = 0 \qquad (18)$$

Knowing the electron density $n(r)$ nature, now the Khon-Sham equations are [1]:

$$\left[-\frac{\nabla^2}{2} + V_n(r) + V_H(r) + V_{xc}(r)\right]\Phi_i(r) = \varepsilon_i\Phi_i(r) \qquad (19)$$

Where the exchange correlation potential is $V_{xc}(r) = \frac{\delta E_{xc}[n(r)]}{\delta n}\Big|$ (20)

(eqs.19,20) indicate that the functional $E_{xc}[n]$ is a sufficient condition to obtain the exact ground-state energy and electron density.

5. The exchange-correlation energy in DFT

In order to solve the Kohn-Sham equations, among many proposed, approximate functionals of $E_{xc}[n]$, two main concepts of exchange-correlation energy functionals are used in DFT which are the local density approximation (LDA) and the generalized gradient approximation (GGA)

5.1.Local density approximation (LDA)

In the LDA, the exchange-correlation functional is simply described by the homogenous (uniform) electron gas model of density *n* [4]. In the electron gas model, the exchange E_X energy and the correlation energy E_C (for no momentum effect) are exactly defined by (eqs 21,22) [1]:

$$E_X = -\frac{C}{(2\pi)^6} k_F^4 V \tag{21}$$

$$E_C = nV \begin{cases} 0.0311 ln r_s - 0.0.48 + 0.002 r_s ln r_s - 0.0116\, r_s & if\ r_s < 1 \\ \frac{-0.1423}{1+1.0529\sqrt{r_s}+03334\, r_s} & if\ r_s > 1 \end{cases} \tag{22}$$

where *C*, k_F and r_s are a numerical dimensionless constant, Fermi wave-vector and Wigner-Seitz radius respectively [1].

5.2.Generalized gradient approximation (GGA)

The basic concept in GGA approximation lies on describing the exchange-correlation energy not only by electronic density *n(r),* but with additional term which is the electronic density gradient (the first derivation). Mathematically, the electronic density is approximated as the first component in Taylor series development. Generally, the exchange-correlation energy in GGA approximation is defined by [3]:

$$E_{XC}[n(r), \nabla n(r)] = \int f(n(r), \nabla n(r)) dr \qquad (23)$$

There are many suggested approximations of density and its gradient dependency for the exchange-correlation energy, where some of them are cited in the next section. The approximations are mainly based on the separation of the exchange correlation by the formulae [3]:

$$E_{XC}[n(r), \nabla n(r)] = E_X[n(r), \nabla n(r)] + E_C[n(r), \nabla n(r)] \qquad (24)$$

6. CASTEP,v8.0 algorithms for solving DFT/Khon-Sham equations

6.1.The basis set

First of all, CASTEP is a DFT based software package where plane waves (PW) are the basis set to expand the Kohn-Sham orbitals [4]. In addition, Chadi-Cohen scheme, and Monkhorst-Pack scheme [7] are the most effective ones to generate *k* points in the reciprocal space when the energy of systems is calculated as an integral over these points.

6.2.Local exchange-correlation functionals (CA-PZ)

The only implemented LDA in CASTEP is the CA-PZ functional [7] that is based on on the empirical parameterization of the Ceperley and Alder (1980) data [6].

6.3.Gradient corrected exchange-correlation functionals

(PBE, PW91, RPBE, PBEsol, WC)

The Perdew, Burke and Ernzerhof (PBE) functional (1996) is the common GGA functional in CASTEP, which gives similar results with PW91(Perdew,1992) functional [7]. A modified nonlocal functional of the PBE was suggested by Hammer, Hansen and Norskov (1999) [7] named (revised) RPBE devoted to describe metallic surfaces [7]. One more time in 2008, Perdew has developed the PBEsol functional to model better the exchange component in solids [6]. Lastly, the plane wave WC functional, proposed by (Wu and Cohen, 2006) [7] allowed to improve structural and surface parameters energies.

6.4.Nonlocal exchange-correlation functionals

(HF-LDA, SX, SX-LDA, PBE0, B3LYP, HSE03, HSE06)

Nonlocal exchange-correlations are hybrid functionals that are constructed of screened, nonlocal and local density component of exchange and correlation energies described in LDA or GGA functionals. They are derived from the generalized Kohn-Sham algorithm (Seidl, 1996) [7]. These hybrid functionals consume much time and are used to improve the band gaps calculations in insulators and semiconductors [6].

In CASTEP calculations, it is recommended to use sX-LDA, PBE0, B3LYP and HSE06. sX-LDA has the screened exchange part and LDA correlation part. The PBE0 is considered as a PBE functional with a predefined amount of exact exchange. B3LYP functional is a combination of Hartree-Fock exchange with DFT exchange-correlation. HSE06 (Heyd-Scuseria-Ernzerhof) functional is based on a optimized screening for Coulomb potential [6].

6.5.Pseudopotentials

The concept of describing electrons in solids according to the valence electrons only is introduced by Phillips and Kleinman (1959), Cohen and Bergstresser (1966) by modeling the nuclear potentials with ionic pseudopotentials which are determined empirically [1]. This approximation resides in the negligible contributions of the core electrons to bonding compared to those of the valence electrons [6]. Moreover, the representation of all nuclei electrons of an atom with plane wave basis sets is computationally expensive.

Two main procedures available in CASTEP are the norm-conserving pseudo-potentials (NCP) and the ultra-soft pseudo-potentials (USP) [7]. For norm-conserving pseudo-potentials, (Hamann, Schlüter and Chiang, 1979, Bachelet, Hamann and Schlüter, 1982, Kleinman and Bylander, 1982) [1], the charge enclosed in the pseudo-potential region is the same as that enclosed by the same space in all electron calculation [1,4]. For ultra-soft pseudo-potentials (Vanderbilt, 1990) [7], a soft pseudo-potential is generated more accurately using charge augmentation functions [1]

are used to relax fluctuations that the previous pseudo-potentials suffered near atoms nuclei [4].

6.6.Relativistic effects

CASTEP includes scalar relativistic effects and also spin-orbital coupling (SOC), these considerations are important, particularly, in the core electrons of heavier elements but they have detrimental effect on the band gap calculation [6]. The scalar relativistic effects, higher order elements of the relativistic energy expansion are added to the kinetic energy operator while the spin-orbit coupling effect is arisen from the magnetic coupling between the different angular momentum degrees of freedom.

7. Calculation of OMHP electronic properties using DFT method

It is widely known that the GGA without considering SOC usually underestimates the band gap of halide perovskites [5,8,9] due to the self-correlation error of electrons and inherent lack of derivative discontinuity [8]. In the same time, the HSE06 without SOC overestimates band gap of halide perovskites [10,11]. Many advanced computational methods, such as PBE+SOC and HSE+SOC, attempt to improve the calculation accuracy in the band structure calculations. However, HSE+SOC calculation is much time consuming, which makes it avoidable in larger cells description.

In order to give more insights into the effect of the different DFT calculation methods on the band gap of OMHP, a comparative study of the band gap structures of $MAPbI_3$ at cubic, tetragonal and orthorhombic phases between standard GGA-PBE and HSE06 functionals has been made, as shown in Figure.15.

It has been found that GGA-PBE results are very consistent with the experimental ones compared to HSE06 in calculating the band gaps of $MAPbI_3$ structures [12]. In another work, an investigation of the electronic band gap, band structure, total and partial densities of states of $FABX_3$ (B=Sn, Ge; X=I,Br, Cl) perovskites using CASTEP code has approved that GGA-PBE results agree with the experimental ones while PBE+SOC has exhibited underestimated values [10].

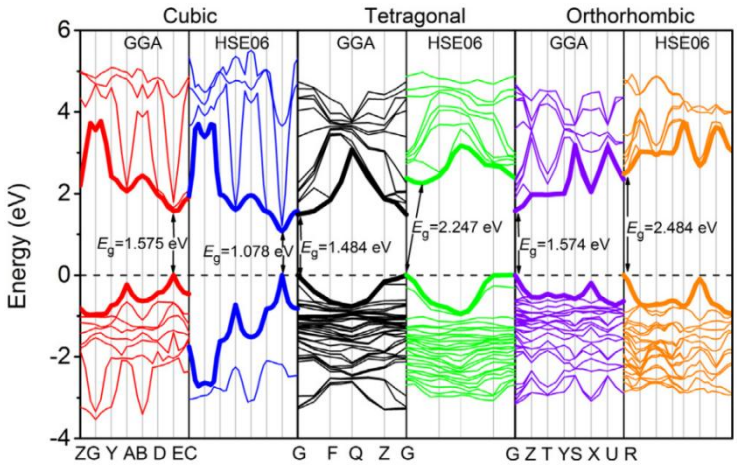

Figure.15. Comparison of band gap of $MAPbI_3$ using PBE-GG and HSE06 functionals [12].

In astonishing study, 24 exchange-correlation functionals with and without SOC have been examined to calculate the band gaps of ($MAPbI_3$) and ($FAPbI_3$) cubic perovskites, ranging from three LDA functional (PWC, VWN, CA_PZ), ten GGA functional (BP, PW91, BLYP, BOP, VWN-BP, PBE, RPBE, PBESOL, HCTH, WC), seven MGGA M06-L, M11-L, MS0, MS1, MS2, TPSS, revTPSS) and four hybrids (HF-LDA, sX, sX-LDA, HSE06) [13].

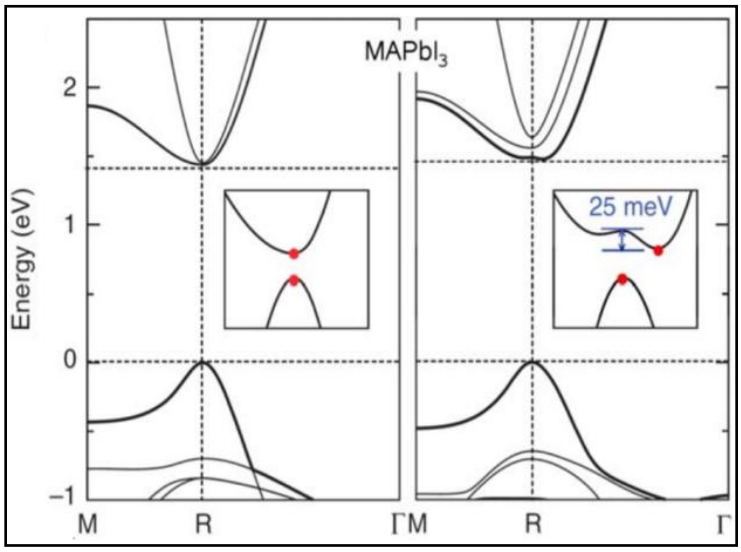

Figure.16. Energy band gap of cubic $MAPbI_3$ around R point without (left) and with (right) SOC [14].

In that study, it has been concluded that PBE and RPBE exhibit a good compromise between the accuracy of the obtained band gap and the computational cost. In addition, a sharp drop in the band gaps (~1 eV) is associated using SOC effect. The effect of SOC effect is considered also at the qualitative level. For instance, it has been found that SOC yield in indirect band gap for cubic $MAPI_3$ as shown in Figure.16[14].

8. Conclusion

To begin with, the DFT is the projection of electron of density *n(r)* in solving iteratively Khon-Sham equations which are implicitly the transformations of single-particle Shrödinger equation under clamped nuclei, independent electronic, mean field and quantum mechanics approximations.

Furthermore the core of DFT is based on the exchange-correlation functionals where many of them are proposed to predict accurate electronic properties, range from the simple LDA, GGA and hybrid functionals. In addition, pseudopotentials approximation in DFT allows reducing the computational load.

The use of DFT calculations is the fittest choice of many researchers to describe and examine the electronic properties of oregano-metallic halide perovskites, particularly, the PBE and RPBE functional due to their compromise between the accuracy of the obtained band gap and the computational cost.

9. References

[1].F. Giustino Materials Modeling using Density Functional Theory.2014.Oxford university press.

[2].T. Wolfram and S. ELL ˙Ialtio ˘Glu. Electronic and Optical Properties of d-band Perovskites.2006. Cambridge university press.

[3].K. HADDADI. Etude des propriétés structurales, élastiques et électroniques des composés antiperovskites de type $XNCa_3$.2013.These de doctorat en science. Universite de Setif.

[4].J Kitchin. Modeling materials using density functional theory.2012. GNU Free Documentation License.

[5].P. Beltracchi. A first-principles study of hybrid organic-inorganic perovskites for photovoltaic applications.2015.Thesis .University of Colorado.

[6].S.Cottenier. Density Functional Theory and the Family of (L)APW-methods: a step-by-step introduction.2013.

[7].BIOVIA. Castep guide materials studio v8.0. 2014. Dassaut systemes.

[8].J. Shi and S. Yun. First-Principles DFT Calculations for Perovskite Solar Cells.2018. Wiley.

[9].Z.W. Xu, C.R. Zhang, Y.Z. Wu, J.J. Gong , W. Wang , Z.J. Liu ,H. S. Chen. Density functional theory study on the electronic structures and related properties of Ag-doped $CH_3NH_3PbI_3$ perovskite. 2019. Results in Physics. Elsevier.

[10].Md Roknuzzaman, J. A. Alarco, H. Wang, A. Du, T. Tesfamichael, K. (Ken) Ostrikov. Ab initio atomistic insights into lead-free formamidinium based hybrid perovskites for photovoltaics and optoelectronics.2019. Computational Materials Science. Elsevier.

[11].Y.Wang, T. Gould, J.F. Dobson, H.Zhang, H Yang, X. Yaob and H.Zhao. Density functional theory analysis of structural and electronic properties of orthorhombic perovskite $CH_3NH_3PbI_3$.2014. Phys. Chem. Chem. Phys. RSC.

[12].M.Zhong, W. Zengb, H. Tang, L.X. Wang, F.S Liu, B.Tang,Q. J. Liu. Band structures, effective masses and exciton binding energies of perovskite polymorphs of $CH_3NH_3PbI_3$.2019. Solar Energy. Elsevier.

[13].N. Hernández-Haro, J. Ortega-Castro,Y. B. Martynov, R. G. Nazmitdinov, A. Frontera. DFT prediction of band gap in organic-inorganic metal halide perovskites: an exchange-correlation functional benchmark study.2018. Chemical physics. Elsevier.

[14].C.J Yu. Advances in modelling and simulation of halide perovskites for solar cell applications. 2018. JPhys Energy.IOP Publishing.

CHAPTER 3

Optimized Opto-electronic and Mechanical Properties of Orthorhombic ($MAPbX_3$) (X=I,Br,Cl) for Photovoltaic Applications

1. Introduction

Emergence of Organometallic halide perovskite (OMHP) in photovoltaic applications is due to their special absorptivity. OMHP absorbers are thus widely considered to enhance thin film PV cells of the 3rd generation [1,2]. They are among the best materials with high power conversion efficiency (PCE). In dye-sensitized solar cells [3], OMHPs have been used in devices with high PCE values [4,5] with high reported values more than 22% [6]. Therefore, OMHP systems have the prospect to reach commercial PV applications [7]. In addition to all such features, OMHP devices can be prepared by simple methods [8]. Therefore, OMHP based photovoltaic devices have a prosperous future, and need more study aiming at enhancing their conversion efficiencies.

In this chapter, the core of the thesis on (OMHP) is given. The obtained results present the description, optimization and comparison of a group of methylamunium lead halides ($MAPbX_3$) where (X=I, Br and Cl) at their orthorhombic phase. The description of ($MABX_3$) perovskites is determined by the calculation of lattice parameters and elastic constants, thus it provides insights into the crystallinity and morphology of the group of ($MABX_3$) perovskites. The optimization and comparison of the opto-electronic and mechanical properties is studied through the calculation of the energy band gap, density of states, absorption coefficients, dielectric constants and refractive index of ($MABX_3$) perovskites in such exposition to examine and identify the appropriate solar sell absorber. Ideally, a best absorber should be thermodynamically and permanently stable, non toxic, and has high absorption and charge transport properties.

In this work, the determination and comparison of the opto-electronic and mechanical properties of the sub group ($MAPbX_3$) perovskites in which the isovalent substitution of halide atoms is performed (X=I, Br and Cl).

Methylamunium lead halides ($MAPbX_3$) (X=I, Br and Cl) form a sub-class of perovskites. They are characterized by excellent opto-electronic features such as high absorption coefficients, tunable energy band gaps in the visible range, long range electron-hole transport lengths, and high carrier mobility [2,8,9]. Such features make these compounds good candidates for solar cells with high performance.

Iodine (I) based hybrid perovskites have been extensively studied for high PCE purposes. $MAPbX_3$ where (X=I, Br and Cl) features can be simply monitored by changing the halide ions from one to another [10]. By knowing $MAPbX_3$ parameters, such as shape and band structure, which relate to the effective masses of charge carriers and dielectric constants, the physics of devices can be understood, and techniques to develop their PV devices can be invented [9].

Generally, perovskites are represented by the general formula ABX_3, where A is an inorganic or organic cation, like $CH_3NH_3^+$(MA),$CH_5N_2^+$:FA,·...), B is a metal cation, like (Pb^{2+},Sn^{2+},...) , and X is a halide anion (I^-, Br^-,Cl^-, F^-). This study is focused basically on orthorhombic $MAPbX_3$ (X=I^-, $Br^-$and Cl^-) fundamental properties. Analytically, the formability and stability of orthorhombic $MAPbX_3$ (X=I^-, $Br^-$and Cl^-) are assisted by satisfying the octahedral factor μ and the tolerance factor t. The $MAPbX_3$ crystal structure is described in literature. So, the crystallography of $MAPbX_3$ is an arrangement of inorganic framework. A metal ion $Pb^{2+}$with six neighbouring halide ions I, Br, or Cl share $[PbI_6]^{4-}$, $[PbBr_6]^{4-}$or $[PbCl_6]^{4-}$ octahedra respectively. The MA cations are located at the centers of the $[PbI_6]^{4-}$ octahedra. Furthermore, each organic cation is coordinated by twelve halide anions as shown in Figure.17 [11].

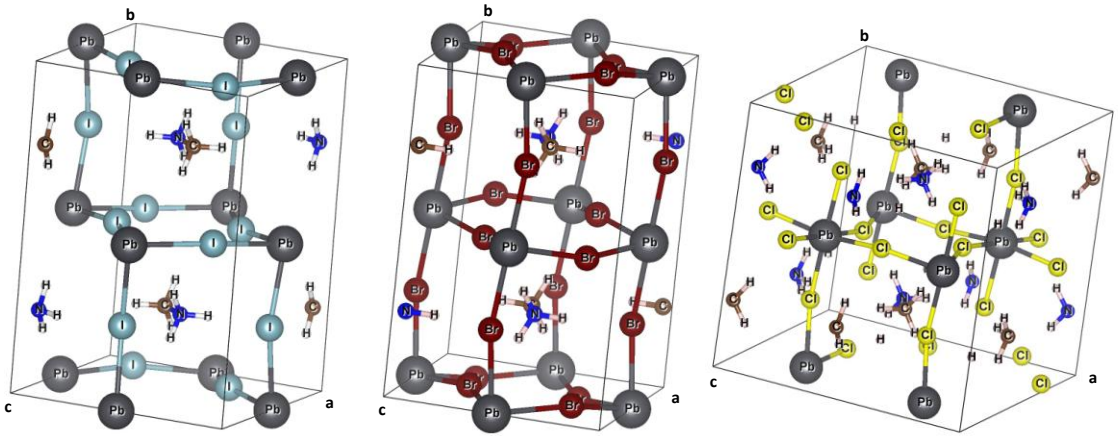

(a) (b) (c)

Figure.17. Orthorhombic crystal structures for: (a) $MAPbI_3$ (b) $MAPbBr_3$ and (c) $MAPbCl_3$.

X-ray diffraction patterns show that $MAPbX_3$ (X=I, Br and Cl), depending on temperature, may have different phases and symmetries. As temperature increases, the structures vary from low temperature orthorhombic to tetragonal, and then to high temperature cubic perovskite structures [5,12]. Literature also shows that when temperature increases, the symmetry of the perovskite increases too [13]. $MAPbX_3$ (X=I, Br and Cl) is formed at low temperature gradually in an orthorhombic structure γ phase (pnma space group) as presented in Figure 17. For instance, such structures occur for $MAPbCl_3$ at <172.9 K, for $MAPbBr_3$ at <144.5 K and for $MAPbI_3$ at <162.2 K) [14].

This work aims to quantitatively and qualitatively describe various intrinsic properties of $MAPbX_3$ (X=I, Br and Cl) as absorbent materials. Quantitative description involves ab-initio DFT based calculation of optimized properties , for orthorhombic structures of $MAPbX_3$ (X=I, Br and Cl): such as their electronic band gap structures, density of states, dielectric constant and refraction index as well as their mechanical properties. Qualitative description involves comparisons with other earlier studies. Finding optimal properties of $MAPbX_3$ that yield solar cells with higher conversion efficiency and comparing such findings with earlier experimental studies is one main goal of this work. Such comparison has not been made earlier to our knowledge.

2. Computational methods

DFT theory based calculation is useful in perovskite characterization. In this study, all calculation results: bulk geometry optimization, electronic, optical and mechanical properties are acquired using-plane wave basis- DFT method implemented in the Cambridge Sequential Total Energy Package (CASTEP, v 8.0) code. Ultrasoft pseudopotentials were adopted to describe the electron-ion interaction. The procedure Perdew-Burke-Ernzerhof (PBE) [15] constructs the generalized gradient approximation (GGA) functional DFT to express the exchange-correlation energy.

Fast low energy scanning studies of $MAPbX_3$ (X=I, Br and Cl) structures were performed and cutoff kinetic energies were found to be 400 eV for ($MAPBI_3$), 450 eV for ($MAPbBr_3$), and 400 eV for ($MAPbCl_3$). After checking convergence criteria, the Monkhorst-Pack of k-point mesh grid were fixed at 7×5×7 for ($MAPbI_3$), 8×6×8 for

($MAPbBr_3$) and 7×7×7 for ($MAPbCl_3$) for sampling Brillouin zone. Energy tolerance of $5x10^{-7}$eV/atom was set to betterprobe the calculation. The electronic valence states of each atom are: MA: Pb:$5d^{10}$ $6s^2p^2$, I:$5s^2p^5$,Br:$4s^2p^5$,Cl:$3s^2p^5$,C: $2s^22p^2$, N: $2s^22p^2$,H:$1s^1$.

3. Result and discussion

3.1. Structural properties

Firstly, to study such $MAPbX_3$ (X=I, Br and Cl) crystal systems, the equilibrium lattice parameters are calculated using BFGS method for geometry optimization [16] implemented in CASTEP. It allows refining a 3D system to obtain more stable and relaxed structure. The obtained lattice parameters (a×b×c) and the volume V are summarized in Table.2. The table shows that calculated lattice parameters of $MAPbX_3$ (X=I, Br and Cl) by (DFT-GGA) method are consistent with the listed experimental values. The results thus add credibility to findings acquired in following sections.

Table.2.Calculated (DFT) and experimental lattice parameters values of $MAPbX_3$ (X=I, Br, Cl).

Compound	Calculated lattice parameters a,b,c (Å),V(Å^3)	Experimental value	References
$MAPbI_3$	a=8.848,b=12.928,c=9.136. V=1045.116.	a=8.861, b=12.62, c=8.581. V=959.5	[14].
$MAPbBr_3$	a=7.999,b=12.009,c=8.675. V=833.408.	a=7.979,b=11.845,c=8.58. V=811.1	[14,17]
$MAPbCl_3$	a=11.480,b=11.610,c=11.545. V=1538.828.	a=11.193, b=11.347, c=11.287. V=1432.5.	[18]

3.2.Elastic constants and mechanical stability

The stability of perovskites based solar cell can be affected by various factors which determine the cell degradation, stress and strain [19]. For example, the design, the fabrication and the industrial processing of OMHP solar cells may affect their mechanical properties [20]. Therefore, the anisotropy on the Young′s modulus and the elastic constants of $MAPbX_3$ (X= I, Br, Cl) are investigated in this work.

Table.3. Calculated elastic constants, Young′s modulus (E), bulk modulus (B) and shear modulus (G) of $MAPbX_3$ (X= I, Br, Cl).

Elastic constants (GPa)	$MAPbI_3$ (Calculated)	$MAPbI_3$ [20]	$MAPbBr_3$ (Calculated)	$MAPbBr_3$ [20]	$MAPbCl_3$ (Calculated)
c_{11}	65.85	27.8	26.44	41.4	48.80
c_{22}	29.99	20.5	40.21	33.1	54.20
c_{33}	34.01	24.8	27.32	49.9	52.36
c_{44}	3.81	3	7.12	17.5	14.39
c_{55}	18.86	9.8	11.62	13.9	17.73
c_{66}	0.61	6.3	5.20	5.7	14.76
c_{12}	0.66	11.7	10.97	19.5	3.68
c_{13}	16.49	17.4	14.27	28.7	6.21
c_{23}	9.79	20.2	12.67	14.7	3.42
Young′s modulus E_x,E_y ,E_z (GPa)	57.24 26.84 26.79	15	18.43 33.33 18.34	27.9	47.87 53.75 51.44
Bulk modulus B, (GPa)	19.33	18.1	18.68	26.9	20.21
Shear modulus G, (GPa)	6.94	3.6	8.05	9.5	18.4

Table.3 contains the values of calculated elastic constants and Young′s modulus E_x, E_y, E_z for $MAPbX_3$ (X= I, Br, Cl) compounds. After some mathematical operations, the stability criteria for the used $MAPbX_3$ (X= I, Br, Cl), with orthorhombic structure, are well satisfied:

$c_{11}+ c_{22}-2c_{12}>0$, $c_{11}+ c_{33}- 2c_{13}>0$, $c_{22}+ c_{33}-2 c_{23}>0$, $c_{11}+ c_{22+} c_{33}+ 2c_{12}+ 2c_{13}+ 2c_{23}>0$, $c_{11}>0$, $c_{22}>0$, $c_{33}>0$, $c_{44}>0$, $c_{55}>0$, $c_{66}>0$ in [20]. The obtained elastic constants are comparable to those reported [20] for both $MAPBX_3$ (X=I, Br). Moreover, Young′s modulus values of $MAPbX_3$ (X=I, Br and Cl), along x, y and z faces, show the anisotropic stiffness for these materials. $MAPbX_3$ (X=I, Br) systems exhibit a clear contrast stiffness $E_{x,I}$=57.24 GPa and $E_{y,I}$=26.24 GPa, $E_{x,Br}$=18.43 GPa and $E_{y,Br}$=33.33 GPa, $E_{x,Cl}$ =47.87 GPa and $E_{y,Cl}$=53.75 Gpa, as observed in the present work. Based on Young′s modulus results, the tendency $E_{y,Cl}>E_{y,Br}>E_{yI,}$ confirm an earlier literature [21].

3.3.Electronic properties

3.3.1.Electronic band structure

Since the $MAPbX_3$(X=I, Br and Cl) compounds are established at their stable state, their electronic state band gaps are computed and shown in Figure.18. The Figure presents the electronic band gap structures of $MAPbX_3$ (X=I, Br and Cl) along high symmetry path directions. The band values correspond to E_g=1.626, 2.207 and 2.748 eV for $MAPbX_3$ (X=I, Br and Cl), respectively. All $MAPbX_3$ (X=I, Br and Cl) systems show a semiconductor behavior with direct band gap at Γ point. $MAPbX_3$ (X=I, Br and Cl) band structures well depict that the band gap values are inversely proportional to their corresponding halogens atomic numbers ($_{53}$I, $_{35}$Br, $_{17}$Cl). The present calculated band gap are also consistent with those reported earlier [14,22,23] and in congruence with the experimental values [8].

The obtained materials are stable due their formation enthalpies which are Δ_fH=-1.25 eV, Δ_fH=-1.31 eV, Δ_fH=-2.73 eV for $MAPbI_3$, $MAPbBr_3$ and $MAPbCl_3$ respectively. The present results show that the total energy of $MAPbI_3$ (-12500.3816 eV), where it was (-12500.1 eV) [23]. When performing band gap energy calculation, the result for $MAPbI_3$ E_g=1.626 eV is slightly improved with respect to earlier one which showed $E_{gMAPbI3}$

=1.656 eV value [1]. Moreover, the energy band gap result for $MAPbCl_3$ $E_{gMAPbCl3}$ =2.748 eV is found when performing the calculation on the lattice of (a=11.480, b=11.610 and c=11.545 Å) parameters. These parameters were used after screening for literature data. For example, the lattice parameters (a=5.673, b=5.628 and c=11.182 Å) were cited in one earlier report for orthorhombic $MAPbCl_3$ [14]; while they were (a=11.193, b=11.347, c=11.287 Å) in another report [21]. The present study thus gives more accurate values with higher credibility for parameters to be used in future calculations.

Energy diagrams found in the present work show that gradual exchange of iodide with bromide, and then with chloride in OMHP tunes the band gap from 1.62 to 2.2 and to 2.7 eV, respectively. Such tuning, confirmed here opens scope for new OMHP applications, as described earlier [24].

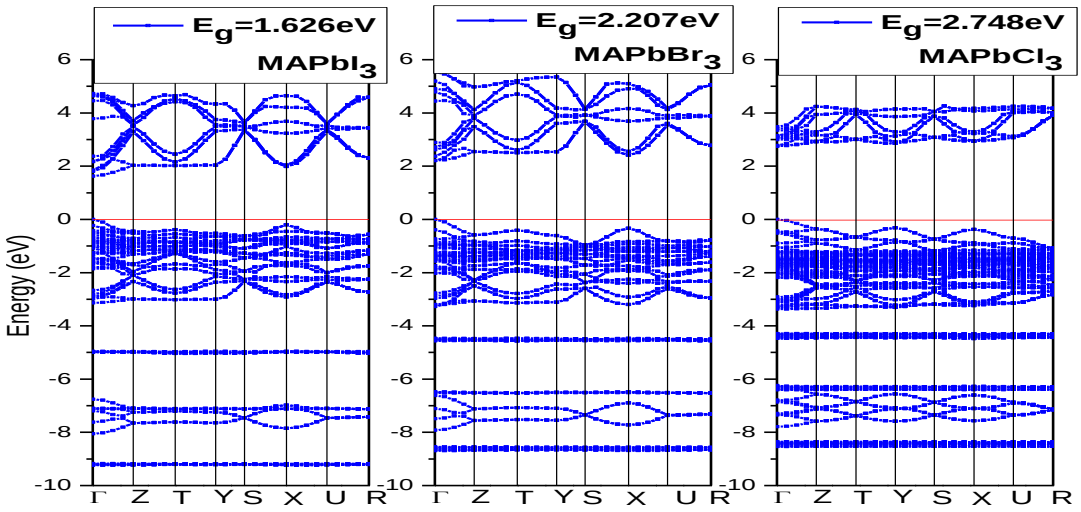

(a) (b) (c)

Figure.18. Electronic band gap structures of (a) $MAPbI_3$,(b) $MAPbBr_3$ and (c) $MAPbCl_3$.

3.3.2.Density of sates

The total (TDOS) and partial PDOS values are described in Figure.19. The figure shows that all $MAPbX_3$ (X=I, Br and Cl) compounds have the same energy distribution trend. The study shows that the MA-p state is located at -5 eV, far away from the Fermi level and has a small contribution on the band gap compared to other inorganic ions. The

results confirm the calculated partial density of states (PDOS) values reported earlier [25] that show a negligible density of states effect near the band edges. Moreover, MA^+ cation conserves the electronic equilibrium and stability of the structure. Recent literature shows that the interaction between MA^+ cation and $[PbX_3]^{4-}$ framework influences the bands composition and consequently the crystal geometry [26].

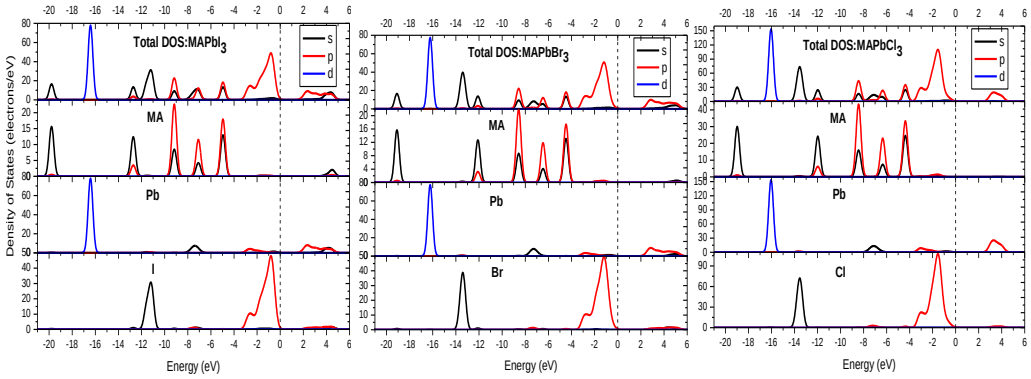

Figure.19. Total and partial density of states (TDOS and PDOS) of $MAPbX_3$ (X=I, Br and Cl).

From the figure, it has been noted that the conduction band minimum (CBM) is mainly dominated by Pb-6p orbitals and remains unchanged for all compounds. On the other hand the valence band maximum (VBM) is centered on halide ions p states (I-5p, Br-4p and Cl-3p) mixed with a small amount of Pb-6p and Pb-s states. Approximately, Pb cation and halide anions (I, Br, Cl) build the band gap energy edges [27]. No intense overlapping occurs between Pb-6p and (I-5p, Br-4p and Cl-3p) states which means weak Pb-X bonding [28].

Figure.19 also shows that the Pb-s and (I-p, Br-p and Cl-p states) are clearly visible at the same position from [-8 to -6 eV]. A hybrid state is clearly pointed between Pb-p and (I-p, Br-p and Cl-p) states over [-4 to 0 eV] energy band at the VBM and over [1.7 to 5 eV] energy band for the CBM as shown in Figure.19.

3.3.3 Electron charge density and Mullikan population analysis

To probe more intrinsic characteristic of $MAPbX_3$ (X=I, Br and Cl), further explanations on charge distribution are depicted in Figure.20.

The MA^+ cation shows very weak interaction and thus negligible overlap of electron orbitals between the organic component and inorganic Pb-X octahedrons. The behavior is present in all compounds. This feature is supported by the experimental contour plots of electron density for $MAPbBr_3$ reported earlier [29]. Finally, the interactions between Pb ions and X halide ions seem to be of ionic character bonding.

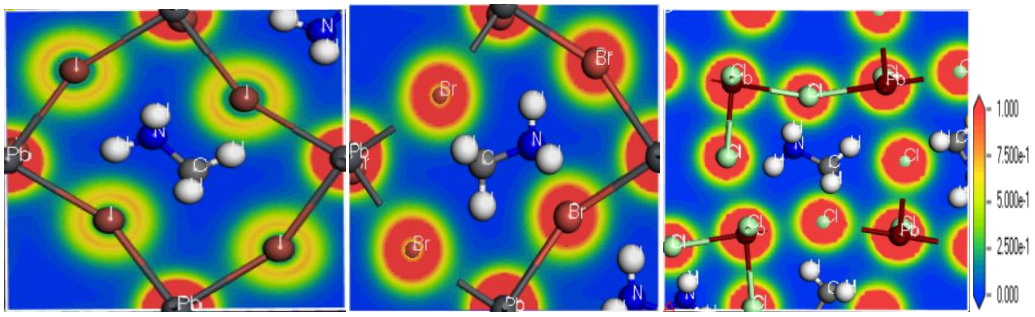

Figure.20. Electron charge density distribution of $MAPbX_3$ (X=I, Br, Cl) ranging (0 to 1e/A^3).

Once such OMHP structure is optimized, assigning partial charges to atoms can be very useful to give an interpretation for charge distribution in compounds. Population analysis methods provide valuable insights into the interactions that give rise to bonding, where Mulliken's analysis is the most common population analysis method.

Table.4.Calculated Mulliken atomic population values in Pb-X (I, Br and Cl) bonds.

Compound	ion	atomic Mullikan population	Ion number
$MAPbI_3$	I(1)	-0.47	8
	I(2)	-0.40	4
	Pb	+0.82	4
$MAPbBr_3$	Br(1)	-0.47	8
	Br(2)	-0.41	4
	Pb	+0.96	4
$MAPbCl_3$	Cl(1)	-0.57	12
	Cl(2)	-0.58	8
	Cl(3)	-0.59	4
	Pb	+1.11	8

Electronic charges for atomic Mullikan population of Pb-X bonding are summarized in Table.4. The table describes the partial charges of each atom in Pb-X bonding. The more electronegative Cl, Br and I atoms attract electron density away from the less electronegative Pb atoms leaving them positively charged.

3.4.Optical properties

The optical properties of orthorhombic $MAPbX_3$ (X=I, Br, Cl) can display anisotropy due to their asymmetry. This effect is included in the calculated results by taking the polarization direction of the electromagnetic field into account.

3.4.1. Absorption coefficient

The optical absorption coefficients of $MAPbX_3$ (X=I, Br, Cl) in different polarization directions are depicted in Figure.21. The figure shows the higher calculated absorption coefficient values ($\alpha=10^4$ to 10^5 cm^{-1}) for each OMHP in all polarization directions. From the figure, $MAPbI_3$, $MAPbBr_3$ and $MAPbCl_3$ present the same α trend and remain isotropic in all polarization directions over the visible energy band. $MAPbBr_3$ and $MAPbI_3$ exhibit a little anisotropy effect on the absorption peaks (4.5 and 3.5 eV) respectively in the near and middle ultraviolet [3.1-5.0 eV] energy bands with respect to polarization directions.

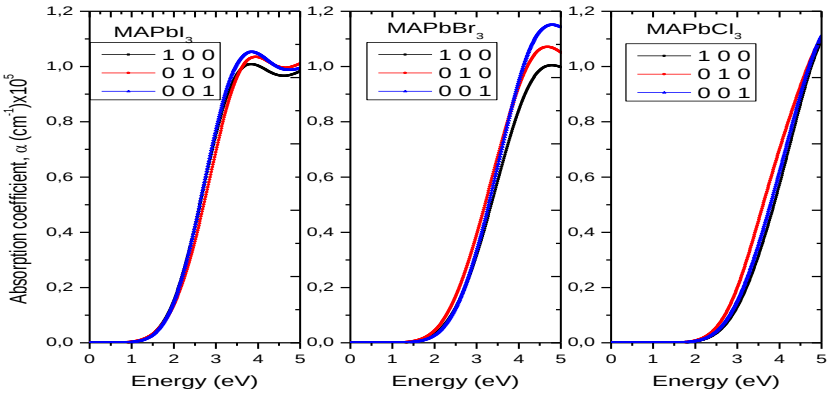

Figure.21. Optical absorption coefficients α of $MAPbX_3$ (X=I, Br, Cl) in different polarization directions.

To get more insight into the absorption coefficient of $MAPbX_3$ (X=I, Br, Cl), a comparative presentation is allowed in Figure.22. The figure shows that $MAPbI_3$ exhibits

broad and high light absorbance ($\alpha=10^4$-10^5 cm^{-1}) over the visible spectrum [1.65-3.26 eV: 380-750 nm]. Therefore, $MAPbI_3$ can be recommended in thin film absorber solar cells, as described earlier [30]. This absorption coefficient value is greater than those observed in conventional PV inorganic p-n junction materials such as $CuInGaSe_2$, CdTe and GaAs [14]. Figure.22 also shows that when halogen atomic size decreases (I, Br, Cl), light absorption decreases, accompanied by lowering of relative number of absorbed photons over the visible spectrum.

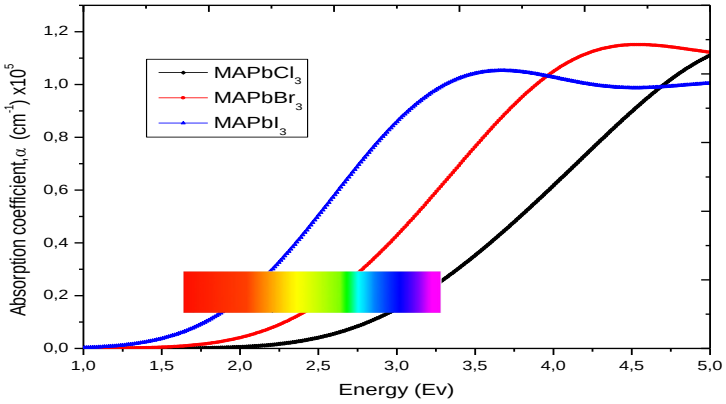

Figure.22. Comparison of optical absorption coefficient α for $MAPbX_3$(X=I, Br, Cl) at (0 0 1) polarization direction.

3.4.2.Dielectric constant

The dielectric constant or relative permittivity is a property that describes the ability of a medium to store an electric field during dipole polarization.

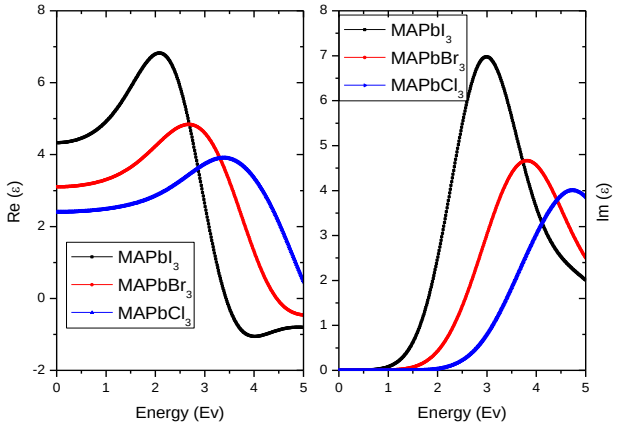

Figure.23. Re(ε) and Im(ε) of $MAPbX_3$ (X=I, Br, Cl) at (0 0 1) polarization direction.

The dielectric constant is expressed as: $\varepsilon = \varepsilon' - i\varepsilon''$, where the real part ε′ represents the charge storage ability and the imaginary part ε″ represents the energy loss. Only electronic polarization governs the dielectric process at optical (ultrahigh) frequencies. Figure.23 shows that $MAPbI_3$ has ε'_{opt}= 7, in congruence with literature [26,31]. It can thus be concluded that: when halogens atomic size decreases (I-Br-Cl), the electric field storage ability decreases but accompanied with a minimum energy loss (Figure.23).

3.4.3. Refractive index

The refractive index values for $MAPbX_3$ (X=I, Br, Cl) in different polarization directions are shown in Figure.24. $MAPbI_3$, $MAPbBr_3$ or $MAPbCl_3$ behaves in the same way when interacting with the incident electromagnetic field but a sensible anisotropy is present when each of these materials responds to such specific polarization.

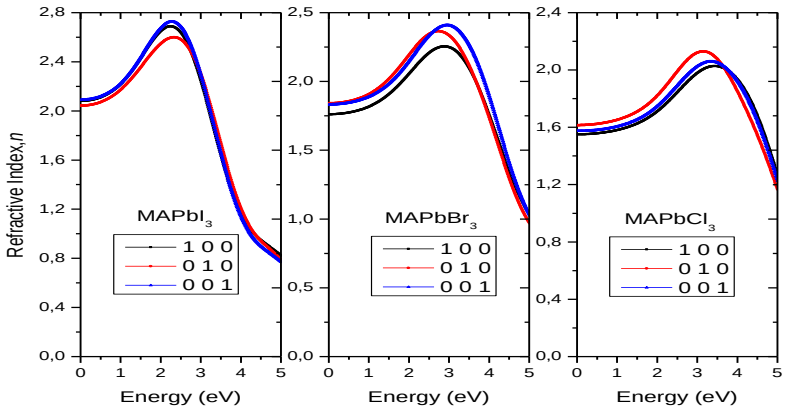

Figure.24. Refractive index *n* of $MAPbX_3$ (X=I, Br, Cl) in different polarization directions.

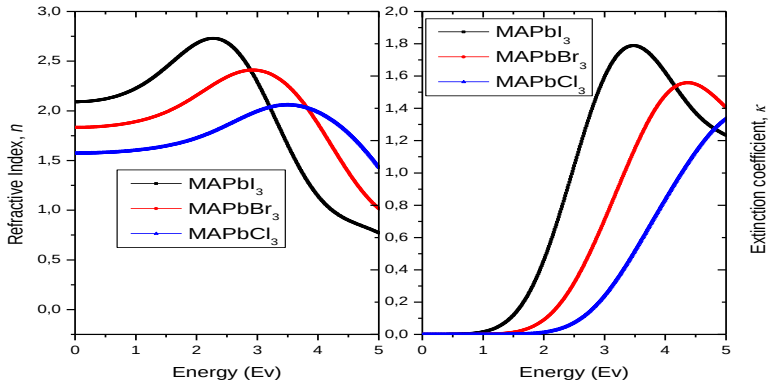

Figure.25. Calculated refractive index and extinction coefficients of $MAPbX_3$ (X=I, Br, Cl) at (001) polarization direction.

For comparison purposes, Figure.25 shows the refraction index values for $MAPbX_3$ (X=I, Br, Cl) at (001) polarization direction. The values vary as $n_{MAPbI3} > n_{MAPbBr3} > n_{MAPbCl3}$ along short wavelengths. The calculated values are comparablewith literature [32] for $MAPbX_3$ (X=I, Br, Cl) in their pseudo cubic phase, in term of the behaviour and effect of the anisotropy on the refractive index and extinction coefficient on $MAPbX_3$ (X=I, Br, Cl). It should be kept in mind that the present results specifically describe orthorhombic $MAPbX_3$ (X=I, Br, Cl) materials.

4. Conclusion

$MAPbX_3$ (X=I, Br, Cl) perovskites at their orthorhombic phase are basically described, in the present work, using DFT-GGA-PBE method implemented in CASTEP. These sub families of perovskites are absorber materials, so their optoelectronic and mechanical properties are calculated.

Firstly, for $MAPbX_3$ (X=I, Br, Cl) group, the calculated elastic constant values agree with other earlier literature. Furthermore, the anisotropy affects the stiffness of each compound along x,y, z orientations. $MAPbI_3$ is the stiffest material with E_x=57.24 GPa and the trend; $E_{y,Cl}$=53.75 GPa>$E_{y,Br}$=33.33 GPa>$E_{y,I}$=26.84 GPa is observed.

The results also show that the energy band gap can be tuned (from E_g=1.62 to 2. 2 to 2.74 eV) by varying halogens (from X=I to Br to Cl) respectively. Moreover, MA^+ has no significant effect on bonding charge distribution which is formed strongly by $Pb^{2+}$and (X=I, Br, Cl) atomic orbitals. The results show that $MAPbI_3$ has a wide band and strong absorption coefficient of $10^5 cm^{-1}$ in [1.65-3.26 eV: 380-750 nm] over the visible energy range. The calculated values state that anisotropy slightly affects the optical properties, particularly for $MAPbX_3$ (X=I, Br) in the near and mid ultraviolet range [3.1-5 eV]. Finally, the results show that when atomic number for the halide decreases, the dielectric constant and refractive index values decrease for $MAPbX_3$ (X=I, Br, Cl).

In conclusion, the obtained results give the idea that $MAAPbI_3$ is the recommended absorber and the more appropriate perovskite to use in photovoltaic solar cells.

5. References

[1]. Kanhere, P., Chakraborty, S., Rupp, C. J., Ahujabd, R.,Chen, Z. 2015. Substitution induced band structure shape tuning in hybrid perovskites (CH_3 $NH_3Pb_{1-x}Sn_xI_3$) forefficient solar cell applications.RSC Adv, 5, 1 07497.

[2]. Ndione, P. F., Li, Z., Zhu, K., 2016. Effects of alloying on optical properties of organic-inorganic lead halide perovskite thin films. Journal of Materials Chemistry C.

[3]. Zhou, Y., F. Wang, H.H. Fang, M. A. Loi, F.Y. Xie, N. Zhoa,Wong, C. P. 2016. Distribution of bromine in mixed iodide-bromide organolead perovskites and its impact on photovoltaic performance.Journal of Materials Chemistry A.

[4]. Hsiao, Y., Wu, T., Li, M., Liu, Q., Qin, W., Hu, B., 2015.Fundamental physics behind high efficiency organometal halide perovskite solar cells. J. Mater. Chem. A 3,15372.

[5]. Chen, J., Zhou, S., Jin, S.,Zhai, T.,2015. Crystal organometal halide perovskites with promising optoelectronic applications.Journal of Materials Chemistry C.

[6]. Qing, B., Wei, W., Zhou, Y.,Dong Y., 2018. Photoelectric performance and stability comparison of $MAPbI_3$ and $FAPbI_3$ perovskites solar cells. Solar Energy 174. 933-939.

[7]. Liu, D., Li, S., Bian, F.,Meng, X.,2018. First principles investigation on the electronic and mechanical properties of Cs-doped $CH_3NH_3PbI_3$. Materials.

[8]. Quarti, C., Mosconi, E.,Ball, J. M.,D'Innocenzo, V., Tao, C.,Pathak, S., Snaith, H. J.,Petrozza, A., Angelis, F. D., 2015.Structural and optical properties of methylammonium lead iodide across the tetragonal to cubic phase transition: implications for perovskite solar cells. Energy & Environmental Science.

[9]. Song, T. B., Chen, Q, Zhou, H., Jiang, C. , Wang, H. H., Yang, M., Liu, Y. S., You, J.,Yang, Y., 2015. Perovskite solar cells: film formation and properties.J. Mater. Chem. A.

[10]. Koliogiorgos, A., Baskoutas, S., Galanakis, I., 2017. Electronic and gap properties of lead-free perfect and mixed hybrid halide perovskites: An ab-initio study. Computational Materials Science 138. 92–98.

[11]. Chang, J.,Chen, H.,Yuan, H.,Wang, B.,Chen, X., 2017. The mixing effect of organic cations on structural,electronic and optical properties of $FA_xMA_{1-x}PbI_3$ perovskites.Physical Chemistry Chemical Physics.

[12]. Manser, J.S., Christians, J. A., Kamat, P. V., 2016.Intriguing optoelectronic properties of metal halide perovskites.Chem. Rev., 116, 12956 – 13008.

[13]. Chen, Q., Marco, N. D., Yang, Y. , Song, T.B., Chen, C.C.,Zhao, H. ,Hong, Z.,Zhou, H., Yang, Y., 2015. Under the potlight: The organic-inorganic hybrid halide perovskite for optoelectronic applications.Nano Today. 10, 355-396.

[14]. Liu, X., Zhao, W., Cui, H.,Xie, Y.,Wang, Y.,Xu, T.,Huang, F., 2012.Organic-inorganic halide perovskite based solar cells - Revolutionary progress in photovoltaics.Inorganic Chemistry Frontiers.

[15]. Perdew, J. P,Burke, K.,Ernzerhof, M., 1996. Generalized gradient approximation made simple,Phys.Rev. Lett,77,3865-3868.

[16]. Pfrommer,B.G., Louie, C. M., S.G. Cohen,M.L.,1997. Relaxationofcrystals withthequasi-Newton method,J.Comput. Phys,13,233-240.

[17]. Swainson, I.P.,Hammond, R.P., Soulliere, C., Knop, O., Massa,W.,2003. Phase transitions in the perovskite methylammonium lead bromide, $CH_3Nh_3PbBr_3$.Journal of Solid State Chemistry, 176. 97-104.

[18]. Chia, L., Swainsona, I, Cranswick, L., Herb, J.H.,Stephens, P., Knop, O., 2005. The ordered phase of methylammonium lead chloride $CH_3NH_3PbCl_3$. Journal of Solid State Chemistry, 178, 1376-1385.

[19]. Chen, A., Youssef, M., Zhang, C., 2018. Strain effect on the performance of amorphous silicon and perovskite solar cells. Solar Energy 163, 243-250.

[20]. Feng, J., 2014. Mechanical properties of hybrid organic-inorganic $CH_3NH_3BX_3$ (B = Sn, Pb; X = Br, I) perovskites for solar cell absorbers.APL materials 2, 081801.

[21]. Sun, S., Fang, Y.,Kieslich, G.,White, T. J.,Cheetham, A. K., 2015. Mechanical properties of organic-inorganic halide perovskites, $CH_3NH_3PbX_3$ (X=I, Br and Cl), by nano-indentation. Journal of Materials Chemistry A.

[22]. Cui, J., Yuan, H., Li, J., Xu, X., Shen, Y. ,Lin ,H.,Wang, M., 2015.Recent progress in efficient hybrid lead halide perovskite solar cells.Sci. Technol. Adv. Mater. 16, 036004.

[23]. Ji, D.,Xiao, X. J., Zhang, C. M.,Liy, X. L., Hu, M. Z., Yin., 2016.Regulatory band gap of vacancy at the B sites in $CH_3NH_3Pb_{1-x}I_3$ perovskite. Modern Physics Letters B,Vol. 30, No. 23.

[24]. Jacobsson, T. J, Correa-Baena, J. P., Pazoki, M., Saliba, M., Schenk, K., Grätzel, M., Hagfeldt, A., 2016. An exploration of the compositional space for mixed lead halogen perovskites for high efficiency solar cells. Energy & Environmental Science.

[25]. Ye, Y., Run, X., Tao, X. H., Feng, H., Fei, X., Jun, W. L., 2015.Nature of the band gap of halide perovskites ABX_3(A = CH_3NH_3,Cs; B= Sn, Pb; X = Cl, Br, I): First-principles calculations.Chin. Phys. B Vol. 24, No. 11. 116302.

[26]. Fan, Z.,Sun, K.,Wang, J.,2015. Perovskites for photovoltaics:acombined review of organic-inorganic halide perovskites and ferroelectric oxide perovskites. Journal of Materials Chemistry A.

[27]. Mladenovic, M.,Vukmirovic, N., 2018. Effects of thermal disorder on electronic structure of halide perovskites: Insights from MD Simulations.Physical Chemistry Chemical Physics.

[28]. Yin, W. J., Yang, J. H., Kang, J.,Yan, Y., Wei, S.H., 2014. Halide perovskite materials for solar cells: A theoretical review. Journal of Materials Chemistry A.

[29]. Jishi, R. A., Ta, O. B., Sharif, A. A., 2014. Modeling of lead halide perovskites for Photovoltaic applications. Cond. Mat.

[30]. Wolf, S. D., Holovsky, J., Moon, S.J., Löper, P., Niesen, B., Ledinsky, M., Haug, F.J., Yum, J.H., Ballif, C., 2014.Organometallic halide perovskites: Sharp optical absorption edge and its relation to photovoltaic performance. J. Phys. Chem. Lett, 5, 1035 – 1039.

[31]. Kenichiro Tanakaa, Takayuki Takahashia, Takuma Bana, Takashi Kondoa, Kazuhito Uchidab, Noboru Miura.2003. Comparative study on the excitons in lead-halide-based perovskite-type crystals CH3NH3PbBr3 CH3NH3PbI3. Solis State communications. 127.619-623.

[32]. Leguy, A. M. A., Azarhoosh, P., Alonso, M. I., Quiles, M. C.,Weber, O. J., Yao, J., Bryant, D., Weller, M. T., Nelson, J., Walsh , A., VSchilfgaarde, M.,Barnes, P.R. F., 2016. Experimental and theoretical optical properties of methylammonium lead halide perovskites. Nanoscale, 8, 6317.

CHAPTER 4

Effect of Metal (Ag and Cd) Substitution on $MAPbI_3$ Optoelectronic Properties for Photovoltaic Applications

1. Introduction

Organometallic halide perovskites (OMHP) are widely considered in photovoltaic applications partly due to their special absorptivity [1,2]. OMHP based solar cells, exhibit high power conversion efficiency (PCE) more than 22 % [3-6]. OMHP based solar cells may potentially have commercial application [7] due to their simple fabrication and efficient architecture [8]. With promising future, OMHP based PV devices deserve more study to optimize their conversion efficiencies.

Methylamunium lead iodide ($MAPbI_3$) has special optoelectronic features, such as high absorption coefficient, tunable band gap energy in the visible range, long range electron-hole transport lengths and high carrier mobility [2,8,9]. Such features highlight the importance of $MAPbI_3$ systems in high performance solar cells.

X-ray diffraction patterns show that $MAPbI_3$ involves various phases and symmetries at different temperatures. By increasing temperature, the crystal structure changes from orthorhombic to tetragonal, and then to high-temperature cubic perovskite [5,10]. Consequently, the perovskite symmetry increases as the temperature increases [11]. At low temperatures, precisely below 162.2 K, $MAPbI_3$ is gradually formed in the orthorhombic γ phase, with (pnma) space group [12], as described in Figure.26(a).

This study aims at investigating fundamental properties of the $MAPbI_3$ orthorhombic phase. Analytically, the formability and stability of orthorhombic $MAPbI_3$ are justified by satisfying the octahedral factor μ and the tolerance factor t defined by:

$$\mu = {r_{Pb}}/{r_I} \tag{25}$$

$$t = {(r_{MA} + r_I)}\Big/{\sqrt{2}(r_{Pb} + r_I)} \tag{26}$$

Where r_{MA}, r_{Pb} and r_I are the ionic radii ofmethyl ammonium MA^+, Pb^{2+} and I^- ions respectively.

As discussed above, the $MAPbI_3$ crystal structure is described earlier. So, the $MAPbI_3$ resembles inorganic framework crystal structures. A metal ion Pb^{2+} with six neighbouring

iodide I^- ions share a $[PbI_6]^{4-}$ octahedron. The methyl ammonium MA^+ cations are located between $[PbI_6]^{4-}$octahedra, where each organic cation is coordinated to twelve iodide ions, as shown in Figure.26(a) [13].

Despite the advantages of $MAPbI_3$, it suffers two shortcomings. Firstly it has low stability, which limits its commercial value. Secondly, it involves the hazardous Pb^{2+} ions which may lead to environmental problems in case of wide commercial application, keeping in mind the low perovskite stability. Therefore, further study is needed to stabilize the perovskite and/or lower the lead ion concentrations.

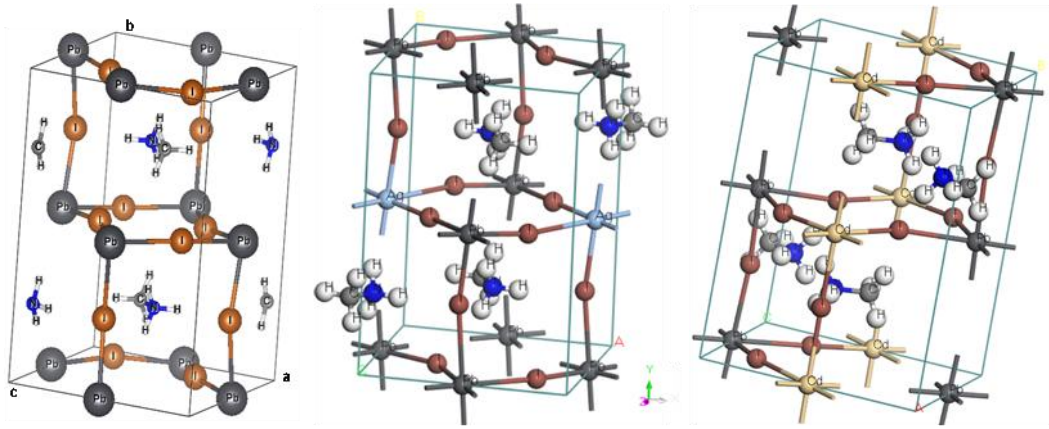

(a) (b) (c)

Figure.26. Proposed orthorhombic crystal structures of (a) $MAPbI_3$ (b) $MAAg_{0.17}Pb_{0.83}I_3$ and (c) $MACd_{0.5}Pb_{0.5}I_3$

Recently, the Pb^{2+}ions have been substituted with other metal cations, aiming at enhancing the properties of the $MAPbI_3$perovskite. Different metals are investigated for this purpose. Monovalent substitution, with ions such as those of Cu, Na, Ag and others, significantly affects the perovskite properties, and consequently the solar cell performance[14]. Mn^{2+}, Zn^{2+}, Sn^{2+}, Ge^{2+} , $Cd^{2+}$and others were examined as isovalent replacement for the toxic lead ion in $MAPbI_3$ perovskite on one hand, and to tune the material optoelectronic properties on the other hand [15].

In the present work, two ions (Ag^+ and Cd^{2+}) are chosen as partial substituent for lead ion to yield the orthorhombic $MAB_xPb_{1-x}I_3$ (B_x=$Ag_{0.17}$ or $Cd_{0.5}$) systems. The goal is many-fold. Using lower lead ion content should lower the environmental impact of the new systems. Investigating Ag^+ and Cd^{2+} ions by including effect of valence state ($4d^{10}$)

on the electronic interactions and the optical properties of the new systems, is another goal. Moreover, stability assessment of the new system is beneficial for environmental purposes.

Ag^{+} ion, which has not been widely described before as dopant in $MAPbI_3$, is chosen as substituent element because its ionic radius (1.15Å) is soundly close to that of Pb^{2+}(1.19 Å). Hopefully, the substitution may have minimal effect on the new system structural properties. A compromised control of the substituted concentration is of interest, between the Ag^{+} excess that leads to a metallic behavior of $MAAg_xPb_{1-x}I_3$ and the desirable tuned properties.

Cadmium ion (Cd^{2+}) has an ionic radius of 0.95 Å and is also toxic like Pb^{2+}. The Cd partial substitution into $MAPbI_3$ is still under investigation due to the inconsistent theoretical and experimental findings in literature [16]. Dependence of band gap value and orthorhombic phase stability with respect to the Cd substitution concentration needs further study.

Using ab-initio DFT calculations, the structural and the optoelectronic properties (including electronic band gap structure, density of states, dielectric constant and refraction index) are comparatively studied here for the orthorhombic $MAPbI_3$, and for the proposed systems $MAAg_{0.17}Pb_{0.83}I_3$ and $MACd_{0.5}Pb_{0.5}I_3$. Structures for these systems are summarized in Figure.26.(b-c).

2. Computational methods

DFT theory based calculation is useful for perovskite characterization. In this study, all calculation results: bulk geometry optimization, electronic and optical properties have been acquired using plane wave basis DFT method implemented in the Cambridge Sequential Total Energy Package (CASTEP, v 8.0) code. Using CASTEP, all perovskite structures are described and treated as periodic systems which can be achieved by creating a supercell containing the structure of interest [17]. The supercell is very expensive approach for calculating the properties of perovskite solutions. Ultrasoft pseudo-potentials have been adopted to describe the electron-ion interaction. The procedure Perdew-Burke-Ernzerhof (PBE) [18] constructs the generalized gradient

approximation (GGA) functional DFT to express the exchange-correlation energy. Furthermore, to compare the band gap results, the hybrid functional HSE06 [19], with norm-conserving pseudo-potentials [20], has also been used.

Fast low energy scanning calculations on $MAPbI_3$, $MAAg_{0.17}Pb_{0.83}I_3$ and $MACd_{0.5}Pb_{0.5}I_3$ structures have been performed and the cutoff kinetic energies have been found to be 400 eV for $MAPBI_3$, 400 eV for $MAAg_{0.17}Pb_{0.83}I_3$ and 550 eV for $MACd_{0.5}Pb_{0.5}I_3$. After checking convergence criteria, the Monkhorst-Pack of k-points mesh grids were fixed at 7×5×7 for $MAPbI_3$, and at 6×4×5 in both $MAAg_{0.17}Pb_{0.83}I_3$ and $MACd_{0.5}Pb_{0.5}I_3$ for Brillouin zone sampling. Energy tolerance of $5x10^{-7}$ eV/atom has been set to better probe the calculation. The electronic valence states of each atom are: Pb:$5d^{10}$ $6s^2p^2$, I:$5s^2p^5$,Ag: $4d^{10}$ $5s^1$, Cd:$4d^{10}$ $5s^2$, C: $2s^22p^2$, N: $2s^22p^2$,H:$1s^1$.

3. Results and discussion

3.1. Structural properties

Table.5. Calculated (DFT) and lattice parameter values for $MAPbI_3$, $MAAg_{0.17}Pb_{0.83}I_3$ and $MACd_{0.5}Pb_{0.5}I_3$

Compound	Calculated lattice parameters a,b,c (Å),V(Å^3),(α,β,γ)°	Literature experimental value (Ref)
$MAPbI_3$	a=8.848,b=12.928,c=9.136	a=8.861, b=12.62, c=8.581.
	α=β=γ=90°	α=β=γ=90° [12]
	V=1045.116.	[12]V=959.5
$MAAg_{0.17}Pb_{0.83}I_3$	a=8.466,b=12.78,c=9.141.	
	α=89.46°, β= 90.267°, γ=90.119°	
	V=989.	
$MACd_{0.5}Pb_{0.5}I_3$	a=8.568,b=12.729,c=9.23	
	α=89.978°, β=90.451°, γ=89.987°	
	V=1006.8	

To study the proposed crystal systems, the equilibrium lattice parameters have been calculated using the BFGS method for geometry optimization described in CASTEP [21]. This method allows refining a 3D system to obtain more stable and relaxed structure. Values for the lattice parameters: (a×b×c), (α,β,γ) and the volume V of $MAPbI_3$, $MAAg_{0.17}Pb_{0.83}I_3$ and $MACd_{0.5}Pb_{0.5}I_3$ are shown in Table.5.

Table.5 shows that the calculated lattice parameters of $MAPbI_3$ by (PBE-GGA) method are consistent with literature values [12]. Table.5 also shows that the volumes of $MAAg_{0.17}Pb_{0.83}I_3$ and $MACd_{0.5}Pb_{0.5}I_3$ are contracted along x and y directions compared to that of $MAPbI_3$. Moreover, the table shows that incorporating Ag or Cd ions into $MAPbI_3$ slightly distorts the orthorhombic symmetry to triclinic structures for $MAAg_{0.17}Pb_{0.83}I_3$ and $MACd_{0.5}Pb_{0.5}I_3$ (Figure.26.(b-c)). The structures can also be considered approximately orthorhombic as all observed triclinic system angles are close to 90˚

3.2. Electronic properties

3.2.1. Electronic band gap

Since the $MAB_xPb_{1-x}I_3$ (B_x=$Ag_{0.17}$ or $Cd_{0.5}$) systems are established in their stable states, their electronic band gaps are computed and shown in Figure.27. The comparison of the electronic band gap structures of $MAAg_{0.17}Pb_{0.83}I_3$ and $MACd_{0.5}Pb_{0.5}I_3$ along high symmetry path directions is presented in the figure.

Figure.27 (a) shows that the proposed partial substitutions cause significant tuning in the perovskite band gap. The band gap value found using PBE-GGA method is widened from E_g=1.626eV (for $MAPbI_3$) to 1.732 eV (for $MAAg_{0.17}Pb_{0.83}I_3$) and is narrowed to 0.753eV (for $MACd_{0.5}Pb_{0.5}I_3$). The calculated $MAPbI_3$ band gap value is in congruence with those reported earlier [8,12,21,22,29]. Such tuning, confirmed here opens a new scope for new OMHP applications, as described above [25].

The obtained materials are stable due their formation enthalpies which are Δ_fH=-1.25 eV, Δ_fH=-1.19 eV, Δ_fH=-1.28 eV for $MAPbI_3$, $MAAg_{0.17}Pb_{0.83}I_3$ and $MACd_{0.5}Pb_{0.5}I_3$ respectively The present results show that $MAPbI_3$ total energy (−12500.3816 eV) is comparable to the earlier reported value (−12500.1 eV)[23]. The obtained band gap value of $MAPbI_3$ (1.626 eV) is also consistent with earlier reported value 1.656 eV [23].

Figure.27(a) shows that contrary to the direct band gap for $MAPbI_3$, the $MAAg_{0.17}Pb_{0.83}I_3$ and $MACd_{0.5}Pb_{0.5}I_3$ systems have indirect band gaps for Γ to Q point and D to B point, respectively, where the electronic transition between the valence band (VB) and the conduction band (CB) edges is assisted by phonons [26]. The figure also shows that Ag^+ ion partial substitution shifts the Fermi level down towards the valence band. Such behavior was reported in earlier literature [14,25]. This explains why $MAAg_{0.17}Pb_{0.83}I_3$ behaves as a p-type semiconductor.

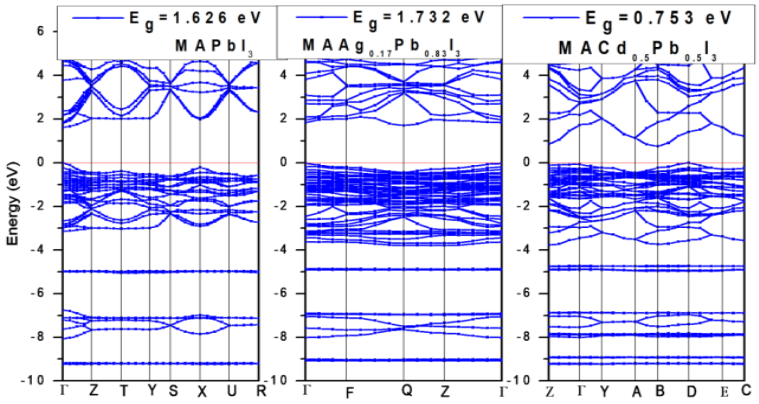

Figure.27. Electronic band gap structures of $MAPbI_3$, $MAAg_{17}Pb_{83}I_3$ and $MACd_{0.5}Pb_{0.5}I_3$; using (PBE-GGA).

The 50% Cd substitution into $MAPbI_3$ drastically narrows the band gap and the result (E_g=0.753 eV) seems to be anomalous. Therefore, the Tauc plot is useful to calculate the optical band gap for $MACd_{0.5}Pb_{0.5}I_3$ as shown in Figure.28. The quantity to show is $(\alpha E)^{1/r}$; where *r* is an exponent that expresses the nature of the transition). The band gap of $MACd_{0.5}Pb_{0.5}I_3$ is indirect which means that *r*=2.

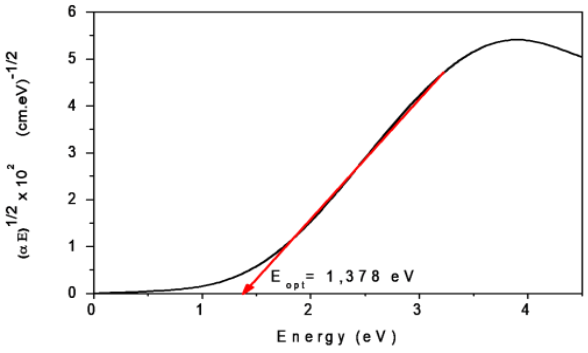

Figure.28. $MACd_{0.5}Pb_{0.5}I_3$ Tauc plot using PBE-GGA method

Figure.28 shows that the optical band gap obtained from Tauc plot E_{opt}=1.378 eV is incomparable with E_g=0.753 eV. It is nearly a half band gap reduction.

In addition to the PBE-GGA method, the HSE06 method has been used to calculate the electronic bad gap values for all three compounds. The results are presented in Figure.29.

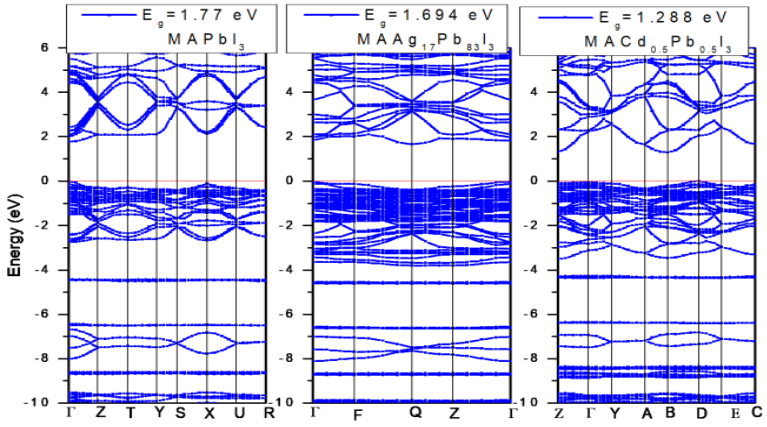

Figure.29. Electronic band gap structures of $MAPbI_3$, $MAAg_{17}Pb_{83}I_3$ and $MACd_{0.5}Pb_{0.5}I_3$; using (HSE06) method.

From Figures.(27,29), the obtained band gap results of $MAPbI_3$ and $MAAg_{17}Pb_{83}I_3$ using (PBE-GGA) and (HSE06) methods are comparable. While the PBE-GGA method shows that the band gap values of 1.626 eV (for $MAPbI_3$), 1.732 eV (for $MAAg_{0.17}Pb_{0.83}I_3$) and 0.753 eV (for $MACd_{0.5}Pb_{0.5}I_3$), the HSE06 method shows 1.770 eV (for $MAPbI_3$), 1.694 eV for ($MAAg_{0.17}Pb_{0.83}I_3$) and 1.288 eV (for $MACd_{0.5}Pb_{0.5}I_3$). For $MAPbI_3$ the band gap calculated by HSE06 is 8.85% wider than that calculated using PBE-GGA method. Inversely, for $MAAg_{0.17}Pb_{0.83}I_3$, the HSE06 calculated band is 2.2% narrower than the PBE-GGA value. For $MACd_{0.5}Pb_{0.5}I_3$, the HSE06 value is 71% wider than the PBE-GGA value. It should be noted that for the $MACd_{0.5}Pb_{0.5}I_3$ system, the HSE06 value is closer to the the optical band gap value, compared to the PBE-GGA result.

3.2.2. Density of states (DOS)

To investigate the optoelectronic properties of $MAPbI_3$ and $MAB_xPb_{1-x}I_3$ (B=$Ag_{0.17}$ or $Cd_{0.5}$), both total density of states (TDOS) and partial density of states (PDOS) are

calculated. Figure.30 shows that all studied compounds have the same energy distribution trend. The results show that the MA-p states are located at -5 eV, far away from the Fermi level and have small contribution to the band gap compared to other metallic atoms. The present results confirm the calculated partial density of states (PDOS) values reported earlier [27] that show the negligible MA^+ density of states effect near the band edges. Moreover, MA^+ cation conserves the electronic equilibrium and stability of the structure. It is reported that the interaction between MA^+ cation and $[PbI_3]^{4-}$ framework affects the orbital band compositions and consequently the crystal structure [28]. In all compounds, Pb-6p orbital is the major factor that controls the conduction band minima (CBM) [29]. On the other hand, the partial DOS results demonstrate that the valence band is mainly I-5p character from [-2- 0 eV]. Then, a mixture of I-5p with Ag-4d and low Cd-4d orbital density occurs in the band [-2 to -4 eV]. So the Ag^+/Cd^{2+} -4d states have no effect on the energy band gap formation. Approximately, the Pb cation and I anion determine the band gap energy edge positions. The results are in good agreement with literature [14,16].

Figure.30 shows that there is no intense overlapping between Ag-4d/Pb-6p and I-5p on one hand and between Cd-4d/Pb-6p and I-5p on the other hand. This means weak Ag/Cd/Pb-I bonding [29].

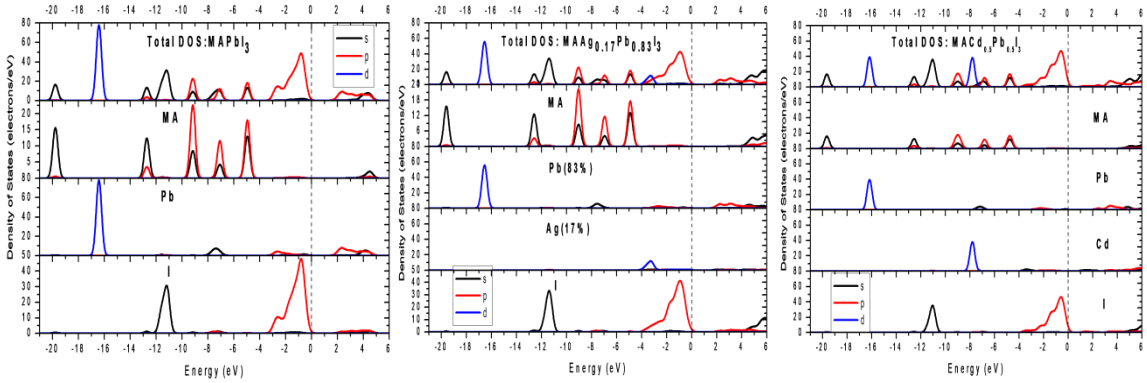

Figure.30.Values for total and partial density of states (TDOS and PDOS) for $MAPbI_3$, $MAAg_{0.17}Pb_{0.83}I_3$ and $MACd_{0.5}Pb_{0.5}I_3$

3.2.3. Electronic charge distribution

To further probe intrinsic characteristics of $MAPbI_3$ and $MAB_xPb_{1-x}I_3$ where ($B=Ag_{0.17}$ or $Cd_{0.5}$) electronic charge distributions are studied.

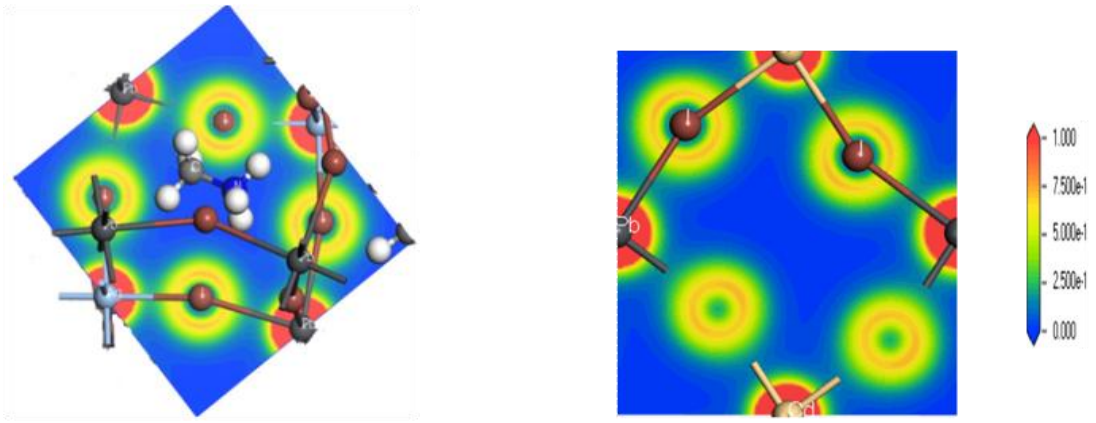

(a) (b)

Figure.31. Electron charge distribution for (a) $MAAg_{0.17}Pb_{0.83}I_3$ and (b) $MACd_{0.5}Pb_{0.5}I_3$ ranging (from 0 to 1e/Å^3)

Figure.31 shows that MA^+ cation exhibits very weak interactions with Ag, Cd, Pb or I ions. This means a negligible overlap between the orbitals of the organic component and inorganic Ag/Cd/Pb-I octahedra. The behavior is observed in all compounds, in congruence with literature [30]. Therefore, the interactions between Ag/Cd/Pb cations and I anion seem to have mostly electrostatic bond character.

3.2.4 Mullikan population analysis

Once the perovskite structure is optimized, assigning partial charges to atoms can be very useful to interpret quantitative partial charges in compounds. Population analysis methods provide valuable insights into interactions that give rise to bonding, where Mulliken's analysis is the most common population analysis method.

Electronic charges of atoms, based on Mullikan population of Ag/Cd/Pb-I bonding, are summarized in Table.6. The table shows the partial charges on each atom involved in Ag/Cd/Pb-I bonding. The iodine I atom, with higher electro-negativity, attracts electrons from Ag, Cd or Pb atoms leaving them positively charged.

Approximately, the I^- anion and Pb^{2+}cation preserve the same charges in two compounds. Table.6 also shows that Cd is the cation with the highest ability to share the electronic charge (+0.24 e) compared to Ag (+0.37 e) and Pb (+0.74 e) due to its lower electro-negativity (or higher electro-positivity). Electro-positivity describes the tendency

of an element to lose one or more electrons. Electropositive elements therefore tend to form positive ions. They donate electrons to other species and in doing so act as reducing agents. Metals are characterized by their electro-positivity, where alkali metals are known to behave as reducing agents.

Table.6.Calculated Mulliken atomic population charges in Ag/Cd/Pb-I bonding.

Compound	Ion	Mullikan atomic population	Ion number
$MAAg_{0.17}Pb_{0.83}I_3$	I(1)	-0.44	4
	I(2)	-0.22	2
	I(3)	-0.39	2
	I(4)	-0.19	2
	I(5)	-0.15	2
	Pb	+0.74	2
	Ag	+0.37	2
$MACd_{0.5}Pb_{0.5}I_3$	I(1)	-0.35	4
	I(2)	-0.33	4
	I(3)	-0.41	2
	I(4)	-0.14	2
	Pb	+0.74	2
	Cd	+0.24	2

3.2.5.Effective masses

In this study, the anistropic effective masses (m^*) of electrons (m^*_e) and holes (m^*_h) along principal directions are analytically obtained. This has been achieved by the parabolic approximation where the holes or electrons should exist at the top and bottom of the valence and conduction bands, respectively.

The effective mass model is defined by the equation:

$$m^* = \hbar^2 \left(\partial^2 E(k) / \partial k^2\right)^{-1} \quad (27)$$

Where *E(k)* is the energy dispersion Eigen state.

The effective mass results of holes and electrons are shown in Table.7. The PBE-GGA method is adopted to calculate effective masses for $MAPbI_3$ and $MAAg_{0.17}Pb_{0.83}I_3$ due to the band gap similarity compared to that obtained with HSE06 method. For $MACd_{0.5}Pb_{0.5}I_3$, the result is obtained using HSE06 energy dispersion. In Table.7, m_0 refers to electron mass.

Table.7 shows that all compounds are characterized by their low effective masses. The anisotropy also affects strongly the charge carrier (electron or hole) inside the perovskite.

Table.7. Anisotropic effective masses of $MAPbI_3$, $MAAg_{0.17}Pb_{0.83}I_3$$MACd_{0.5}Pb_{0.5}I_3$ using PBE-GGA and HSE06 methods.

Compound	Method	m_h^*/m_0	m_e^*/m_0
$MAPbI_3$	PBE-GGA	m^*_x =0.127	m^*_x =0.18
		m^*_y =0.06	m^*_y =0.084
		m^*_z =0.11	m^*_z =0.167
$MAAg_{0.17}Pb_{0.83}I_3$	PBE-GGA	m^*_x =0188	m^*_x =0.188
		m^*_y =0.39	m^*_y =0.082
		m^*_z=0.077	m^*_z=0.16
$MACd_{0.5}Pb_{0.5}I_3$	HSE06	m^*_x =0.095	m^*_x =0.1
		m^*_y =0.043	m^*_y =0.045
		m^*_z =0.082	m^*_z =0.085

3.3.Optical properties

The optical properties of orthorhombic $MAAg_{0.17}Pb_{0.83}I_3$, $MACd_{0.5}Pb_{0.5}I_3$ and $MAPbI_3$ should be anisotropic due to their asymmetry. The anisotropy is taken into account in the calculations by considering all different polarization directions of the electromagnetic field.

3.3.1.Absorption coefficient

Figure.32 shows the optical absorption coefficient values for $MAPbI_3$, $MAAg_{0.17}Pb_{0.83}I_3$ and $MACd_{0.5}Pb_{0.5}I_3$ along all polarization directions. As depicted in Figure.32, $MACd_{0.5}Pb_{0.5}I_3$ behaves differently when interacting with photons along x and z directions. The absorption peaks occur at 4.3 eV on one hand, and along y direction where the peak occurs at 3.5 eV on the other hand. Moreover, the absorption character along y direction resembles those of $MAPbI_3$ or $MAAg_{0.17}Pb_{0.83}I_3$.

To have in thoughts about the absorption through the partial Ag/Cd substitution, a comparative presentation is shown in Figure.33. The figure shows that $MAPbI_3$ exhibits broad and high light absorbance ($\alpha=10^4$ - 10^5 cm^{-1}) over the visible spectrum [1.65-3.26 eV: 750-380 nm], followed by $MAAg_{0.17}Pb_{0.83}I_3$ ($\alpha=10^4$ – $0.6x10^5$ cm^{-1}) and a smaller value for $MACd_{0.5}Pb_{0.5}I_3$ with ($\alpha=1.5x10^4$ – $0.4x10^5$ cm^{-1}). All in all, $MAPbI_3$ is still the appropriate absorber and can be recommended for thin film photovoltaic applications.

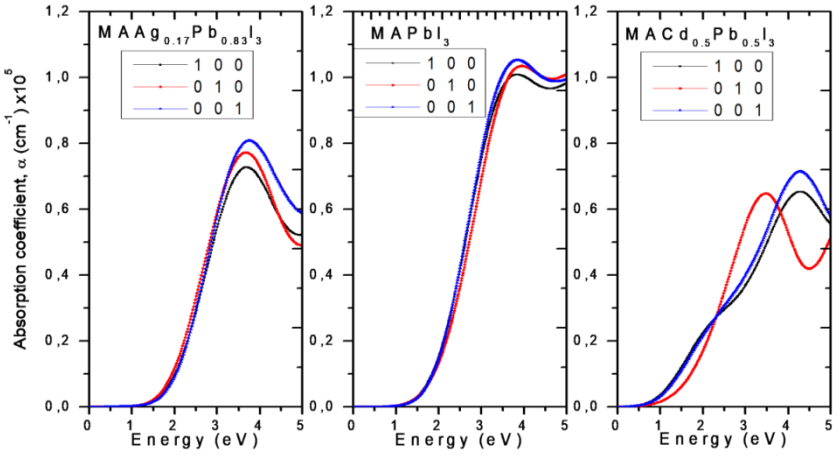

Figure.32. Optical absorption coefficient (α) values for $MAAg_{0.17}Pb_{0.83}I_3$, $MAPbI_3$ and $MACd_{0.5}Pb_{0.5}I_3$ in different polarization directions

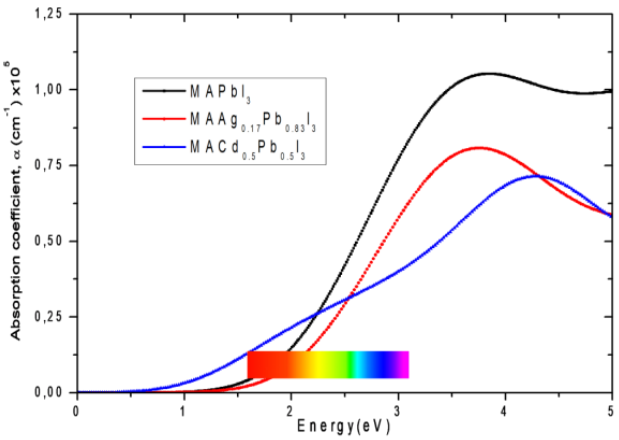

Figure.33. Comparison of optical absorption coefficient α values: for $MAAg_{0.17}Pb_{0.83}I_3$, $MAPbI_3$ and $MACd_{0.5}Pb_{0.5}I_3$ at (001) polarization direction using PBE method.

The figure shows the tendency:

$\alpha_{(MAPbI3)}=1.07x10^5 cm^{-1} > \alpha_{(MAAg0.17Pb0.83I3)}=0.8x10^5 cm^{-1} > \alpha_{(MACd0.5Pb0.5I3)} = 0.7x10^5\ cm^{-1}$. For this reason, $MAPbI_3$ is being considered as absorber in thin film solar cells [31]. Its absorption coefficient value is greater than those observed in conventional PV inorganic p-n junction materials such as $CuInGaSe_2$, CdTe and GaAs as described earlier [12].

Figure.33 also shows that $MAPbI_3$, and $MAAg_{0.17}Pb_{0.83}I_3$ exhibit the same α trend and remain isotropic in all polarization directions over the visible range [1.65-3.1 eV]. On the other hand, the anisotropy slightly affects the photon absorption in $MAAg_{0.17}Pb_{0.83}I_3$ in the near and mid ultraviolet range [3.1-5.0 eV] along all polarization directions. Highest absorption values are observed along z (001) direction for all compounds. Like $MAPbI_3$, the 17% Ag doped system exhibits highest absorption peak at the same energy (3.6 eV).

3.3.2.Dielectric constant

The real and imaginary parts of dielectric constant values for $MAAg_{0.17}Pb_{0.83}I_3$, $MAPbI_3$ and $MACd_{0.5}Pb_{0.5}I_3$ are illustrated in Figure.34(a-b). The figures show that all compounds have the same dielectric constant character and the same order of values in the visible spectrum. The $MAPbI_3$ has $\varepsilon'_{opt}=7$ and $\varepsilon''=7.5$, in congruence with literature [32]. Figures.34(a-b) show that doping $MAPbI_3$ with 17% Ag increases the dielectric real part ε' to 8.2 and lowers the dielectric imaginary part ε'' to 6.5.

Figure.34 shows that the $MACd_{0.5}Pb_{0.5}I_3$ has the exception where the anisotropy affects the dielectric behavior along x and z polarization directions. It is also noted that outside the visible band all compounds suffer the anisotropy effect. The high dielectric constant values are observed along z direction for both the real part and the imaginary part. Moreover, the Cd doped system maintains the same storage ability of $MAPbI_3$ (ε'_{opt}=7), whereas loss lowering occurs along the y direction (ε''=5.5) and along both the x and z directions (ε''=4).

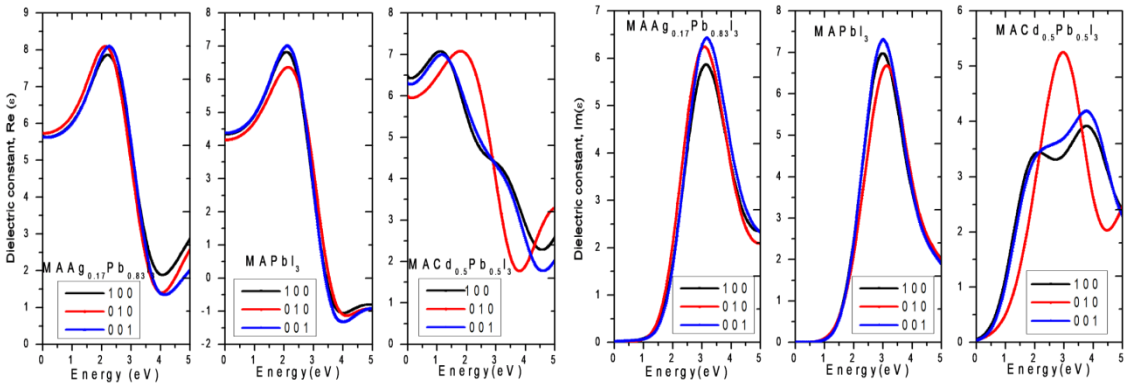

(a) (b)

Figure.34. Dielectric constant values (a) Re (ε) and (b) Im (ε) of $MAAg_{0.17}Pb_{0.83}I_3$, $MAPbI_3$ and $MACd_{0.5}Pb_{0.5}I_3$ along different polarization directions.

3.3.3.Refractive index

The refractive index (n) values in different polarization directions are shown in Figure.35(a), while the values of extinction coefficient are shown in Figure.35(b). The figures show that the $MAPbI_3$, $MAAg_{0.17}Pb_{0.83}I_3$ and $MACd_{0.5}Pb_{0.5}I_3$ behave similarly, with the exception for $MACd_{0.5}Pb_{0.5}I_3$ trend along x and z directions when interacting with the incident electromagnetic field. Moreover, the anisotropy influences each of these materials when responding to such specific polarization outside the visible spectrum.

For comparison purposes, Figure.35(a-b) show that the17% Ag doped system exhibits slightly increased reactive index n from 2.75 to 2.9 and decreased wave attenuation or extinction coefficient κ (Im (n)) from 1.8 to 1.4. Figure.35(a) shows that $n_{MAAg0.17Pb0.83I3} > n_{MAPbI3} > n_{MACd0.5Pb0.5I3,}$ with highest value n=2.9 observed for $MAAg_{0.17}Pb_{0.83}I_3$. The calculated values are comparable to literature [33], keeping in mind that the present

results specifically describe orthorhombic $MAPbI_3$ source. Incorporating 50% Cd into $MAPbI_3$ maintains the high refractive index peaks n=2.5 at 2.5 eV and 3.5 eV as in $MAPbI_3$, whereas the extinction coefficient κ is decreased from κ =1.8 (for $MAPbI_3$) to κ=1.2, 1.1 and 1.0 along y, z and x directions, respectively, for the doped system.

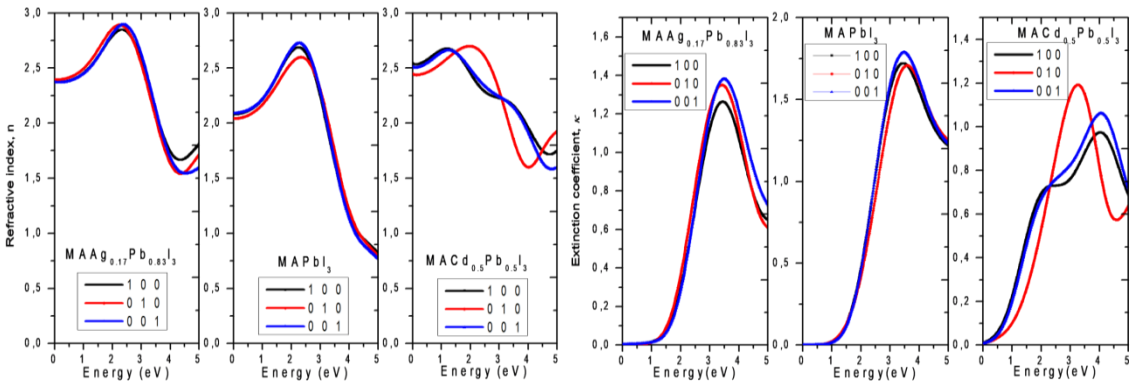

(a) (b)

Figure.35. Plots showing values of (a) Refractive index n and (b) Extinction coefficient κ for $MAAg_{0.17}Pb_{0.83}I_3$, $MAPbI_3$ and $MACd_{0.5}Pb_{0.5}I_3$ along different polarization directions.

Collectively, the study shows that the partial substitution of lead ion in $MAPbI_3$ may affect its optoelectronic properties without changing the crystal structure itself. The Ag^+ ion increases the refractive index value by increasing the real part and decreasing the imaginary part. The band gap value is widened which makes the doped system suitable for visible light absorption. For Cd^{2+} ion substituted system, the study came out with accurate optoelectronic property values for $MACd_{0.5}Pb_{0.5}I_3$ and $MACdI_3$ as reported earlier [15,23]. Investigating different substituent concentrations, to reach optimal compositions with the best optoelectronic properties for solar cell manufacturing based on $MAAB_xPb_{1-x}I_3$ is underway in these laboratories, together with stabilizing effect of elemental partial substitution. Optimized substituent concentration for various elements is also worth to investigate.

4. Conclusion

$MAPbI_3$ and $MAB_xPb_{1-x}I_3$ (B_x=$Ag_{0.17}$or $Cd_{0.5}$) perovskites at their orthorhombic phase are basically described here using DFT (PBE-GGA and HSE06) methods implemented in

CASTEP. These sub-families of perovskites are absorber materials, so their optoelectronic properties are calculated. For $MAAB_xPb_{1-x}I_3$ (B=0.17 Ag or 0.5 Cd) group, the substitution of 17% Ag and 50% Cd concentrations into $MAAPbI_3$ contracts the sizes of the new $MAAB_{0.17}Pb_{0.83}I_3$ and $MAAB_{0.5}Pb_{0.5}I_3$ perovskites.The results also show partial substitution with Ag and Cd tunes the energy band gap. The obtained band gaps using different methods are comparable for $MAPbI_3$, where E_g(PBE)=1.620 eV and E_g(HSE06)=1.77 eV and for $MAB_{0.17}Pb_{0.83}I_3$ where E_g(PBE)=1.732 eV and E_g(HSE06)=1.694 eV. The calculated values for $MACd_{0.5}Pb_{0.5}I_3$ are inconsistent, with E_g(PBE)=0.753 eV and E_g(HSE06)= 1.288, albeit the HSE06 result better fits with Tauc plot optical band gap valueE_{opt}=1.378 eV

Furthermore, the methyl ammonium (MA^+) has no significant effect on bonding charge distribution that strongly occurs by Pb-6p and I-5p atomic orbitals in all compounds. The results show that $MAPbI_3$ has the widest band and highest absorption coefficient (10^5 cm^{-1}) in the visible range [1.65-3.26 eV:350-780 nm] compared to the other perovskites. $MAPbI_3$ exhibits broad and high light absorbance ($\alpha=10^4$ - 10^5 cm^{-1}) over the visible spectrum [1.65-3.26 eV: 380-750 nm], followed by $MAAg_{0.17}Pb_{0.83}I_3$ ($\alpha=10^4 - 0.6x10^5$ cm^{-1}) and least for $MACd_{0.5}Pb_{0.5}I_3$ ($\alpha=1.5x10^4 - 0.4x10^5$ cm^{-1}).

Low anisotropic electron and hole effective masses characterize all compounds in the range of $0.043m_0$-$0.188m_0$. Moreover,the anisotropy slightly affects the optical properties for $MAAPbI_3$and $MAAB_{0.17}Pb_{0.83}I_3$ in the near and mid ultraviolet range [3.1-5.0 eV]. For $MAAB_{0.5}Pb_{0.5}I_3$, the anisotropy affects the optical properties such as the absorption coefficient α, the dielectric constant ε and the refractive index n along x and z directions.

Finally, the 17% Ag^+ substitution into the $MAAPbI_3$ increases the refractive index (Re(n)) and decreases the extinction coefficient (Im (n)=κ). The observed n values are 2.90, 2.75 and 2.00 for $MAAg_{0.17}Pb_{0.83}I_3$, $MAPbI_3$ and $MACd_{0.5}Pb_{0.5}I_3$, respectively, at 2.5 eV energy peak value. The observed κ values are 1.4, 1.8, and 1.2 for $MAAg_{0.17}Pb_{0.83}I_3$, $MAPbI_3$ and $MACd_{0.5}Pb_{0.5}I_3$, respectively, at 3.5 eV energy peak value.

5. References

[1].Kanhere, P., Chakraborty, S., Rupp, C. J., Ahujabd, R.,Chen, Z. 2015. Substitution induced band structure shape tuning in hybrid perovskites ($CH_3NH_3Pb_{1-x}Sn_xI_3$ for efficient solar cell applications. RSC Adv, 5, 1 07497.

[2].Ndione, P. F., Li, Z., Zhu, K, Effects of alloying on optical properties of organic-inorganic lead halide perovskite thin films. Journal of Materials Chemistry C. 4 (2016) 7775-7782.

[3].Zhou, Y., F. Wang, H.H. Fang, M. A. Loi, F.Y. Xie, N. Zhoa, Wong, C. P, Distribution of bromine in mixed iodide-bromide organo-lead perovskites and its impact on photovoltaic performance. Journal of Materials Chemistry A. 4 (2016) 16191-16197

[4].Hsiao, Y., Wu, T., Li, M., Liu, Q., Qin, W., Hu, B., 2015.Fundamental physics behind high efficiency organometal halide perovskite solar cells. J. Mater. Chem. A 3,15372.

[5].Chen, J., Zhou, S., Jin, S.,Zhai, T, Crystal organometal halide perovskites with promising optoelectronic applications. Journal of Materials Chemistry C. 4 (2015) 11-27.

[6].Qing, B., Wei, W., Zhou, Y.,Dong Y., 2018. Photoelectric performance and stability comparison of $MAPbI_3$ and $FAPbI_3$ perovskites solar cells. Solar Energy 174. 933-939.

[7].Liu, D., Li, S., Bian, F.,Meng, X.,. First principles investigation on the electronic and mechanical properties of Cs-doped $CH_3NH_3PbI_3$. Materials. 11 (2018) 1141.

[8].Quarti, C., Mosconi, E.,Ball, J. M.,D'Innocenzo, V., Tao, C.,Pathak, S., Snaith, H. J.,Petrozza, A., Angelis, F. D, Structural and optical properties of methylammonium lead iodide across the tetragonal to cubic phase transition: implications for perovskite solar cells. Energy & Environmental Science. 9 (2015) 155-163.

[9].Song, T. B., Chen, Q, Zhou, H., Jiang, C. , Wang, H. H., Yang, M., Liu, Y. S., You, J.,Yang, Y., Perovskite solar cells: film formation and properties.J. Mater. Chem. A. 3, (2015) 9032-9050.

[10].Manser, J.S., Christians, J. A., Kamat, P. V., 2016.Intriguing optoelectronic properties of metal halide perovskites.Chem. Rev., 116, 12956 – 13008.

[11].Chen, Q., Marco, N. D., Yang, Y. , Song, T.B., Chen, C.C.,Zhao, H. ,Hong, Z.,Zhou, H., Yang, Y., 2015. Under the potlight: The organic-inorganic hybrid halide perovskite for optoelectronic applications.NanoToday. 10, 355-396.

[12].Liu, X., Zhao, W., Cui, H.,Xie, Y.,Wang, Y.,Xu, T.,Huang, F.,Organic-inorganic halide perovskite based solar cells - Revolutionary progress in photovoltaics. Inorganic Chemistry Frontiers. 2 (2015) 315-335.

[13].Chang, J.,Chen, H.,Yuan, H.,Wang, B.,Chen, X.,. The mixing effect of organic cations on structural,electronic and optical properties of $FA_xMA_{1-x}PbI_3$perovskites.Physical Chemistry Chemical Physics. 20 (2017) 941-950.

[14].Zhou S, Ma Y, Zhou G, Xu X, Qin M, Li Y, Hsu Y, Hu H, Li G, Zhao N, Xu J, and Lu X,.Ag-doped halide perovskite nanocrystals for tunable band structure and efficient Charge transport. ACS Energy Letters. 4 (2019)534-541.

[15].Jiang L, Wu T, Sun L, Li Y, Li A, Lu R, Zou K, and Deng W, First principles screening of lead-free methylammonium metal iodine perovskites for photovoltaic application. The Journal of Physical Chemistry C. 121,44, (2017) 24359-24364.

[16].Zhang L .WangJ,Wu J. Mo S.iLong,Fe.·Zou, Z.Gao Y, Crystal structure, optical behavior and electrical conduction of the new organic–inorganic compound $CH_3NH_3CdI_3$. The Journal of Material science: Materials in Electonics. 12 (2018). 9821–9828.

[17].Ackland, G.J, Warren. M.C, Clark S.J. 1997. Practical methods in ab initio lattice dynamics, J,Phys, Condens. Matt, 9, 7861-7872.

[18].Perdew, J. P,Burke, K.,Ernzerhof, M., 1996. Generalized gradient approximation made simple,Phys.Rev. Lett,77,3865-3868.

[19].Krukau,A.V.,Vydrov,O.A., Izmaylov,A.F.;Scuseria,G.E. 2006. Influence of the exchange screening Parameter on the performance of screened hybrid functional. J.Chem.Phys.,125,224106

[20].Troullier,N.;Martins,J.L.1991. Efficient pseudopotentials for plane-wave calculations. Phys.Rev.B,43, 1993-2006

[21].Pfrommer,B.G., Louie, C. M., S.G. Cohen,M.L.,1997. Relaxation of crystals withthequasi-Newton method,J.Comput. Phys,13,233-240.

[22].Cui, J., Yuan, H., Li, J., Xu, X., Shen, Y. ,Lin ,H.,Wang, M., 2015.Recent progress in efficient hybrid lead halide perovskite solar cells.Sci. Technol. Adv. Mater. 16, 036004.

[23].Ji, D.,Xiao, X. J., Zhang, C. M.,Liy, X. L., Hu, M. Z., Yin., 2016.Regulatory band gap of vacancy at the B sites in $CH_3NH_3Pb_{1-x}I_3$perovskite.Modern Physics Letters B,Vol. 30, No. 23.

[24].Zhang, Y and Feng, J. 2016. $CH_3NH_3Cd_{0.875}Pb_{0.125}I_3$ perovskite as potential photovoltaic materials. AIP Advances 6.

[25].Jacobsson, T. J, Correa-Baena, J. P., Pazoki, M., Saliba, M., Schenk, K., Grätzel, M., Hagfeldt, A., An exploration of the compositional space for mixed lead halogen perovskites for high efficiency solar cells. Energy and Environmental Science. 9 (2016) 1706-1724.

[26].ChenQ, ChenL, YeF, ZhaoT, TangF, RajagopalA,Jiang Z, Jiang S, Y. Jen A-, Xie Y, Cai J, and Chen L., Ag-incorporated organic-inorganic perovskite films and planar heterojunction solar cells. NANO letters. 17 5 (2017) 3231-3237.

[27].Ye, Y., Run, X., Tao, X. H., Feng, H., Fei, X., Jun, W. L., 2015.Nature of the band gap of halide perovskites ABX_3(A = CH_3NH_3,Cs; B= Sn, Pb; X = Cl, Br, I): First-principles calculations.Chin. Phys. B Vol. 24, No. 11. 116302.

[28].Mladenovic, M.,Vukmirovic, N.,. Effects of thermal disorder on electronic structure of halide perovskites: Insights from MD simulations.Physical Chemistry Chemical Physics. 20 (2018) 25693-25700.

[29].Yin, W. J., Yang, J. H., Kang, J.,Yan, Y., Wei, S.H., Halide perovskite materials for solar cells: A theoretical review. Journal of Materials Chemistry A. 3 (2014) 8926-8942.

[30].Jishi, R. A., Ta, O. B., Sharif, A. A.,. Modeling of lead halide perovskites for Photovoltaic applications. Cond. Mat. 118 49 (2014)28344-28349.

[31].Wolf, S. D., Holovsky, J., Moon, S.J., Löper, P., Niesen, B., Ledinsky, M., Haug, F.J., Yum, J.H., Ballif, C., 2014.Organometallic halide perovskites: Sharp optical absorption edge and its relation to photovoltaic performance. J. Phys. Chem. Lett, 5, 1035 – 1039.

[32].Fan, Z.,Sun, K.,Wang, J., Perovskites for photovoltaics: a combined review of organic-inorganic halide perovskites and ferroelectric oxide perovskites. Journal of Materials Chemistry A. 3 (2015)18809-18828.

[33].Leguy, A. M. A., Azarhoosh, P., Alonso, M. I., Quiles, M. C.,Weber, O. J., Yao, J., Bryant, D., Weller, M. T., Nelson, J., Walsh , A., VSchilfgaarde, M.,Barnes, P.R. F., 2016. Experimental and theoretical optical properties of methylammonium lead halide perovskites. Nanoscale, 8, 6317.

CONCLUSION

Conclusion

In this thesis, it is concluded that the OMHPs are absorbers behaving as p-n junction solar cell. So, its stability against moisture, temperature, UV light and fabrication techniques are the major challenging improvements to profit from its high power conversion efficiency PCE.

In the thesis, $MAPbX_3$ (X=I, Br, Cl) and $MAB_xPb_{1-x}I_3$ (B_x=$Ag_{0.17}$or $Cd_{0.5}$) perovskites at their orthorhombic phase are basically described, using DFT-GGA and HSE06 methods implemented in CASTEP. These sub-families of perovskites are absorber materials, so their optoelectronic and mechanical properties are calculated.

Firstly, for $MAPbX_3$ (X=I, Br, Cl) group, the anisotropy affects the stiffness of each compound along x, y, z orientations. $MAPbI_3$ is the stiffest material with E_x=57.24 GPa and the trend; $E_{y,Cl}$=53.75 GPa>$E_{y,Br}$=33.33 GPa>$E_{y,I}$=26.84 GPa is observed. The results also show that the energy band gap can be tuned (from E_g=1.62 to 2. 2 to 2.74 eV) by varying halogens (from X=I to Br to Cl) respectively. Moreover, MA^+ has no significant effect on bonding charge distribution which is formed strongly by Pb^{2+} and (X=I, Br, Cl) atomic orbitals. The results show that $MAPbI_3$ has a wide band and strong α of 10^5 cm^{-1} in [1.65-3.26 eV] over the visible energy range. The obtained values state that anisotropy slightly affects the optical properties, particularly for $MAPbX_3$ (X=I, Br) in the NIR and UV range [3.1-5 eV]. Finally, the results show that when atomic number for the halide decreases, ε and n decrease for $MAPbX_3$ (X=I,Br,Cl).

For $MAB_xPb_{1-x}I_3$ (B=$Ag_{0.17}$ or $Cd_{0.5}$) group, the substitution of 17% Ag and 50% Cd into $MAPbI_3$ contracts the sizes of the $MAAg_{0.17}Pb_{0.83}I_3$ and $MAAB_{0.5}Pb_{0.5}I_3$ materials The results show that the Ag and Cd substitution tune the energy band gap, where for $MAPbI_3$ ($E_{g(PBE)}$=1.62 eV and $E_{g(HSE06)}$=1.77 eV), where $E_{g(PBE)}$=1.73 and $E_{g(HSE06)}$=1.69 for $MAAg_{0.17}Pb_{0.83}I_3$. Inconsistent values for $MACd_{0.5}/Pb_{0.5}I_3$ with $E_{g(PBE)}$=0.753 eV and $E_{g(HSE06)}$=1.288, albeit the HSE06 result better fits with Tauc plot optical band gap value E_{opt}=1.378 eV. Furthermore, the (MA^+) has no significant effect on bonding charge distribution that strongly occurs by Pb-6p and I-5p atomic orbitals in all compounds. The results show $MAPbI_3$ exhibits broad and high light absorbance (α=10^4-10^5 cm^{-1}) over the

visible spectrum, followed by $MAAg_{0.17}Pb_{0.83}I_3$ ($\alpha=10^4$–$0.6x10^5$ cm^{-1}) and least for $MACd_{0.5}Pb_{0.5}I_3$ ($\alpha=1.5x10^4$–$0.4x10^5$ cm^{-1}). Low anisotropic electron and hole effective masses characterize all compounds in the range of $0.043m_0$-$0.188m_0$, although the significant anisotropy effect has been found for $MAAB_{0.5}Pb_{0.5}I_3$. Finally, the 17% Ag^+ substitution into the $MAAPbI_3$ increases n and decreases κ. The calculated values for n are 2.90, 2.75 and 2.00 for $MAAg_{0.17}Pb_{0.83}I_3$, $MAPbI_3$ and $MACd_{0.5}Pb_{0.5}I_3$, respectively, at 2.5 eV energy peak value. The values for κ are 1.4, 1.8, and 1.2 for $MAAg_{0.17}Pb_{0.83}I_3$, $MAPbI_3$ and $MACd_{0.5}Pb_{0.5}I_3$, respectively, at 3.5 eV energy peak value.

Annex
cif. Files of used perovskites

1. $MAPbI_3$ (cif.file)

```
data_OptimizationMAPbI3\400\0015
_audit_creation_date              2020-01-30
_audit_creation_method            'Materials Studio'
_symmetry_space_group_name_H-M    'PNMA'
_symmetry_Int_Tables_number       62
_symmetry_cell_setting            orthorhombic
loop_
_symmetry_equiv_pos_as_xyz
  x,y,z
  -x+1/2,-y,z+1/2
  -x,y+1/2,-z
  x+1/2,-y+1/2,-z+1/2
  -x,-y,-z
  x+1/2,y,-z+1/2
  x,-y+1/2,z
  -x+1/2,y+1/2,z+1/2
_cell_length_a                    8.8480
_cell_length_b                    12.9289
_cell_length_c                    9.1361
_cell_angle_alpha                 90.0000
_cell_angle_beta                  90.0000
_cell_angle_gamma                 90.0000
loop_
_atom_site_label
_atom_site_type_symbol
_atom_site_fract_x
_atom_site_fract_y
_atom_site_fract_z
_atom_site_U_iso_or_equiv
_atom_site_adp_type
_atom_site_occupancy
H1     H     0.46378   0.31961   0.39461   0.00000  Uiso   1.00
H9     H     0.55974   0.31436   0.64489   0.00000  Uiso   1.00
I33    I     0.19953   0.01172   0.20081   0.00000  Uiso   1.00
H17    H     0.33916   0.25000   0.51485   0.00000  Uiso   1.00
H21    H     0.67962   0.25000   0.53414   0.00000  Uiso   1.00
C29    C     0.95003   0.25000   0.03866   0.00000  Uiso   1.00
I41    I     0.47815   0.25000   0.96793   0.00000  Uiso   1.00
Pb25   Pb    0.50000   0.00000   0.00000   0.00000  Uiso   1.00
N45    N     0.93050   0.75000   0.07712   0.00000  Uiso   1.00
loop_
_geom_bond_atom_site_label_1
_geom_bond_atom_site_label_2
_geom_bond_distance
_geom_bond_site_symmetry_2
_ccdc_geom_bond_type
H1     C29     1.094   4_455 S
H9     N45     1.041   2_665 S
I33    Pb25    3.234   .     S
```

```
I33     Pb25    3.258   2       S
H17     C29     1.096   4_455   S
H21     N45     1.050   2_665   S
C29     H1      1.094   4       S
C29     H1      1.094   6       S
C29     H17     1.096   4       S
C29     N45     1.495   3_745   S
I41     Pb25    3.251   1_556   S
I41     Pb25    3.251   3_656   S
Pb25    I33     3.234   5_655   S
Pb25    I41     3.251   1_554   S
Pb25    I41     3.251   3_646   S
Pb25    I33     3.258   2_554   S
Pb25    I33     3.258   6       S
N45     H9      1.041   2_664   S
N45     H9      1.041   8_654   S
N45     H21     1.050   2_664   S
N45     C29     1.495   3_755   S
```

2. $MAPbBr_3$ (cif.file)

```
data_Optimization\MAPbBr3\450\015
_audit_creation_date                2020-01-30
_audit_creation_method              'Materials Studio'
_symmetry_space_group_name_H-M      'PNMA'
_symmetry_Int_Tables_number         62
_symmetry_cell_setting              orthorhombic
loop_
_symmetry_equiv_pos_as_xyz
  x,y,z
  -x+1/2,-y,z+1/2
  -x,y+1/2,-z
  x+1/2,-y+1/2,-z+1/2
  -x,-y,-z
  x+1/2,y,-z+1/2
  x,-y+1/2,z
  -x+1/2,y+1/2,z+1/2
_cell_length_a                      7.9994
_cell_length_b                      12.0093
_cell_length_c                      8.6753
_cell_angle_alpha                   90.0000
_cell_angle_beta                    90.0000
_cell_angle_gamma                   90.0000
loop_
_atom_site_label
_atom_site_type_symbol
_atom_site_fract_x
_atom_site_fract_y
_atom_site_fract_z
_atom_site_U_iso_or_equiv
_atom_site_adp_type
_atom_site_occupancy
```

```
Br2     Br     0.29410   0.02882   0.71192   0.00000  Uiso   1.00
H1      H      0.02791   0.32401   0.12493   0.00000  Uiso   1.00
D1      H      0.00760   0.31980   0.84274   0.00000  Uiso   1.00
C1      C     -0.02047   0.25000   0.06374   0.00000  Uiso   1.00
N1      N      0.04897   0.25000  -0.09485   0.00000  Uiso   1.00
D2      H      0.17890   0.25000  -0.09539   0.00000  Uiso   1.00
Br1     Br    -0.03246   0.25000   0.48179   0.00000  Uiso   1.00
H2      H      0.84323   0.25000   0.04940   0.00000  Uiso   1.00
Pb1     Pb     0.00000   0.00000   0.50000   0.00000  Uiso   1.00
loop_
_geom_bond_atom_site_label_1
_geom_bond_atom_site_label_2
_geom_bond_distance
_geom_bond_site_symmetry_2
_ccdc_geom_bond_type
Br2     Pb1      3.006   .      S
Br2     Pb1      3.013   2      S
H1      C1       1.105   .      S
D1      N1       1.051   1_556  S
C1      H1       1.105   7      S
C1      N1       1.484   .      S
C1      H2       1.097   1_455  S
N1      D2       1.039   .      S
N1      D1       1.051   1_554  S
N1      D1       1.051   7_554  S
Br1     Pb1      3.018   .      S
Br1     Pb1      3.018   3_556  S
H2      C1       1.097   1_655  S
Pb1     Br2      3.006   5_556  S
Pb1     Br1      3.018   3_546  S
Pb1     Br2      3.013   2_554  S
Pb1     Br2      3.013   6_456  S
```

3. $MAPbCl_3$ (cif.file)

```
data_Opt\pr012\400
_audit_creation_date                2020-01-30
_audit_creation_method              'Materials Studio'
_symmetry_space_group_name_H-M      'PNMA'
_symmetry_Int_Tables_number         62
_symmetry_cell_setting              orthorhombic
loop_
_symmetry_equiv_pos_as_xyz
  x,y,z
  -x+1/2,-y,z+1/2
  -x,y+1/2,-z
  x+1/2,-y+1/2,-z+1/2
  -x,-y,-z
  x+1/2,y,-z+1/2
  x,-y+1/2,z
  -x+1/2,y+1/2,z+1/2
_cell_length_a                      11.4804
```

```
_cell_length_b                     11.6101
_cell_length_c                     11.5451
_cell_angle_alpha                  90.0000
_cell_angle_beta                   90.0000
_cell_angle_gamma                  90.0000
loop_
_atom_site_label
_atom_site_type_symbol
_atom_site_fract_x
_atom_site_fract_y
_atom_site_fract_z
_atom_site_U_iso_or_equiv
_atom_site_adp_type
_atom_site_occupancy
Pb1    Pb    0.25011   0.50054   0.22677   0.00000  Uiso   1.00
Cl2    Cl    0.29074   0.47369   0.47346   0.00000  Uiso   1.00
Cl3    Cl   -0.00623   0.47122   0.29343   0.00000  Uiso   1.00
H4     H     0.57865   0.17243   0.54762   0.00000  Uiso   1.00
H5     H     0.41109   0.32282   0.42019   0.00000  Uiso   1.00
H6     H    -0.05989   0.17250   0.59548   0.00000  Uiso   1.00
H7     H     0.06006   0.32227   0.42219   0.00000  Uiso   1.00
Cl8    Cl    0.22404   0.25000   0.22147   0.00000  Uiso   1.00
C9     C     0.52480   0.25000   0.54177   0.00000  Uiso   1.00
N10    N     0.46419   0.25000   0.42761   0.00000  Uiso   1.00
C11    C    -0.05727   0.25000   0.54158   0.00000  Uiso   1.00
N12    N     0.05456   0.25000   0.47580   0.00000  Uiso   1.00
H13    H     0.45886   0.25000   0.61027   0.00000  Uiso   1.00
H14    H     0.52426   0.25000   0.35985   0.00000  Uiso   1.00
H15    H    -0.12950   0.25000   0.47977   0.00000  Uiso   1.00
H16    H     0.12553   0.25000   0.53250   0.00000  Uiso   1.00
Cl17   Cl    0.27515   0.75000   0.21971   0.00000  Uiso   1.00
loop_
_geom_bond_atom_site_label_1
_geom_bond_atom_site_label_2
_geom_bond_distance
_geom_bond_site_symmetry_2
_ccdc_geom_bond_type
Pb1    Cl8     2.925   .     S
Pb1    Cl2     2.903   .     S
Pb1    Cl2     2.977   2_564 S
Pb1    Cl3     2.828   6     S
Pb1    Cl17    2.912   .     S
Cl2    Pb1     2.977   2_565 S
Cl3    Pb1     2.828   6_455 S
H4     C9      1.094   .     S
H5     N10     1.046   .     S
H6     C11     1.094   .     S
H7     N12     1.045   .     S
Cl8    Pb1     2.925   7     S
C9     N10     1.490   .     S
C9     H13     1.095   .     S
C9     H4      1.094   7     S
```

```
N10     H14     1.043   .      S
N10     H5      1.046   7      S
C11     N12     1.492   .      S
C11     H15     1.094   .      S
C11     H6      1.094   7      S
N12     H16     1.045   .      S
N12     H7      1.045   7      S
Cl17    Pb1     2.912   7_565  S
```

4. $MAPb_{0.83}Ag_{0.17}I_3$ (cif.file)

```
data_MAPb84Ag16I3(opt)
_audit_creation_date                    2020-01-30
_audit_creation_method                  'Materials Studio'
_symmetry_space_group_name_H-M          'P1'
_symmetry_Int_Tables_number             1
_symmetry_cell_setting                  triclinic
loop_
_symmetry_equiv_pos_as_xyz
  x,y,z
_cell_length_a                          8.4662
_cell_length_b                          12.7804
_cell_length_c                          9.1412
_cell_angle_alpha                       89.4603
_cell_angle_beta                        90.2675
_cell_angle_gamma                       90.1192
loop_
_atom_site_label
_atom_site_type_symbol
_atom_site_fract_x
_atom_site_fract_y
_atom_site_fract_z
_atom_site_U_iso_or_equiv
_atom_site_adp_type
_atom_site_occupancy
H1      H      0.50030   0.33394   0.38120   0.00000  Uiso   1.00
H2      H      0.51303   0.32131   0.64769   0.00000  Uiso   1.00
I3      I      0.17727   0.98376   0.18749   0.00000  Uiso   1.00
H4      H      0.99824   0.66667  -0.11520   0.00000  Uiso   1.00
H5      H      0.99428   0.67865   0.15235   0.00000  Uiso   1.00
I6      I      0.32278   0.01582   0.68690   0.00000  Uiso   1.00
H7      H      0.51390   0.80635   0.62337   0.00000  Uiso   1.00
H8      H      0.49718   0.81023   0.35994   0.00000  Uiso   1.00
I9      I      0.78798   0.48387   0.76801   0.00000  Uiso   1.00
H10     H     -0.01135   0.19306   1.12266   0.00000  Uiso   1.00
H11     H     -0.00413   0.18953   0.85860   0.00000  Uiso   1.00
I12     I      0.73118   0.51629   0.29010   0.00000  Uiso   1.00
H13     H      0.49977   0.66602   0.61894   0.00000  Uiso   1.00
H14     H      0.48727   0.67865   0.35242   0.00000  Uiso   1.00
I15     I      0.82271   0.01629   0.81228   0.00000  Uiso   1.00
H16     H      0.00188   0.33333   1.11507   0.00000  Uiso   1.00
H17     H      0.00573   0.32131   0.84752   0.00000  Uiso   1.00
```

```
I18    I     0.67725   0.98416   0.31301   0.00000  Uiso   1.00
H19    H     0.48618   0.19363   0.37678   0.00000  Uiso   1.00
H20    H     0.50308   0.18975   0.64017   0.00000  Uiso   1.00
I21    I     0.21192   0.51602   0.23156   0.00000  Uiso   1.00
H22    H     1.01146   0.80693  -0.12274   0.00000  Uiso   1.00
H23    H     1.00411   0.81042   0.14131   0.00000  Uiso   1.00
I24    I     0.26805   0.48360   0.70990   0.00000  Uiso   1.00
H25    H     0.33073   0.26912   0.45724   0.00000  Uiso   1.00
H26    H     0.66298   0.25413   0.57070   0.00000  Uiso   1.00
C27    C    -0.04164   0.26339   1.05942   0.00000  Uiso   1.00
I28    I     0.46446   0.25044   0.99337   0.00000  Uiso   1.00
H29    H     1.16969   0.73185  -0.04378   0.00000  Uiso   1.00
H30    H     0.84231   0.74650   0.07708   0.00000  Uiso   1.00
C31    C     0.54197   0.73605   0.56130   0.00000  Uiso   1.00
I32    I     0.03376   0.74359   0.50201   0.00000  Uiso   1.00
H33    H     0.66939   0.73085   0.54296   0.00000  Uiso   1.00
H34    H     0.33720   0.74584   0.42930   0.00000  Uiso   1.00
C35    C     1.04171   0.73659  -0.05952   0.00000  Uiso   1.00
I36    I     0.53505   0.74982   0.00720   0.00000  Uiso   1.00
H37    H    -0.16964   0.26813   1.04375   0.00000  Uiso   1.00
H38    H     0.15770   0.25348   0.92279   0.00000  Uiso   1.00
C39    C     0.45810   0.26392   0.43879   0.00000  Uiso   1.00
I40    I     0.96608   0.25656   0.49826   0.00000  Uiso   1.00
Pb41   Pb    0.50001   0.00004  -0.00001   0.00000  Uiso   1.00
Pb42   Pb    0.00004   0.00016   0.49986   0.00000  Uiso   1.00
Pb43   Pb    0.49997   0.50001   0.00002   0.00000  Uiso   1.00
Ag44   Ag   -0.00014   0.50001   0.49984   0.00000  Uiso   1.00
N45    N     0.96552   0.74326   0.08680   0.00000  Uiso   1.00
N46    N     0.53981   0.25690   0.58333   0.00000  Uiso   1.00
N47    N     0.03446   0.25670   0.91311   0.00000  Uiso   1.00
N48    N     0.46042   0.74307   0.41684   0.00000  Uiso   1.00
loop_
_geom_bond_atom_site_label_1
_geom_bond_atom_site_label_2
_geom_bond_distance
_geom_bond_site_symmetry_2
_ccdc_geom_bond_type
H1     C39     1.094   .      S
H2     N46     1.042   .      S
I3     Pb41    3.238   1_565  S
I3     Pb42    3.241   1_565  S
H4     C35     1.095   .      S
H5     N45     1.044   .      S
I6     Pb42    3.223   .      S
I6     Pb41    3.230   1_556  S
H7     C31     1.094   .      S
H8     N48     1.047   .      S
I9     Pb43    3.247   1_556  S
I9     Ag44    3.049   1_655  S
H10    C27     1.094   .      S
H11    N47     1.048   .      S
I12    Ag44    2.974   1_655  S
```

I12	Pb43	3.296	.	S
H13	C31	1.094	.	S
H14	N48	1.043	.	S
I15	Pb41	3.238	1_556	S
I15	Pb42	3.241	1_655	S
H16	C27	1.095	.	S
H17	N47	1.044	.	S
I18	Pb42	3.223	1_665	S
I18	Pb41	3.230	1_565	S
H19	C39	1.094	.	S
H20	N46	1.047	.	S
I21	Pb43	3.245	.	S
I21	Ag44	3.051	.	S
H22	C35	1.094	.	S
H23	N45	1.047	.	S
I24	Ag44	2.973	.	S
I24	Pb43	3.300	1_556	S
H25	C39	1.094	.	S
H26	N46	1.050	.	S
C27	H37	1.094	.	S
C27	N47	1.491	.	S
I28	Pb41	3.215	1_556	S
I28	Pb43	3.204	1_556	S
H29	C35	1.094	.	S
H30	N45	1.047	.	S
C31	H33	1.095	.	S
C31	N48	1.489	.	S
I32	Pb42	3.292	1_565	S
I32	Ag44	3.126	.	S
H34	N48	1.051	.	S
C35	N45	1.491	.	S
I36	Pb43	3.207	.	S
I36	Pb41	3.212	1_565	S
H38	N47	1.048	.	S
C39	N46	1.491	.	S
I40	Ag44	3.124	1_655	S
I40	Pb42	3.290	1_655	S
Pb41	I3	3.238	1_545	S
Pb41	I15	3.238	1_554	S
Pb41	I28	3.215	1_554	S
Pb41	I36	3.212	1_545	S
Pb41	I6	3.230	1_554	S
Pb41	I18	3.230	1_545	S
Pb42	I18	3.223	1_445	S
Pb42	I32	3.292	1_545	S
Pb42	I40	3.290	1_455	S
Pb42	I3	3.241	1_545	S
Pb42	I15	3.241	1_455	S
Pb43	I9	3.247	1_554	S
Pb43	I28	3.204	1_554	S
Pb43	I24	3.300	1_554	S
Ag44	I12	2.974	1_455	S

```
Ag44   I40      3.124   1_455 S
Ag44   I9       3.049   1_455 S
```

5. $MAPb_{0.5}Cd_{0.5}I_3$ (cif.file)

```
data_MAPbCdI3(opt)
_audit_creation_date                2020-01-30
_audit_creation_method              'Materials Studio'
_symmetry_space_group_name_H-M      'P1'
_symmetry_Int_Tables_number         1
_symmetry_cell_setting              triclinic
loop_
_symmetry_equiv_pos_as_xyz
  x,y,z
_cell_length_a                      8.5689
_cell_length_b                      12.7294
_cell_length_c                      9.2305
_cell_angle_alpha                   90.0000
_cell_angle_beta                    90.0000
_cell_angle_gamma                   90.0000
loop_
_atom_site_label
_atom_site_type_symbol
_atom_site_fract_x
_atom_site_fract_y
_atom_site_fract_z
_atom_site_U_iso_or_equiv
_atom_site_adp_type
_atom_site_occupancy
H1     H     0.49516   0.32098   0.38356   0.00000  Uiso   1.00
H2     H     0.52080   0.31627   0.64658   0.00000  Uiso   1.00
I3     I     0.20220   0.98518   0.20812   0.00000  Uiso   1.00
H4     H     1.00484   0.67902  -0.11644   0.00000  Uiso   1.00
H5     H     0.97920   0.68373   0.14658   0.00000  Uiso   1.00
I6     I     0.29780   0.01482   0.70812   0.00000  Uiso   1.00
H7     H     0.50484   0.82098   0.61644   0.00000  Uiso   1.00
H8     H     0.47920   0.81627   0.35342   0.00000  Uiso   1.00
I9     I     0.79780   0.48518   0.79188   0.00000  Uiso   1.00
H10    H    -0.00484   0.17902   1.11644   0.00000  Uiso   1.00
H11    H     0.02080   0.18373   0.85342   0.00000  Uiso   1.00
I12    I     0.70220   0.51482   0.29188   0.00000  Uiso   1.00
H13    H     0.50484   0.67902   0.61644   0.00000  Uiso   1.00
H14    H     0.47920   0.68373   0.35342   0.00000  Uiso   1.00
I15    I     0.79780   0.01482   0.79188   0.00000  Uiso   1.00
H16    H    -0.00484   0.32098   1.11644   0.00000  Uiso   1.00
H17    H     0.02080   0.31627   0.85342   0.00000  Uiso   1.00
I18    I     0.70220   0.98518   0.29188   0.00000  Uiso   1.00
H19    H     0.49516   0.17902   0.38356   0.00000  Uiso   1.00
H20    H     0.52080   0.18373   0.64658   0.00000  Uiso   1.00
I21    I     0.20220   0.51482   0.20812   0.00000  Uiso   1.00
H22    H     1.00484   0.82098  -0.11644   0.00000  Uiso   1.00
H23    H     0.97920   0.81627   0.14658   0.00000  Uiso   1.00
```

```
I24    I     0.29780   0.48518   0.70812   0.00000  Uiso   1.00
H25    H     0.33762   0.25000   0.46579   0.00000  Uiso   1.00
H26    H     0.67017   0.25000   0.57004   0.00000  Uiso   1.00
C27    C    -0.03689   0.25000   1.05604   0.00000  Uiso   1.00
I28    I     0.47402   0.25000   0.99853   0.00000  Uiso   1.00
H29    H     1.16238   0.75000  -0.03421   0.00000  Uiso   1.00
H30    H     0.82983   0.75000   0.07004   0.00000  Uiso   1.00
C31    C     0.53689   0.75000   0.55604   0.00000  Uiso   1.00
I32    I     0.02598   0.75000   0.49853   0.00000  Uiso   1.00
H33    H     0.66238   0.75000   0.53421   0.00000  Uiso   1.00
H34    H     0.32983   0.75000   0.42996   0.00000  Uiso   1.00
C35    C     1.03689   0.75000  -0.05604   0.00000  Uiso   1.00
I36    I     0.52598   0.75000   0.00147   0.00000  Uiso   1.00
H37    H    -0.16238   0.25000   1.03421   0.00000  Uiso   1.00
H38    H     0.17017   0.25000   0.92996   0.00000  Uiso   1.00
C39    C     0.46311   0.25000   0.44396   0.00000  Uiso   1.00
I40    I     0.97402   0.25000   0.50147   0.00000  Uiso   1.00
Pb41   Pb    0.50000   0.00000   0.00000   0.00000  Uiso   1.00
Cd42   Cd    0.00000   0.00000   0.50000   0.00000  Uiso   1.00
Pb43   Pb    0.50000   0.50000   0.00000   0.00000  Uiso   1.00
Cd44   Cd    0.00000   0.50000   0.50000   0.00000  Uiso   1.00
N45    N     0.95120   0.75000   0.08511   0.00000  Uiso   1.00
N46    N     0.54880   0.25000   0.58511   0.00000  Uiso   1.00
N47    N     0.04880   0.25000   0.91489   0.00000  Uiso   1.00
N48    N     0.45120   0.75000   0.41489   0.00000  Uiso   1.00
loop_
_geom_bond_atom_site_label_1
_geom_bond_atom_site_label_2
_geom_bond_distance
_geom_bond_site_symmetry_2
_ccdc_geom_bond_type
H1     C39     1.097   .      S
H2     N46     1.045   .      S
I3     Pb41    3.200   1_565  S
I3     Cd42    3.209   1_565  S
H4     C35     1.097   .      S
H5     N45     1.045   .      S
I6     Cd42    3.200   .      S
I6     Pb41    3.209   1_556  S
H7     C31     1.097   .      S
H8     N48     1.045   .      S
I9     Pb43    3.200   1_556  S
I9     Cd44    3.209   1_655  S
H10    C27     1.097   .      S
H11    N47     1.045   .      S
I12    Cd44    3.200   1_655  S
I12    Pb43    3.209   .      S
H13    C31     1.097   .      S
H14    N48     1.045   .      S
I15    Pb41    3.200   1_556  S
I15    Cd42    3.209   1_655  S
H16    C27     1.097   .      S
```

H17	N47	1.045	.	S
I18	Cd42	3.200	1_665	S
I18	Pb41	3.209	1_565	S
H19	C39	1.097	.	S
H20	N46	1.045	.	S
I21	Pb43	3.200	.	S
I21	Cd44	3.209	.	S
H22	C35	1.097	.	S
H23	N45	1.045	.	S
I24	Cd44	3.200	.	S
I24	Pb43	3.209	1_556	S
H25	C39	1.094	.	S
H26	N46	1.049	.	S
C27	H37	1.094	.	S
C27	N47	1.496	.	S
I28	Pb41	3.190	1_556	S
I28	Pb43	3.190	1_556	S
H29	C35	1.094	.	S
H30	N45	1.049	.	S
C31	H33	1.094	.	S
C31	N48	1.496	.	S
I32	Cd42	3.190	1_565	S
I32	Cd44	3.190	.	S
H34	N48	1.049	.	S
C35	N45	1.496	.	S
I36	Pb43	3.190	.	S
I36	Pb41	3.190	1_565	S
H38	N47	1.049	.	S
C39	N46	1.496	.	S
I40	Cd44	3.190	1_655	S
I40	Cd42	3.190	1_655	S
Pb41	I3	3.200	1_545	S
Pb41	I15	3.200	1_554	S
Pb41	I28	3.190	1_554	S
Pb41	I36	3.190	1_545	S
Pb41	I6	3.209	1_554	S
Pb41	I18	3.209	1_545	S
Cd42	I18	3.200	1_445	S
Cd42	I32	3.190	1_545	S
Cd42	I40	3.190	1_455	S
Cd42	I3	3.209	1_545	S
Cd42	I15	3.209	1_455	S
Pb43	I9	3.200	1_554	S
Pb43	I28	3.190	1_554	S
Pb43	I24	3.209	1_554	S
Cd44	I12	3.200	1_455	S
Cd44	I40	3.190	1_455	S
Cd44	I9	3.209	1_455	S

Published Works

Solar Energy 182 (2019) 9–15

Contents lists available at ScienceDirect

Solar Energy

journal homepage: www.elsevier.com/locate/solener

Optimized opto-electronic and mechanical properties of orthorhombic methylamunium lead halides ($MAPbX_3$) (X = I, Br and Cl) for photovoltaic applications

Mohammed Elmamoun Laamari[a], Ali Cheknane[a,*], Ali Benghia[b], Hikmat S. Hilal[c]

[a] Laboratoire des semiconducteurs et matériaux fonctionnels, Université Amar Telidji de Laghouat, Bd des martyrs, BP37G, 03000 Laghouat, Algeria
[b] Laboratoire de physique des matériaux, Université Amar Telidji de Laghouat, Bd des martyrs, BP37G, 03000 Laghouat, Algeria
[c] SSERL, Department of Chemistry, An-Najah National University, P.O. Box 7, Nablus, West Bank, Palestine

ARTICLE INFO

Keywords:
Perovskites
DFT
Optical absorption
Band gap tuning
Stiffness

ABSTRACT

Organometallic halide perovskites (OMHPs) are absorbent materials, and can thus be employed in solar cells with power conversion efficiency (PEC) of 22% or higher. Using calculations, this work confirms earlier experimental findings and determines optimal properties to achieve maximum conversion efficiency for OMHPs. Values of energy band gap, density of states, absorption coefficient, refractive index, dielectric constant and elastic constants of orthorhombic methylamunium lead halides ($MAPbX_3$) (X = I, Br and Cl) family are all calculated using Density Functional Theory (DFT) method with generalized gradient approximation (GGA). The stiffness of ($MAPbX_3$) (X = I, Br and Cl) is investigated by calculating Young's moduli E constants. Among the series, $MAPbI_3$ is the stiffest material with E_x = 57.24 GPa. The perovskite family members are characterized by their energy band gap variation as: $E_{g\ MAPbI3,\ MAPbBr3,\ MAPbCl3}$ = 1.626, 2.207 and 2.748 eV, respectively. They also exhibit a remarkable absorption coefficient ($\alpha_{\ MAPbX3} = 10^5\ cm^{-1}$) over a wide energy range particularly the visible spectrum [1.65–3.26 eV: 380–750 nm]. The anisotropy of optical properties ($MAPbX_3$) (X = I, Br) is proven in the near and middle ultraviolet [3.1–5 eV] energy band.

1. Introduction

Perovskites attract special interest among researchers. Perovskite structure and properties make it possible alternative in many applications. Organometallic halide perovskite (OMHP) based solar cells are being widely considered and known as light absorbers (Ji et al., 2016; Chen et al., 2015). Due to their chemical tunability, OMHP can also be tailored for various optoelectronic devices such as light emitting devices (LEDs), optical sensors (e.g. photodetectors), transistors(Zhao and Zhu, 2016); LASERS, light emitting electrochemical cells (LECs) (Chen et al., 2015) and spintronics (Hsiao et al., 2015). All in all, perovskites find their applications in different technologies, both combined and standalone systems (Yusoff and Nazeeruddin, 2016).

Emergence of OMHP in photovoltaic applications is due to their special absorptivity. OMHP absorbers are thus widely considered to enhance thin film PV cells of the 3rd generation (Kanhere et al., 2015; Ndione et al., 2016). They are among best materials with high power conversion efficiency (PCE). In dye-sensitized solar cells(Zhou et al., 2016), OMHPs have been used in devices with high PCE values (Chen et al., 2015; Hsiao et al., 2015) with high reported values of 22.7% (Qing et al., 2018). Therefore, OMHP systems have the prospect to reach commercial PV applications (Liu et al., 2018). In addition to all such features, OMHP devices can be prepared by simple methods (Quarti et al., 2015). Therefore, OMHP based photovoltaic devices have a prosperous future, and need more study aiming at enhancing their conversion efficiencies.

Methylamunium lead halides ($MAPbX_3$) (X = I, Br and Cl) form a sub-class of perovskites. They are characterized by excellent opto-electronic features such as high absorption coefficient, tunable energy band gap in the visible range, long range electron-hole transport length, and high carrier mobility (Ndione et al., 2016; Quarti et al., 2015) and (Song et al., 2015). Such features make these compounds good candidates for solar cells with high performance.

Iodine (I) based hybrid perovskites have been extensively studied for high PCE purposes. $MAPbX_3$ (X = I, Br and Cl) features can be simply monitored by changing the halide ions from one to another (Koliogiorgos et al., 2017). By knowing OMPH parameters, such as shape and band structure, which relate to the effective masses of charge

* Corresponding author.
E-mail address: a.cheknane@lagh-univ.dz (A. Cheknane).

https://doi.org/10.1016/j.solener.2019.02.035
Received 1 December 2018; Received in revised form 5 February 2019; Accepted 16 February 2019

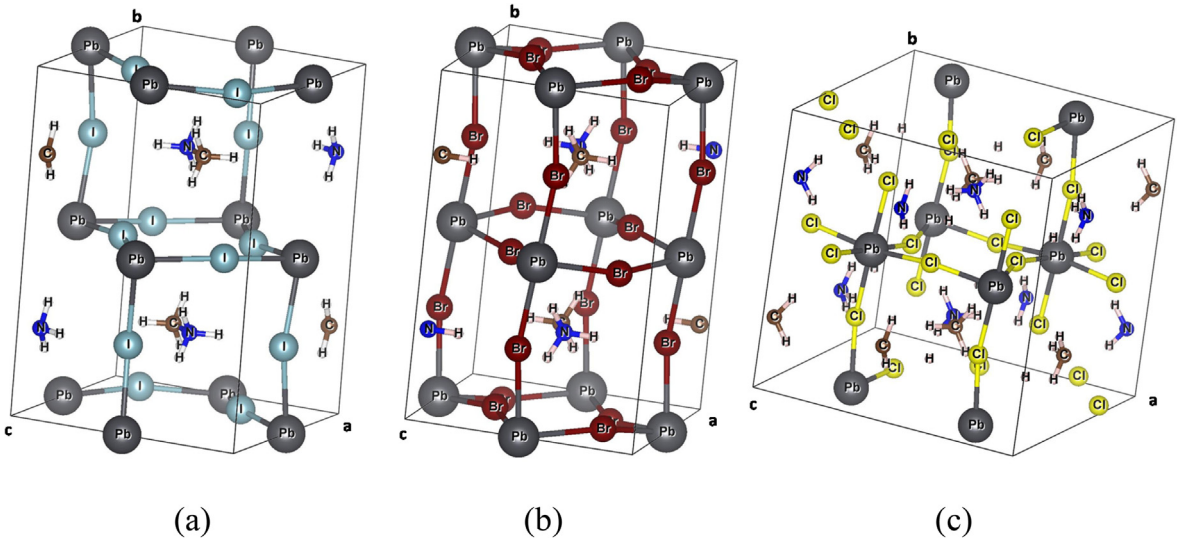

Fig. 1. Orthorhombic crystal structures for: (a) $MAPbI_3$ (b) $MAPbBr_3$ and (c) $MAPbCl_3$.

carriers and dielectric constants, the device physics can be understood, and techniques to develop their PV devices can be invented (Song et al., 2015).

Perovskites are represented by the general formula ABX_3, where A is an inorganic or organic cation, like $CH_3NH_3^+$(MA),$CH_5N_2^+$:FA),·…, B is a metal cation (Pb^{2+}, Sn^{2+}, …), and X is a halide anion (I^-, Br^-,Cl^-, F^-). This study is basically focused on $MAPbX_3$ (X = I^-, Br^- and Cl^-) fundamental properties. The $MAPbX_3$ crystal structure is described in literature. A metal ion Pb^{2+} with six neighbouring halide ions I, Br, or Cl share $[PbI_6]^{4-}$, $[PbBr_6]^{4-}$ or $[PbCl_6]^{4-}$ octahedra, respectively. Furthermore, each organic cation is coordinated by twelve halide anions as shown in Fig. 1 (Chang et al., 2017).

X-ray diffraction patterns show that $MAPbX_3$ (X = I, Br and Cl), depending on temperature, may have different phases and symmetries. As temperature increases, the structures vary from low temperature orthorhombic to tetragonal, and then to high temperature cubic perovskite structures (Chen et al., 2015; Manser et al., 2016). Literature also shows that when temperature increases, the symmetry of the perovskite increases too (Chen et al., 2015). $MAPbX_3$ (X = I, Br and Cl) is formed at low temperature gradually in an orthorhombic structure γ phase (pnma space group) as described in Fig. 1. For instance, such structures occur for $MAPbCl_3$ at < 172.9 K, for $MAPbBr_3$ at < 144.5 K and for $MAPbI_3$ at < 162.2 K) (Liu et al., 2012).

This work aims at quantitatively and qualitatively describing various intrinsic properties of $MAPbX_3$ (X = I, Br and Cl) as absorbent materials. Quantitative description involves ab-initio DFT based calculation of optimized properties, for the orthorhombic structures of $MAPbX_3$ (X = I, Br and Cl), such as their electronic band gap structures, density of states, dielectric constant and refraction index as well as their mechanical properties. Such studies have not been performed earlier to our knowledge. Qualitative description involves comparisons with other earlier studies. Finding optimal properties of $MAPbX_3$ that yield solar cells with higher conversion efficiency, and comparing such findings with earlier experimental studies is one main goal of this work. Such comparison has not been made earlier to our knowledge.

2. Computational methods

DFT theory based calculation is useful in perovskite characterization. In this study, all calculation results: bulk geometry optimization, electronic, optical and mechanical properties are acquired using plane wave basis- DFT method implemented in the Cambridge Sequential Total Energy Package (CASTEP, v 8.0) code. Ultra-soft pseudo potentials were adopted to describe the electron-ion interaction. The procedure Perdew-Burke-Ernzerhof (PBE) (Perdew et al., 1996) constructs the generalized gradient approximation (GGA) functional DFT to express the exchange - correlation energy.

Fast low energy scanning studies of $MAPbX_3$ (X = I, Br and Cl) structures were performed and cutoff kinetic energies were 400 eV for ($MAPBI_3$), 450 eV for ($MAPBBr_3$), and 400 eV for ($MAPbCl_3$). After checking convergence criteria, the Monkhorst-Pack of k-point mesh grid were fixed at 7 × 5 × 7 for ($MAPbI_3$), 8 × 6 × 8 for ($MAPbBr_3$) and 7 × 7 × 7 for ($MAPbCl_3$) for sampling Brillouin zone. Energy tolerance of 5×10^{-7} eV/atom was set to better probe the calculation. The electronic valence states of each atom are: MA: Pb: $5d^{10}$ $6s^2p^2$, I:$5s^2p^5$, Br:$4s^2p^5$, Cl:$3s^2p^5$, C: $2s^22p^2$, N: $2s^22p^2$, H:$1s^1$.

3. Results and discussion

3.1. Structural properties

Firstly, to study such $MAPbX_3$ (X = I, Br and Cl) crystal systems, the equilibrium lattice parameters were calculated using BFGS method for geometry optimization (Pfrommer et al., 1997) implemented in CASTEP. It allows refining a 3D system to obtain more stable and relaxed structure. The obtained lattice parameters (a × b × c) and the volume

Table 1
Calculated (DFT) and experimental lattice parameters values of $MAPbX_3$ (X = I, Br, Cl).

Compound calculated lattice parameters a, b, c (Å), V(Å^3)	Experimental value	References
$MAPbI_3$ a = 8.848, b = 12.928, c = 9.136 V = 1045.116	a = 8.861, b = 12.62, c = 8.581, V = 959.5	Liu et al. (2012)
$MAPbBr_3$ a = 7.999, b = 12.009, c = 8.675 V = 833.408	a = 7.979, b = 11.845, c = 8.58 V = 811.1	Swainson et al. (2003)
$MAPbCl_3$ a = 11.480, b = 11.610, c = 11.545 V = 1538.828	a = 11.193, b = 11.347, c = 11.287 V = 1432.5	Chia et al. (2005)

Table 2
Calculated elastic constants and Young's modulus of $MAPbX_3$ (X = I, Br, Cl).

Elastic constants (GPa)	$MAPbI_3$	$MAPbBr_3$	$MAPbCl_3$
c_{11}	65.85	26.44	48.80
c_{22}	29.99	40.21	54.20
c_{33}	34.01	27.32	52.36
c_{44}	3.81	7.12	14.39
c_{55}	18.86	11.62	17.73
c_{66}	0.61	5.20	14.76
c_{12}	0.66	10.97	3.68
c_{13}	16.49	14.27	6.21
c_{23}	9.79	12.67	3.42
Young's modulus	57.24	18.43	47.87
E_x, E_y, E_z	26.84	33.33	53.75
(GPa)	26.79	18.34	51.44

V are summarized in Table 1. The table shows that the calculated lattice parameters of $MAPbX_3$ (X = I, Br and Cl) by (DFT-GGA) method are consistent with the listed experimental values. These results are thus studied here to add credibility to findings acquired in following sections.

3.2. Elastic constants

The stability of perovskite based solar cell is affected by various factors which determine cell degradation, stress and strain (Chen et al., 2018). For example, the design, the fabrication and the industrial processing of OMHP solar cells may affect their mechanical properties (Feng, 2014). Therefore, the anisotropy on the Young's modulus and the elastic constants of $MAPbX_3$ (X = I, Br, Cl) are intentionally investigated here.

Table 2 summarizes the values of calculated elastic constants and Young's moduli E_x, E_y, E_z for $MAPbX_3$ (X = I, Br, Cl) compounds. After certain mathematical operations, the stability criteria for the used $MAPbX_3$ (X = I, Br, Cl), with orthorhombic structure, are well satisfied:

$c_{11} + c_{22}\text{-}2c_{12} > 0$, $c_{11} + c_{33} - 2c_{13} > 0$, $c_{22} + c_{33} - 2\,c_{23} > 0$, $c_{11} + c_{22} + c_{33} + 2c_{12} + 2c_{13} + 2c_{23} > 0$, $c_{11} > 0$, $c_{22} > 0$, $c_{33} > 0$, $c_{44} > 0$, $c_{55} > 0$, $c_{66} > 0$ (Feng, 2014). The obtained elastic constants are comparable to those reported (Feng, 2014) for both $MAPBX_3$ (X = I,Br). Moreover, Young's modulus values of $MAPbX_3$ (X = I, Br and Cl), along x, y and z faces, show the anisotropic stiffness for these materials. $MAPbX_3$ (X = I, Br) systems exhibit a clear contrast stiffness $E_{x,I}$ = 57.24 GPa and $E_{y,I}$ = 26.24 GPa, $E_{x,Br}$ = 18.43 GPa and $E_{y,Br}$ = 33.33 GPa, $E_{x,Cl}$ = 47.87 GPa and $E_{y,Cl}$ = 53.75 Gpa, as observed in the present work. Based on Young's modulus results, the tendency $E_{y,Cl} > E_{y,Br} > E_{yI,}$ confirms earlier literature(Sun et al., 2015).

3.3. Electronic properties

3.3.1. Electronic band structure

Since the $MAPbX_3$ (X = I, Br and Cl) compounds are established at their stable state, their electronic state band gaps are computed and shown in Fig. 2. The Figure shows the electronic band gap structures of $MAPbX_3$ (X = I, Br and Cl) along high symmetry path directions. The band gap values correspond to E_g = 1.626, 2.207 and 2.748 eV for $MAPbX_3$ (X = I, Br and Cl), respectively. All $MAPbX_3$ (X = I, Br and Cl) systems show a semiconductor behavior with direct band gap at Γ point. $MAPbX_3$ (X = I, Br and Cl) band structures well depict that the band gap values are inversely proportional to their corresponding halogen atomic numbers ($_{53}$I, $_{35}$Br, $_{17}$Cl). The present calculated band gap values are also consistent with those reported earlier (Ji et al., 2016; Liu et al., 2012; Cui et al., 2015) and in congruence with experimental values (Quarti et al., 2015).

The present results show that $MAPbI_3$ is more stable (−12500.3816 eV) than the earlier reported value (−12500.1 eV) (Ji et al., 2016). When performing band gap energy calculation, the result for $MAPbI_3$ E_g = 1.626 eV is slightly improved with respect to earlier one which showed $E_{gMAPbI3}$ = 1.656 eV value (Ji et al., 2016). Moreover, the energy band gap result for $MAPbCl_3$ $E_{gMAPbCl3}$ = 2.748 eV is found when performing calculation on the lattice of (a = 11.480, b = 11.610 and c = 11.545 Å) parameters. These parameters were used after screening for literature data. For example, the lattice parameters (a = 5.673, b = 5.628 and c = 11.182 Å) were cited in one earlier report for orthorhombic $MAPbCl_3$ (Liu et al., 2012); while they were (a = 11.193, b = 11.347, c = 11.287 Å) in another report (Sun et al., 2015). The present study thus gives more accurate values with higher credibility for parameters to be used in future calculations.

Energy diagrams found here show that gradual exchange of iodide with bromide, and then with chloride, in OMHP tunes band gap from 1.62 to 2.2 and to 2.7 eV, respectively. Such tuning, confirmed here opens a new scope for new OMHP applications, as described earlier (Jacobsson et al., 2016).

3.3.2. Density of sates

Fig. 3 shows that all $MAPbX_3$ (X = I, Br and Cl) compounds have the same energy distribution trend. The study shows that the MA-p state is located at −5 eV, far away from the Fermi level, and has a small effect on the band gap compared to other inorganic ions. The present results confirm the calculated partial density of states (PDOS) values reported earlier (Ye et al., 2015) that show a negligible density of states effect near the band edges. Moreover, MA^+ cation conserves the electronic equilibrium and stability of the structure. Recent literature shows that the interaction between MA^+ cation and $[PbX_3]^{4-}$ framework influences the orbital band compositions and consequently the crystal geometry (Fan et al., 2015).

The total (TDOS) and partial PDOS values are described in Fig. 3. The conduction band minimum (CBM) is mainly dominated by Pb-6p orbitals and remains unchanged for all compounds. On the other hand, the valence band maximum (VBM) is centered around halide ions p states (I-5p, Br-4p and Cl-3p) mixed with a small amount of Pb-6pPb-s states. Approximately, Pb cation and halide anions (I, Br, Cl) build the band gap energy edges (Mladenovic and Vukmirovic, 2018). No intense overlapping occurs between Pb-6p and (I-5p, Br-4p and Cl-3p) states which means weak Pb-X bonding (Yin et al., 2014).

Fig. 3 shows that the Pb-s and (I-p, Br-p and Cl-p states) are clearly visible at the same position from [−8 to −6 eV]. A hybrid state is clearly pointed between Pb-p and (I-p, Br-p and Cl-p) states over [−4 to 0 eV] energy band at the VBM and over [1.7 to 5 eV] energy band for the CBM as shown in Fig. 3.

3.3.3. Electron charge density and Mullikan population analysis

To probe more intrinsic characteristics of $MAPbX_3$ (X = I, Br and Cl), further explanations on charge distribution are depicted in Fig. 4.

The MA^+ cation shows very weak interaction and thus negligible overlap of electron orbitals between the organic component and the inorganic Pb-X octahedral. The behavior is present in all compounds. This feature is supported by the experimental contour plots of electron density for $MAPbBr_3$ reported earlier (Jishi et al., 2014). Finally, the interactions between Pb ions and X halide ions seem to be dominated by ionic character bonding.

Once such OMHP structure is optimized, assigning partial charges to atoms can be very useful to give an interpretation for charge distribution in compounds. Population analysis methods provide valuable insights into the interactions that give rise to bonding, where Mulliken's analysis is the most common population analysis method.

Electronic charges for atomic Mullikan population of Pb-X bonding are summarized in Table 3. The Table describes the partial charge value for each atom in Pb-X bonding. The more electronegative Cl, Br and I atoms attract electron density away from the less electronegative Pb atoms leaving them positively charged.

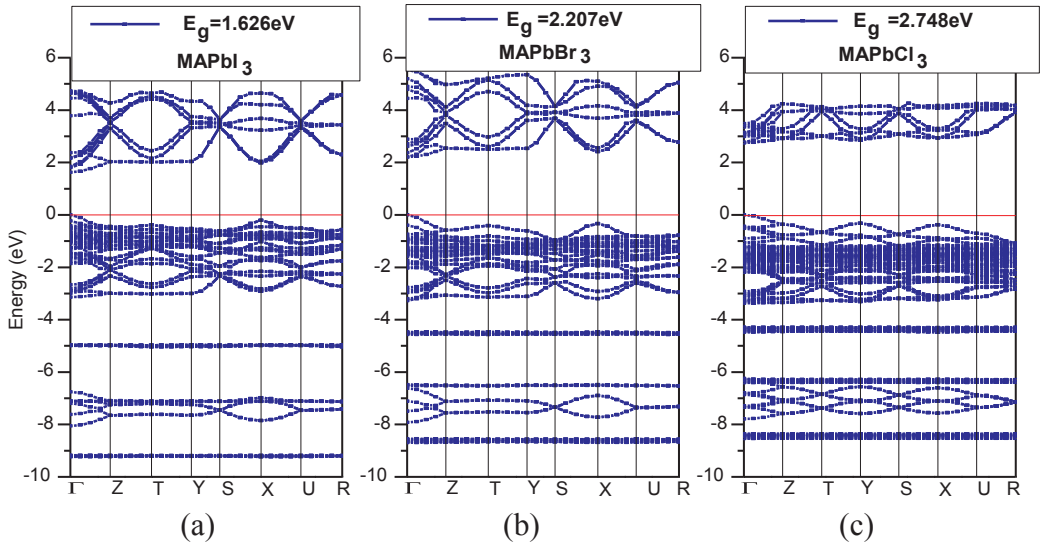

Fig. 2. Electronic band gap structures of (a) $MAPbI_3$, (b) $MAPbBr_3$ and (c) $MAPbCl_3$.

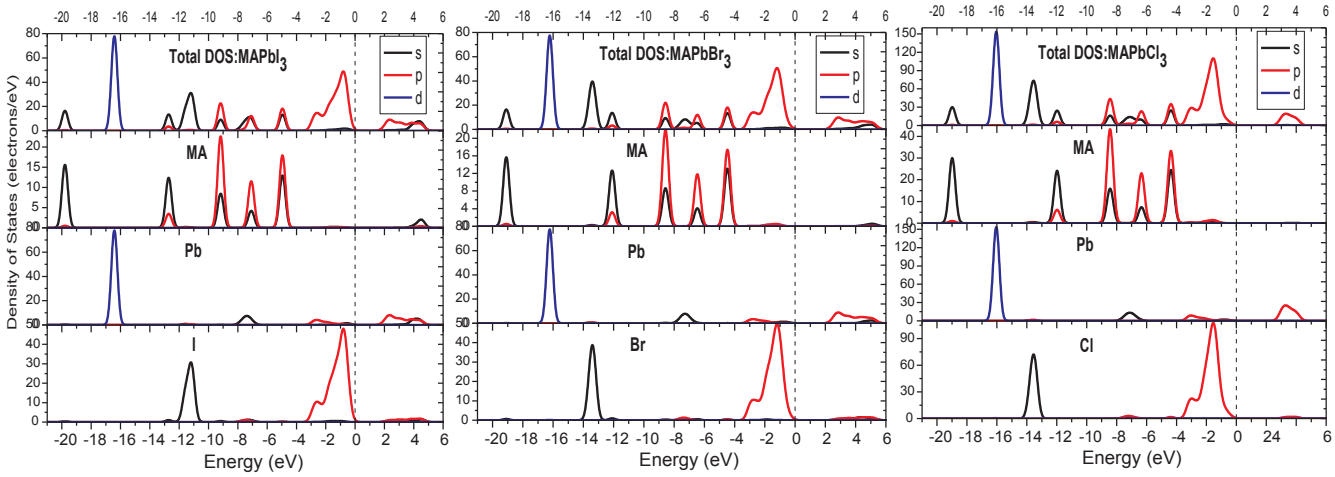

Fig. 3. Total and partial density of states (TDOS PDOS) of $MAPbX_3$ (X = I, Br and Cl).

3.4. Optical properties

The optical properties of orthorhombic $MAPbX_3$ (X = I, Br, Cl) can display anisotropy due to their asymmetry. This effect is included in the calculated results by taking the polarization direction of the electromagnetic field into account.

3.4.1. Absorption coefficient

The optical absorption coefficients of $MAPbX_3$ (X = I, Br, Cl) in different polarization directions are depicted in Fig. 5. The Figure shows the higher calculated absorption coefficient values ($\alpha = 10^4$–$10^5 cm^{-1}$) for each OMHP in all polarization directions. From the Figure, $MAPbI_3$, $MAPbBr_3$ and $MAPbCl_3$ present the same α trend and remain isotopic in all polarization directions over the visible energy band. $MAPbBr_3$ and $MAPbI_3$ exhibit a little anisotropy effect on the

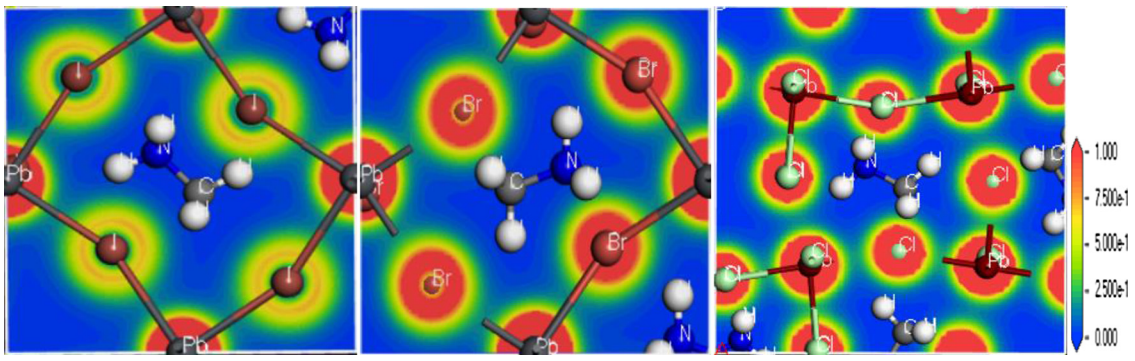

Fig. 4. Electron charge density distribution of $MAPbX_3$ (X = I, Br, Cl) ranging (0–1 e/A^3).

Table 3
Calculated Mulliken atomic population values in Pb-X (I, Br and Cl) bonds.

Compound	Ion	Atomic Mullikan population	Ion number
$MAPbI_3$	I(1)	−0.47	8
	I(2)	−0.40	4
	Pb	+0.82	4
$MAPbBr_3$	Br(1)	−0.47	8
	Br(2)	−0.41	4
	Pb	+0.96	4
$MAPbCl_3$	Cl(1)	−0.57	12
	Cl(2)	−0.58	8
	Cl(3)	−0.59	4
	Pb	+1.11	8

absorption peaks (4.5 and 3.5 eV) respectively in the near and middle ultraviolet [3.1–5.0 eV] energy bands with respect to polarization directions.

To get more insight into the absorption coefficient of $MAPbX_3$ (X = I, Br, Cl), a comparative presentation is shown in Fig. 6. The Figure shows that $MAPbI_3$ exhibits broad and high light absorbance ($\alpha = 10^4$ to 10^5 cm^{-1}) over the visible spectrum [1.65–3.26 eV: 380–750 nm]. Therefore, $MAPbI_3$ can is recommended in thin film absorber solar cells, as described earlier (Wolf et al., 2014) This absorption coefficient value is greater than those observed in conventional PV inorganic p-n junction materials such as $CuInGaSe_2$; CdTe and GaAs (Liu et al., 2012). Fig. 6 also shows that when halogen atomic size decreases (I, Br, Cl), light absorption decreases, accompanied by lowering of relative number of absorbed photons over the visible spectrum.

3.4.2. Dielectric constant

The dielectric constant or relative permittivity is a property that describes the ability of a medium to store electric field during dipole polarization. It is expressed as: $\varepsilon = \varepsilon' - i\varepsilon''$, where the real part ε' represents the charge storage ability and the imaginary part ε'' represents the energy loss. Only electronic polarization governs the dielectric process at optical (ultrahigh) frequencies. Fig. 7 shows that $MAPbI_3$ has $\varepsilon_{opt}' = 7$, in congruence with literature (Fan et al., 2015). It can thus be concluded that: when halogen atomic size decreases (I, Br, Cl), the electric field storage ability decreases but accompanied with only a minimum energy loss as shown in Fig. 7.

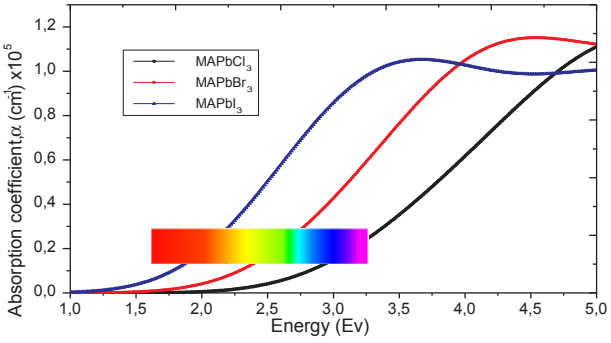

Fig. 6. Optical absorption coefficient α for $MAPbX_3$ (X = I, Br, Cl)at (0 0 1) polarization direction.

3.4.3. Refractive index

The refractive index values for $MAPbX_3$ (X = I, Br, Cl) in different polarization directions are shown in Fig. 8. $MAPbI_3$, $MAPbBr_3$ or $MAPbCl_3$ behave in the same way when interacting with the incident electromagnetic field but a sensible anisotropy is present when each of these materials responds to such specific polarization.

For comparison purposes, Fig. 9 shows the refraction index values for $MAPbX_3$ (X = I, Br, Cl) at (0 0 1) polarization direction. The values vary as $n_{MAPbI3} > n_{MAPbBr3} > n_{MAPbCl3}$ along short wavelengths. The calculated values are comparable with literature (Leguy et al., 2016) for $MAPbX_3$ (X = I, Br, Cl) in their pseudo cubic phase, in term of the behaviour and effect of the anisotropy on the refractive index and extinction coefficient on $MAPbX_3$ (X = I, Br, Cl). It should be kept in mind that the present results specifically describe orthorhombic $MAPbX_3$ (X = I, Br, Cl) materials.

4. Conclusion

$MAPbX_3$ (X = I, Br, Cl) perovskites at their orthorhombic phase are basically described, in the present work, using DFT-GGA method implemented in CASTEP. The $MAPbX_3$ (X = I, Br, Cl) perovskites are absorber materials, so their optoelectronic and mechanical properties are calculated. Firstly, the calculated elastic constant values agree with other earlier literature. Secondly, the anisotropy affects the stiffness of each compound along x, y, z orientations. $MAPbI_3$ is the stiffest material with E_x = 57.24 GPa and the trend; $E_{y,Cl}$ = 53.75 GPa > $E_{y,Br}$ = 33.33

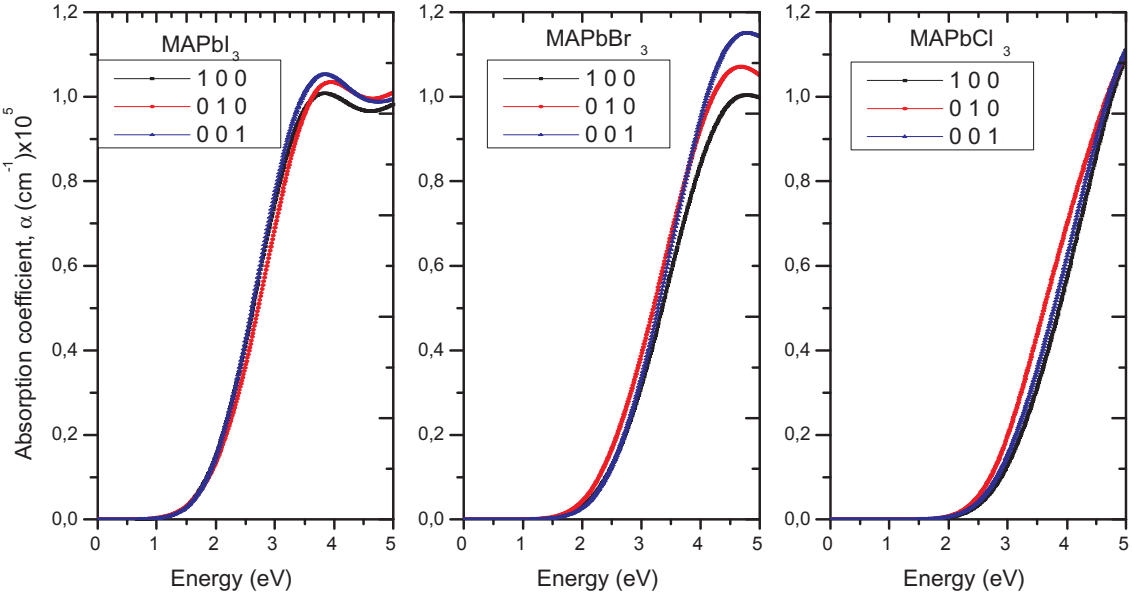

Fig. 5. Optical absorption coefficients α of $MAPbX_3$ (X = I, Br, Cl) in different polarization directions.

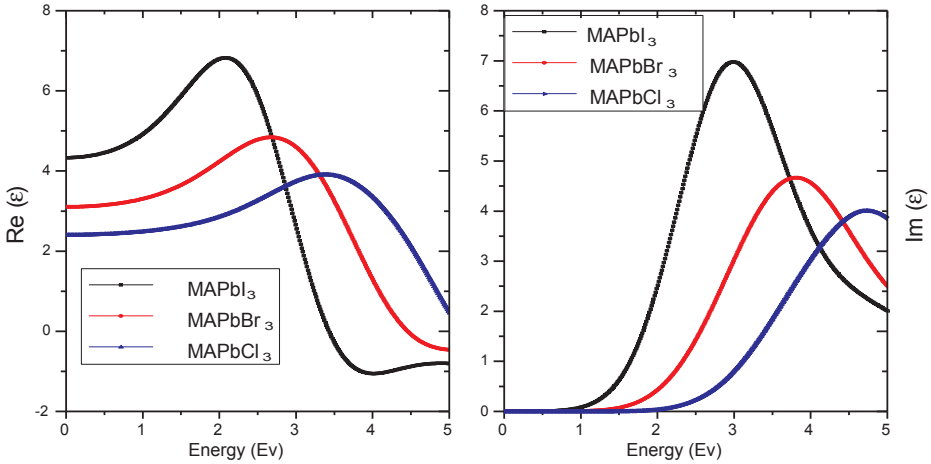

Fig. 7. Re(ε) and Im(ε) of $MAPbX_3$ (X = I, Br, Cl) at (0 0 1) polarization direction.

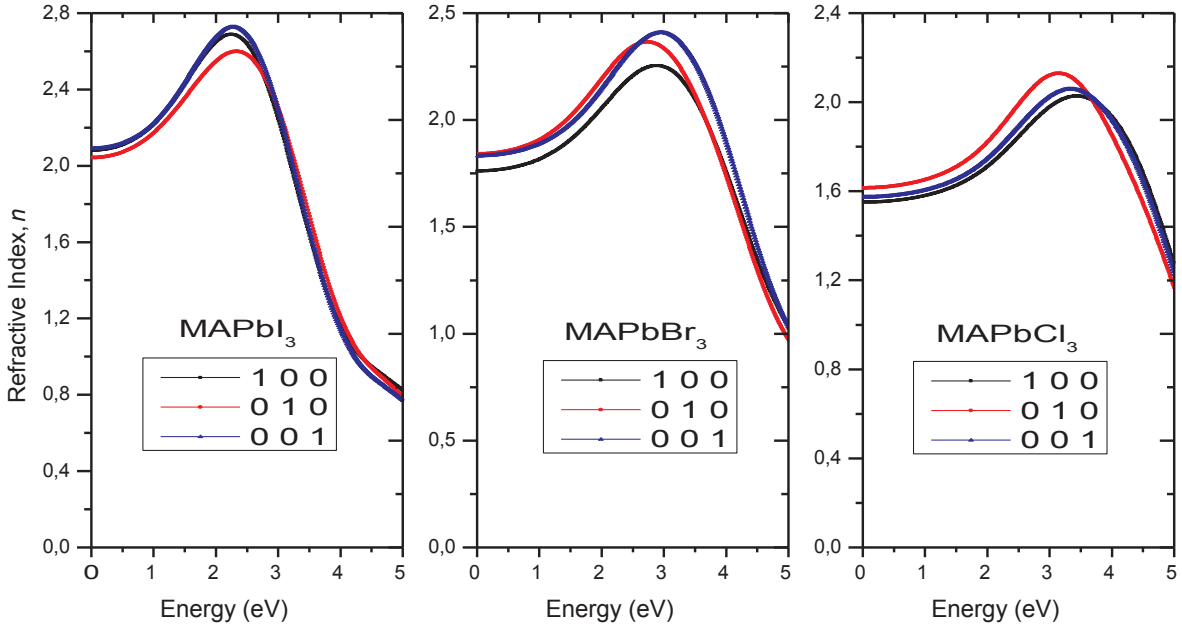

Fig. 8. Refractive index *n* of $MAPbX_3$ (X = I, Br, Cl) in different polarization directions.

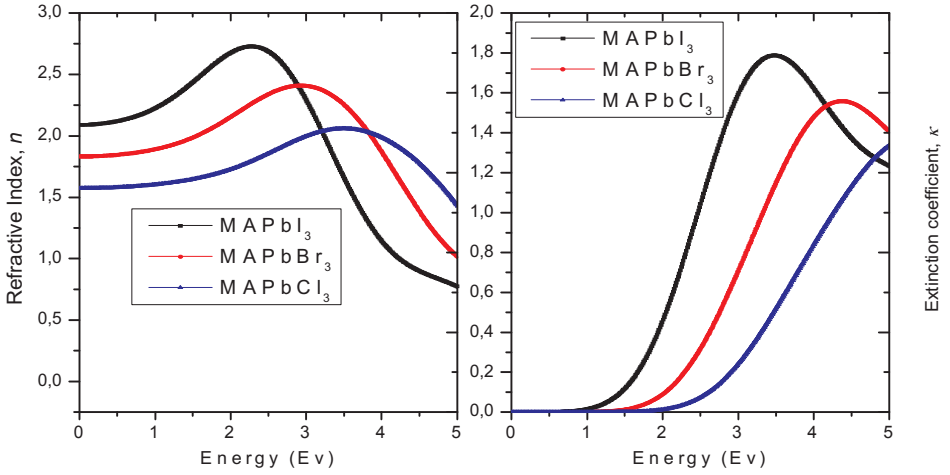

Fig. 9. Calculated refractive index and extinction coefficients of $MAPbX_3$ (X = I, Br, Cl) at (0 0 1) polarization direction.

GPa > $E_{y,I}$ = 26.84 GPa is observed.

The results also show that the energy band gap can be tuned (from E_g = 1.62 to 2.2 to 2.74 eV) by varying halogen atoms (from X = I to Br to Cl), respectively. Moreover, MA^+ has no significant effect on charge distribution in bonds formed strongly between $Pb^{2+}$and (X = I, Br, Cl) atomic orbitals. The results show that $MAPbI_3$ has a wide band gap and strong absorption coefficient of 10^5 cm^{-1} in visible range [1.65–3.26 eV: 380–750 nm]. The calculated values state that anisotropy slightly affects the optical properties, particularly for $MAPbX_3$ (X = I, Br) in the near and mid ultraviolet range [3.1–5.0 eV]. Finally, the results show that when atomic number for the halide decreases, the dielectric constant and refractive index values decrease for $MAPbX_3$ (X = I, Br, Cl).

Acknowledgement

Authors would like to thank “Université Amar Telidji de Laghouat, Algérie” for the financial support.

References

Chang, J., Chen, H., Yuan, H., Wang, B., Chen, X., 2017. The mixing effect of organic cations on structural, electronic and optical properties of $F_AxM_{A1x}Pb_I3$ perovskites. PCCP.

Chen, Q., Marco, N.D., Yang, Y., Song, T.B., Chen, C.C., Zhao, H., Hong, Z., Zhou, H., Yang, Y., 2015. Under the potlight: the organic-inorganic hybrid halide perovskite for optoelectronic applications. Nano Today 10, 355–396.

Chen, A., Youssef, M., Zhang, C., 2018. Strain effect on the performance of amorphous silicon and perovskite solar cells. Sol. Energy 163, 243–250.

Chen, J., Zhou, S., Jin, S., Zhai, T., 2015. Crystal organometal halide perovskites with promising optoelectronic applications. J. Mater. Chem. C.

Chia, L., Swainsona, I., Cranswick, L., Herb, J.H., Stephens, P., Knop, O., 2005. The ordered phase of methylammonium lead chloride $CH_3NH_3PbCl_3$. J. Solid State Chem. 178, 1376–1385.

Cui, J., Yuan, H., Li, J., Xu, X., Shen, Y., Lin, H., Wang, M., 2015. Recent progress in efficient hybrid lead halide perovskite solar cells. Sci. Technol. Adv. Mater. 16 036004.

Fan, Z., Sun, K., Wang, J., 2015. Perovskites for photovoltaics: a combined review of organic-inorganic halide perovskites and ferroelectric oxide perovskites. J. Mater. Chem. A.

Feng, J., 2014. Mechanical properties of hybrid organic-inorganic $CH_3NH_3BX_3$ (B = Sn, Pb; X = Br, I) perovskites for solar cell absorbers. APL Mater. 2 081801.

Hsiao, Y., Wu, T., Li, M., Liu, Q., Qin, W., Hu, B., 2015. Fundamental physics behind high efficiency organometal halide perovskite solar cells. J. Mater. Chem. A 3, 15372.

Jacobsson, T.J., Correa-Baena, J.P., Pazoki, M., Saliba, M., Schenk, K., Grätzel, M., Hagfeldt, A., 2016. An exploration of the compositional space for mixed lead halogen perovskites for high efficiency solar cells. Energy Environ. Sci.

Ji, D., Xiao, X.J., Zhang, C.M., Liy, X.L., Hu, M.Z., Yin, 2016. Regulatory band gap of vacancy at the B sites in $CH_3NH_3Pb_{1x}I_3$ perovskite. Mod. Phys. Lett. B 30 (23).

Jishi, R.A., Ta, O.B., Sharif, A.A., 2014. Modeling of lead halide perovskites for photovoltaic applications. Cond Mat.

Kanhere, P., Chakraborty, S., Rupp, C.J., Ahujabd, R., Chen, Z., 2015. Substitution induced band structure shape tuning in hybrid perovskites (CH_3 $NH_3Pb_{1x}Sn_x$ I_3) for efficient solar cell applications. RSC Adv 5 (1), 07497.

Koliogiorgos, A., Baskoutas, S., Galanakis, I., 2017. Electronic and gap properties of lead-free perfect and mixed hybridhalide perovskites: an ab-initio study. Comput. Mater. Sci. 138, 92–98.

Leguy, A.M.A., Azarhoosh, P., Alonso, M.I., Quiles, M.C., Weber, O.J., Yao, J., Bryant, D., Weller, M.T., Nelson, J., Walsh, A., VSchilfgaarde, M., Barnes, P.R.F., 2016. Experimental and theoretical optical properties of methylammonium lead halide perovskites. Nanoscale 8, 6317.

Liu, D., Li, S., Bian, F., Meng, X., 2018. First principles investigation on the electronic and mechanical properties of Cs-doped $CH_3NH_3PbI_3$. Materials.

Liu, X., Zhao, W., Cui, H., Xie, Y., Wang, Y., Xu, T., Huang, F., 2012. Organic-inorganic halide perovskite based solar cells – revolutionary progress in photovoltaics. Inorg. Chem. Front.

Manser, J.S., Christians, J.A., Kamat, P.V., 2016. Intriguing optoelectronic properties of metal halide perovskites. Chem. Rev. 116, 12956–13008.

Mladenovic, M., Vukmirovic, N., 2018. Effects of thermal disorder on electronic structure of halide perovskites: insights from MD simulations. PCCP.

Ndione, P.F., Li, Z., Zhu, K., 2016. Effects of alloying on optical properties of organic-inorganic lead halide perovskite thin films. J. Mater. Chem. C.

Perdew, J.P., Burke, K., Ernzerhof, M., 1996. Generalized gradient approximation made simple. Phys. Rev. Lett 77, 3865–3868.

Pfrommer, B.G., Louie, C.M., Cohen, S.G., M. L.,, 1997. Relaxation of crystals with the quasi-Newton method. J. Comput. Phys 13, 233–240.

Qing, B., Wei, W., Zhou, Y., Dong, Y., 2018. Photoelectric performance and stability comparison of $MAPbI_3$ and $FAPbI_3$ perovskites solar cells. Sol. Energy 174, 933–939.

Quarti, C., Mosconi, E., Ball, J.M., D'Innocenzo, V., Tao, C., Pathak, S., Snaith, H.J., Petrozza, A., Angelis, F.D., 2015. Structural and optical properties of methylammonium lead iodide across the tetragonal to cubic phase transition: implications for perovskite solar cells. Energy Environ. Sci.

Song, T.B., Chen, Q., Zhou, H., Jiang, C., Wang, H.H., Yang, M., Liu, Y.S., You, J., Yang, Y., 2015. Perovskite solar cells: film formation and properties. J. Mater. Chem. A.

Sun, S., Fang, Y., Kieslich, G., White, T.J., Cheetham, A.K., 2015. Mechanical properties of organic-inorganic halide perovskites, $CH_3NH_3PbX_3$ (X = I, Br and Cl), by nano-indentation. J. Mater. Chem. C.

Swainson, I.P., Hammond, R.P., Soullie're, C., Knop, O., Massa, W., 2003. Phase transitions in the perovskite methylammonium lead bromide, CH_3Nh_3PbBr 3. J. Solid State Chem. 176, 97–104.

Wolf, S.D., Holovsky, J., Moon, S.J., Löper, P., Niesen, B., Ledinsky, M., Haug, F.J., Yum, J.H., Ballif, C., 2014. Organometallic halide perovskites: sharp optical absorption edge and its relation to photovoltaic performance. J. Phys. Chem. Lett 5, 1035–1039.

Ye, Y., Run, X., Tao, X.H., Feng, H., Fei, X., Jun, W.L., 2015. Nature of the band gap of halide perovskites ABX_3(A = CH_3NH_3, Cs; B= Sn, Pb; X = Cl, Br, I): first-principles calculations. Chin. Phys. B 24 (11) 116302.

Yin, W.J., Yang, J.H., Kang, J., Yan, Y., Wei, S.H., 2014. Halide perovskite materials for solar cells: a theoretical review. J. Mater. Chem. A.

Yusoff, A.R.B.M., Nazeeruddin, K.M., 2016. Organohalide lead perovskites for photovoltaic applications. J. Phys. Chem Lett.

Zhao, Y., Zhu, K., 2016. Organic–inorganic hybrid lead halide perovskites for optoelectronic and electronic applications. Chem. Soc. Rev. 45, 655.

Zhou, Y., Wang, F., Fang, H.H., Loi, M.A., Xie, F.Y., Zhoa, N., Wong, C.P., 2016. Distribution of bromine in mixed iodide-bromide organolead perovskites and its impact on photovoltaic performance. J. Mater. Chem. A.

Organic Electronics 75 (2019) 105393

Contents lists available at ScienceDirect

Organic Electronics

journal homepage: www.elsevier.com/locate/orgel

Effect of metal (Ag and Cd) substitution on methylammonium lead iodideperovskiteMAPbI3optoelectronic properties for photovoltaic applications

Mohammed Elmamoun Laamari[a], Ali Cheknane[a,*], Hikmat S. Hilal[b], Ali Benghia[c]

[a] Laboratoire des Semiconducteurs et Matériaux Fonctionnels. Université Amar Telidji de Laghouat, Bd des Martyrs, BP37G, 03000, Laghouat, Algeria
[b] SSERL, Department of Chemistry, An-Najah National University, P.O. Box 7, Nablus, West Bank, Palestine
[c] Laboratoire de Physique des Matériaux. Université Amar Telidji de Laghouat, Bd des Martyrs, BP37G, 03000, Laghouat, Algeria

ARTICLE INFO

Keywords:
Organometallic halide perovskites
Optoelectronic properties
Band gap tuning
Density of states
Dielectric constant

ABSTRACT

Organometallic perovskite (OMHP) based solar cells, with higher than 24% of power conversion efficiency (PCE), attract special attention. High absorption coefficient is a property of such OMHPs. In this work the organometallic halide perovskite, methylamunium lead iodide ($MAPbI_3$), is partially substituted with two Ag and Cd atoms. The effect of substitution on structural and optoelectronic properties of the perovskite is studied, based on the ab-initio DFT method. Properties of $MAPbI_3$ and$MAAB_xPb_{1-x}I_3$(B_x = $Ag_{0.17}$ or $Cd_{0.5}$) perovskites, in their orthorhombic phase, are described. The energy band gaps are calculated here with PBE-GGA and HSE06 methods. The $MAPbI_3$ is characterized by its high absorption coefficient over the visible spectrum [1.65–3.26 eV: 750- 380 nm] compared to $MAAg_{0.17}Pb_{0.83}I_3$ ($\alpha = 10^4$–$0.6 \times 10^5 cm^{-1}$), and $MACd_{0.5}Pb_{0.5}I_3$ ($\alpha = 1.5 \times 10^4$ – $0.4 \times 10^5 cm^{-1}$). Low anisotropic electron and hole effective masses are calculated for all compounds in the range of 0.043 m_o-0.188 m_o. The anisotropy in optical properties for $MACd_{0.5}Pb_{0.5}I_3$, such as the absorption coefficient α, the dielectric constant ε and the refractive index n, is noticed. Enhancement in refractive index *n* of $MAAg_{0.17}Pb_{0.83}I_3$is also observed. The calculated values for n are 2.90, 2.75 and 2.00 for $MAAg_{0.17}Pb_{0.83}I_3$, $MAPbI_3$ and $MACd_{0.5}Pb_{0.5}I_3$, respectively, at 2.5 eV energy peak value. The values for κ are 1.4, 1.8, and 1.2 for $MAAg_{0.17}Pb_{0.83}I_3$, $MAPbI_3$ and $MACd_{0.5}Pb_{0.5}I_3$, respectively, at 3.5 eV energy peak value.

1. Introduction

Organometallic halide perovskites (OMHP)are widely considered in photovoltaic applications partly due to their special absorptivity [1,2]. OMHP based dye-sensitized solar cells, exhibit high power conversion efficiency (PCE)of 22.7% [3–6]. OMHP based solar cells may potentially have commercial application [7] due their simple fabrication and efficient architecture [8]. With promising future, OMHP based PV devices deserve more study to optimize their conversion efficiencies.

Methylamunium lead iodide ($MAPbI_3$) has special optoelectronic features, such as high absorption coefficient, tunable band gap energy in the visible range, long range electron-hole transport lengths and high carrier mobility [2,8,9]. Such features highlight the importance of $MAPbI_3$ systems in high performance solar cells.

X-ray diffraction patterns show that $MAPbI_3$involves various phases and symmetries at different temperatures. By increasing temperature, the crystal structure changes from orthorhombic to tetragonal, and then to high-temperature cubic perovskite [5,10]. Consequently, the perovskite symmetry increases as the temperature increases [11]. At low temperatures, precisely below 162.2 K, $MAPbI_3$ is gradually formed in the orthorhombic γ phase, with (pnma) space group [12], as described in Fig. 1(a).

This study aims at investigating fundamental properties of the $MAPbI_3$ orthorhombic phase. Analytically, the formability and stability of orthorhombic $MAPbI_3$ are justified by satisfying the octahedral factor μ and the tolerance factor t defined by:

$$\mu = r_{Pb}/r_I \quad (1)$$

$$t = (r_{MA} + r_I)/\sqrt{2}\,(r_{Pb} + r_I) \quad (2)$$

where r_{MA}, r_{Pb} and r_I are the ionic radii of MA^+, Pb^{2+} and I^- ions respectively.

As discussed above, the $MAPbI_3$ crystal structure is described earlier. So, the $MAPbI_3$ resembles inorganic framework crystal structures.

* Corresponding author.
E-mail address: a.cheknane@lagh-univ.dz (A. Cheknane).

https://doi.org/10.1016/j.orgel.2019.105393
Received 30 May 2019; Received in revised form 5 July 2019; Accepted 31 July 2019
Available online 02 August 2019

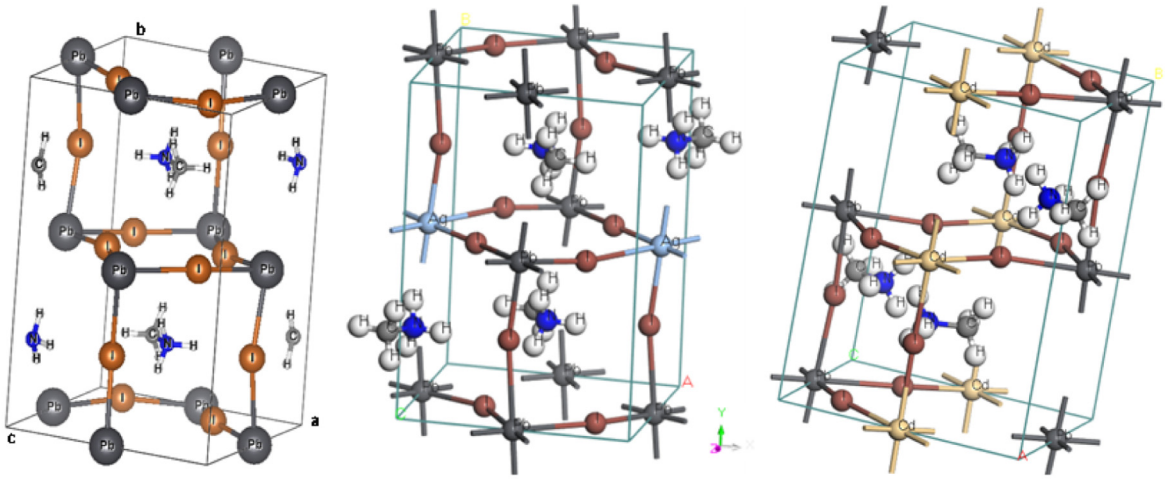

Fig. 1. Proposed orthorhombic crystal structures of(a) $MAPbI_3$ (b) $MAAg_{0.17}Pb_{0.83}I_3$and (c) $MACd_{0.5}Pb_{0.5}I_3$.

A metal ion $Pb^{2+}$with six neighbouring iodide I^- ions share a $[PbI_6]^{4-}$octahedron.The MA cations are located between $[PbI_6]^{4-}$octahedra, where each organic cation is coordinated to twelve iodide ions, as shown in Fig. 1(a), [13].

Despite the advantages of $MAPbI_3$, it suffers two shortcomings. Firstly it has low stability, which limits its commercial value. Secondly, it involves the hazardous Pb^{2+} ions which may lead to environmental problems in case of wide commercial application, keeping in mind the low perovskite stability. Therefore, further study is needed to stabilize the perovskite and/or lower the lead ion concentrations.

Recently, the Pb^{2+}ions have been substituted with other metal cations, aiming at enhancing the properties of the $MAPbI_3$perovskite. Different metals are investigated for this purpose. Monovalent substitution, with ions such as those of Cu, Na, Ag and others, significantly affects the perovskite properties, and consequently the solar cell performance [14]. Mn^{2+}, Zn^{2+}, Sn^{2+}, Ge^{2+}, Cd^{2+}, and others were examined as isovalent replacement for the toxic lead ion in $MAPbI_3$perovskite on one hand, and to tune the material optoelectronic properties on the other hand [15].

In the present work, two ions (Ag^+ and Cd^{2+}) are chosen as partial substituents for lead ion to yield the orthorhombic $MAB_xPb_{1-x}I_3$ ($B_x = Ag_{0.17}$ or $Cd_{0.5}$) systems. The goal is many-fold. Using lower lead ion content should lower the environmental impact of the new systems. Investigating Ag^+ and Cd^{2+} ions, including effect of valence state ($4\,d^{10}$) on the electronic interactions and the optical properties of the new systems, is another goal. Moreover, stability assessment of the new system is beneficial for environmental purposes.

Ag^+ ion, which has not been widely described before as dopant in $MAPbI_3$, is chosen as a substituent element because its ionic radius (1.15Å) is soundly close to that of Pb^{2+}(1.19 Å). Hopefully, the substitution may have minimal effect on the new system structural properties. A compromised control of the substituted concentration is of interest, between the Ag^+ excess that leads to a metallic behavior of $MAAg_xPb_{1-x}I_3$and the desirable tuned properties.

Cadmium ion (Cd^{2+}) has ionic radius of 0.95 Å. Like Pb^{2+}, Cd^{2+} is environmentally not friendly. The Cd partial substitution into $MAPbI_3$ is still under investigation due to in consistent theoretical and experimental findings in literature [16]. Dependence of band gap value and orthorhombic phase stability with respect to the Cd substitution concentration needs further study.

Using ab-initio DFT based calculations, the structural and the optoelectronic properties (including electronic band gap structure, density of states, dielectric constant and refraction index)are comparatively studied here for the orthorhombic $MAPbI_3$, and for the proposed systems $MAAg_{0.17}Pb_{0.83}I_3$and $MACd_{0.5}Pb_{0.5}I_3$. Structures for these systems are summarized in Fig. 1.

2. Computational methods

DFT theory based calculation is useful for perovskite characterization. In this study, all calculation results: bulk geometry optimization, electronic and optical properties have been acquired using-plane wave basis-DFT method implemented in the Cambridge Sequential Total Energy Package (CASTEP, v 8.0) code. Ultrasoft pseudopotentials have been adopted to describe the electron-ion interaction. The procedure Perdew-Burke-Ernzerhof (PBE) [17]constructs the generalized gradient approximation (GGA) functional DFT to express the exchange - correlation energy. Furthermore, to compare the band gap results, the hybrid functional HSE06 [18], with norm-conserving pseudopotentials [19], has also been used.

Fast low energy scanning calculations on $MAPbI_3$, $MAAg_{0.17}Pb_{0.83}I_3$and $MACd_{0.5}Pb_{0.5}I_3$structures have been performed and the cutoff kinetic energies were found to be 400 eV for $MAPbI_3$,400 eV for $MAAg_{0.17}Pb_{0.83}I_3$and 550 eV for $MACd_{0.5}Pb_{0.5}I_3$. After checking convergence criteria, the Monkhorst-Pack of k-points mesh grid were fixed at $7 \times 5 \times 7$for $MAPbI_3$, and at$6 \times 4 \times 5$ for both $MAAg_{0.17}Pb_{0.83}I_3$ and $MACd_{0.5}Pb_{0.5}I_3$ for Brillouin zone sampling. Energy tolerance of 5×10^{-7}eV/atom was set to better probe the calculation. The electronic valence states of each atom are: Pb:5 d^{10} $6s^2p^2$, I:$5s^2p^5$,Ag: 4 d^{10} $5s^1$, Cd:4 d^{10} $5s^2$, C: $2s^22p^2$, N: $2s^22p^2$,H:$1s^1$.

3. Results and discussion

3.1. Structural properties

To study the proposed crystal systems, the equilibrium lattice parameters are calculated using the BFGS method for geometry optimization described in CASTEP [20]. This method allows refining a 3D system to obtain more stable and relaxed structure. Values for the lattice.

Table 1 shows that the calculated lattice parameters of $MAPbI_3$ by (PBE-GGA) method are consistent with literature values [12]. Table 1 also shows that the volumes of $MAAg_{0.17}Pb_{0.83}I_3$ and $MACd_{0.5}Pb_{0.5}I_3$ are contracted along x and y directions, compared to that of $MAPbI_3$. Moreover, the Table shows that incorporating Ag or Cd atoms into $MAPbI_3$ slightly distorts the orthorhombic symmetry to triclinic structures for $MAAg_{0.17}Pb_{0.83}I_3$and $MACd_{0.5}Pb_{0.5}I_3$ (Fig. 1. (b)–(c)). The structures can also be considered approximately orthorhombic as all observed triclinic system angles are close to 90°

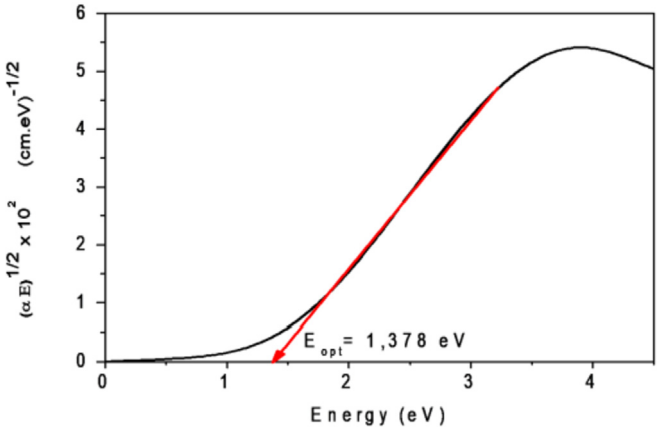

Fig. 2. $MACd_{0.5}Pb_{0.5}I_3$ Tauc plot using PBE-GGA method.

3.2. Electronic properties

3.2.1. Electronic band gap

Since the $MAB_xPb_{1-x}I_3$(B_x = $Ag_{0.17}$ or $Cd_{0.5}$) systems are established in their stable states, their electronic band gaps are computed and shown in Fig. 2. The comparison of the electronic band gap structures of $MAAg_{0.17}Pb_{0.83}I_3$ and $MACd_{0.5}Pb_{0.5}I_3$along high symmetry path directions is presented in the Figure.

Fig. 2 (a) shows that the proposed partial substitutions cause a significant tuning in the perovskite band gap. The band gap value found using PBE-GGA method is widened fromE_g = 1.626eV (for $MAPbI_3$) to 1.732 eV (for $MAAg_{0.17}Pb_{0.83}I_3$)and is narrowed to 0.753eV (for $MACd_{0.5}Pb_{0.5}I_3$). The calculated $MAPbI_3$ band gap value is in congruence with those reported earlier [8,8,12,21,22,29]. Such tuning, confirmed here opens a new scope for new OMHP applications, as described above[24].

The present results show that $MAPbI_3$ total energy (−12500.3816 eV) is comparable to the earlier reported value (−12500.1 eV) [22]. The obtained band gap value of $MAPbI_3$ (1.626 eV) is also consistent with earlier reported value 1.656 eV [22].

Fig. 2 Shows that contrary to the direct band gap for $MAPbI_3$, the $MAAg_{0.17}Pb_{0.83}I_3$ and $MACd_{0.5}Pb_{0.5}I_3$ systems have indirect band gaps for Γ to Q point and D to B point, respectively, where the electronic transition between the valence band (VB) and the conduction band (CB) edges is assisted by phonons [25]. The Figure also shows that Ag^+ ion partial substitution shifts the Fermi level down towards the valence band. Such behavior was reported in earlier literature [14,25]. This explains why $MAAg_{0.17}Pb_{0.83}I_3$ behaves as a p-type semiconductor.

The 50% Cd substitution into $MAPbI_3$drastically narrows the band gap and the result (E_g = 0.753 eV) seems to be anomalous. Therefore, the Tauc plot is useful to calculate the band gap for $MACd_{0.5}Pb_{0.5}I_3$as shown in Fig. 2.

Fig. 2 shows that the optical band gap obtained from Tauc plot E_{opt} = 1.378 eV is incomparable with E_g = 0.753 eV. It is nearly a half band gap reduction.

In addition to the PBE-GGA method, the HSE06 method has been used to calculate the electronic bad gaps for all three compounds. The results are presented in Fig. 3(a) and (b). From Fig. 3, the obtained band gap results of $MAPbI_3$ and $MAAg_{17}Pb_{83}I_3$ using (PBE-GGA) and (HSE06) methods are comparable. While the PBE-GGA method shows band gap values of 1.626 eV (for $MAPbI_3$), 1.732 eV (for $MAAg_{0.17}Pb_{0.83}I_3$) and 0.753 eV (for $MACd_{0.5}Pb_{0.5}I_3$), the HSE06 method shows 1.770 eV (for $MAPbI_3$), 1.694 eV for ($MAAg_{0.17}Pb_{0.83}I_3$) and 1.288 eV (for $MACd_{0.5}Pb_{0.5}I_3$). For $MAPbI_3$ the band gap calculated by HSE06 is 8.85%wider than that calculated using PBE-GGA method. Inversely, for $MAAg_{17}Pb_{83}I_3$, the HSE06 calculated band is 2.2%narrower than the PBE-GGA value. For $MACd_{0.5}Pb_{0.5}I_3$, the HSE06 value is 71% wider than the PBE-GGA value. It should be noted that for the $MACd_{0.5}Pb_{0.5}I_3$ system, the HSE06 value is closer to the Tauc optical band gap value, compared to the PBE-GGA result.

3.2.2. Density of states (DOS)

To investigate the optoelectronic properties of $MAPbI_3$ and $MAB_xPb_{1-x}I_3$ (B=$Ag_{0.17}$ or $Cd_{0.5}$), both total density of states (TDOS) and partial density of states (PDOS) are calculated. Fig. 4 shows that all studied compounds have the same energy distribution trend. The results show that the MA-p states are located at −5 eV, far away from the Fermi level, and have small contribution to the band gap compared to other metallic atoms. The present results confirm the calculated partial density of states (PDOS) values reported earlier [26] that show the negligible MA density of states effect near the band edges. Moreover, MA^+ cation conserves the electronic equilibrium and stability of the structure. It is reported that the interaction between MA^+ cation and $[PbI_3]^{4-}$ framework affects the orbital band compositions and consequently the crystal structure [27]. In all compounds, Pb-6p orbital is the major factor that controls conduction band minima (CBM) [28]. On the other hand, the partial DOS results demonstrate that the valence band is mainly I-5p character from [-2- 0 eV]. Then, a mixture of I-5p with Ag-4d and low Cd-4d orbital density occurs in the band [-2 to −4 eV]. So the Ag^+/Cd^{2+}-4d states have no effect on the energy band gap formation. Approximately, the Pb cation and I anion determine the band gap energy edge positions. The results are in good agreement with literature in Refs. [14,16].

Fig. 4 shows that there is no intense overlapping between Ag-4d/Pb-6p and I-5p on one hand, and between Cd-4d/Pb-6p and I-5p on the other hand. This means weak Ag/Cd/Pb–I bonding [28].

3.2.3. Electronic charge distribution

To further probe intrinsic characteristics of $MAPbI_3$ and $MAB_xPb_{1-x}I_3$ where (B=$Ag_{0.17}$or $Cd_{0.5}$)electronic charge distributions are studied. Fig. 5 shows that MA^+ cation exhibits very weak interactions with Ag, Cd, Pb or I ions. This means negligible overlap between the orbitals of the organic component and inorganic Ag/Cd/Pb–I octahedra. The behavior is observed in all compounds, in congruence with literature [29]. Therefore, the interactions between Ag/Cd/Pb cations and I anion seem to have mostly electrostatic bond character.

3.2.4. Mullikan population analysis

Once the perovskite structure is optimized, assigning partial charges to atoms can be very useful to interpret quantitative partial charges in compounds. Population analysis methods provide valuable insights into interactions that give rise to bonding, where Mulliken's analysis is the most common population analysis method.

Electronic charges of atoms, based on Mullikan population of Ag/Cd/Pb–I bonding, are summarized in Table 2. The Table shows the partial charges on each atom involved in Ag/Cd/Pb–I bonding. The iodine I atom, with higher electronegativity, attracts electrons from Ag, Cd or Pb atoms leaving them positively charged.

Approximately, the I^- anion and Pb^{2+}cation preserve the same charges in two compounds. Table 2 also shows that Cd is the cation with highest ability to share the electronic charge (+0.24 e) compared to Ag (+0.37 e) and Pb (+0.74 e) due to its lower electronegativity (or higher electropositivity). Electropositivity describes the tendency of an element to lose one or more electrons. Electropositive elements therefore tend to form positive ions. They donate electrons to other species and in doing so act as reducing agents. Metals are characterized by their electropositivity, where alkali metals are known to behave as reducing agents.

3.2.5. Effective masses

In this study, the anisotropic effective masse (m^*) of electrons (m_e^*) and holes (m_h^*) along principal directions are analytically obtained. This has been achieved by the parabolic approximation where the holes or

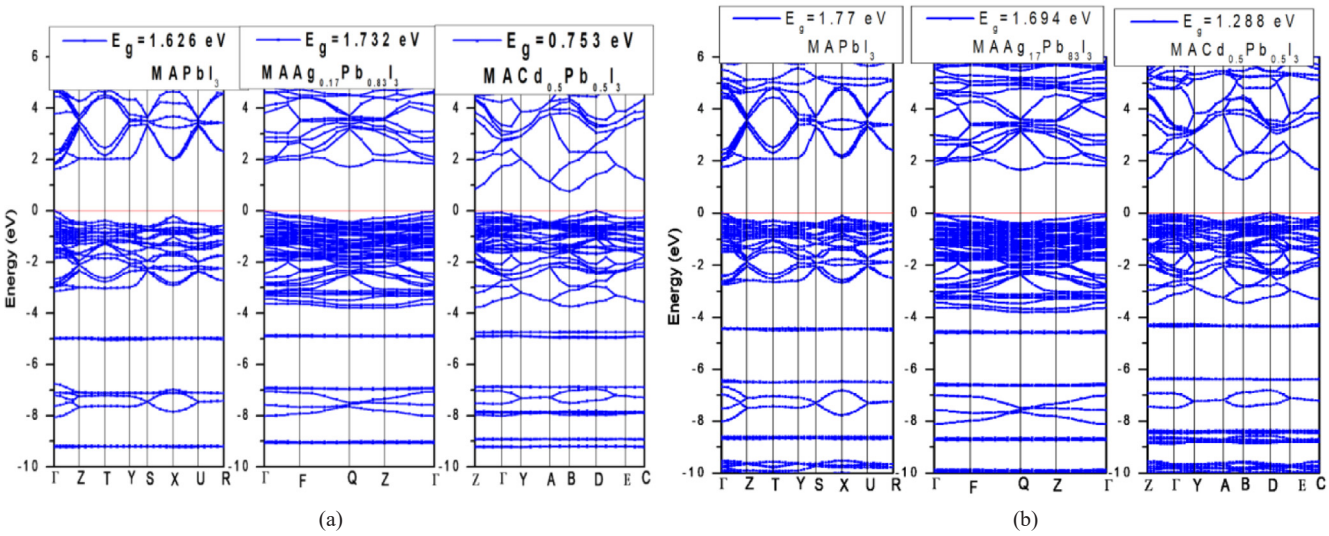

Fig. 3. Electronic band gap structures of $MAPbI_3$, $MAAg_{17}Pb_{83}I_3$and $MACd_{0.5}Pb_{0.5}I_3$using (a) (PBE-GGA) and (b) (HSE06) method.

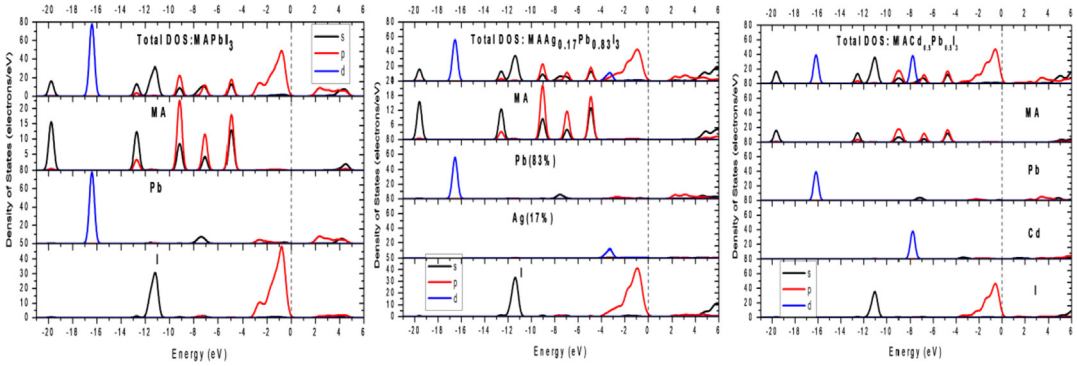

Fig. 4. Total and partial density of states (TDOS and PDOS) for $MAPbI_3$,$MAAg_{0.17}Pb_{0.83}I_3$ and $MACd_{0.5}Pb_{0.5}I_3$.

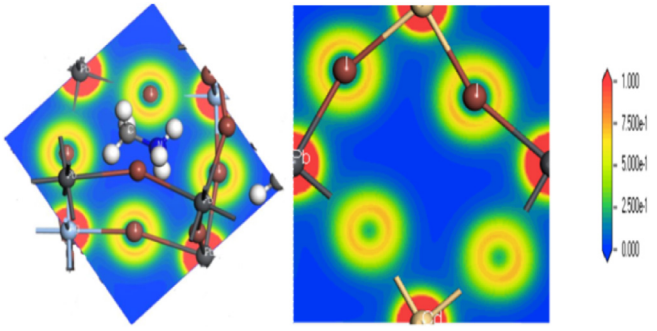

Fig. 5. Electron charge distribution for (a) $MAAg_{17}Pb_{83}I_3$ and (b) $MACd_{0.5}Pb_{0.5}I_3$ ranging (from 0 to 1e/Å^3).

electrons should exist at the top and bottom of the valence and conduction bands, respectively.where*E(k)*is the energy dispersion Eigen state.

The effective mass results of holes and electrons are shown in Table 3.

The PBE-GGA method is adopted to calculate effective masses for $MAPbI_3$, $MAAg_{0.17}Pb_{0.83}I_3$ due to the band gap similarity compared to that obtained with HSE06 method. For $MACd_{0.5}Pb_{0.5}I_3$, the result is obtained using HSE06 energy dispersion. In the Table, m0 refers to electron mass.

Table 3 shows that all compounds are characterized by their low effective masses. The anisotropy also affects strongly the charge carrier (electron or hole) inside the perovskites.

3.3. Optical properties

The optical properties of orthorhombic $MAAg_{0.17}Pb_{0.83}I_3$, $MACd_{0.5}Pb_{0.5}I_3$and $MAPbI_3$ should be anisotropic due to their asymmetry. The anisotropy is taken into account in the calculations by considering all different polarization directions of the electromagnetic field.

As depicted in Fig. 6, $MACd_{0.5}Pb_{0.5}I_3$ behaves differently when interacting with photons along x and z directions where the absorption peaks occur at 4.3 eV on one hand, and along y direction where the peak occurs at 3.5 eV on the other hand. Moreover, the absorption character along y direction resembles that of $MAPbI_3$, or $MAAg_{0.17}Pb_{0.83}I_3$.

To have in thoughts about the absorption through the partial Ag/Cd substitution, a comparative presentation is shown in Fig. 7. The Figure shows that $MAPbI_3$ exhibits broad and high light absorbance ($\alpha = 10^4$ - $10^5 cm^{-1}$) over the visible spectrum [1.65–3.26 eV: 750-380 nm], followed by $MAAg_{0.17}Pb_{0.83}I_3$ ($\alpha = 10^4$–$0.6 \times 10^5 cm^{-1}$) and a smaller value for $MACd_{0.5}Pb_{0.5}I_3$ with ($\alpha = 1.5 \times 10^4 - 0.4 \times 10^5 cm^{-1}$). All in all, $MAPbI_3$ is still the appropriate absorber and can be recommended for thin film photovoltaic applications.

3.3.1. Absorption coefficient

Fig. 6 shows the optical absorption coefficient values for $MAPbI_3$,$MAAg_{0.17}Pb_{0.83}I_3$ and $MACd_{0.5}Pb_{0.5}I_3$ along all polarization

Table 1
Calculated (DFT) and lattice parameter values for $MAPbI_3$, $MAAg_{0.17}Pb_{0.83}I_3$ and $MACd_{0.5}Pb_{0.5}I_3$.

Compound	Calculated lattice parameters a,b,c (Å),V (Å^3), (α,β,γ$^\circ$)	Literature experimental value (Ref) a,b,c (Å),V (Å^3), (α,β,γ$^\circ$)
$MAPbI_3$	a = 8.848,b = 12.928,c = 9.136 α = β = γ = 90° V = 1045.116.	a = 8.861, b = 12.62, c = 8.581. α = β = γ = 90° [12] [12]V = 959.5
$MAAg_{0.17}Pb_{0.83}I_3$	a = 8.466,b = 12.78,c = 9.141. α = 89.46°, β = 90.267°, γ = 90.119° V = 989.	
$MACd_{0.5}Pb_{0.5}I_3$	a = 8.568,b = 12.729,c = 9.23 α = 89.978°, β = 90.451°, γ = 89.987° V = 1006.8	

Parameters (a × b × c), (α,β,γ) and the volume V of $MAPbI_3$, $MAAg_{0.17}Pb_{0.83}I_3$ and $MACd_{0.5}Pb_{0.5}I_3$ are shown in Table 1.

Table 2
Calculated Mulliken atomic population charges in Ag/Cd/Pb–I bonding.

$$m^* = \hbar^2\left(\partial^2 E(k)\Big/\partial k^2\right)^{-1} \quad (3)$$

Compound	Ion	Mullikan atomic population	Ion number
$MAAg_{0.17}Pb_{0.83}I_3$	I (1)	−0.44	4
	I (2)	−0.22	2
	I (3)	−0.39	2
	I (4)	−0.19	2
	I (5)	−0.15	2
	Pb	+0.74	2
	Ag	+0.37	2
$MACd_{0.5}Pb_{0.5}I_3$	I (1)	−0.35	4
	I (2)	−0.33	4
	I (3)	−0.41	2
	I (4)	−0.14	2
	Pb	+0.74	2
	Cd	+0.24	2

The effective mass model is defined by the equation.

Table 3
Anisotropic effective masses of $MAPbI_3$ $MAAg_{0.17}Pb_{0.83}I_3$ $MACd_{0.5}Pb_{0.5}I_3$ using PBE-GGA and HSE06 methods.

Compound	Method	m^*_h/m_0	m^*_e/m_0
$MAPbI_3$	PBE-GGA	m^*_x = 0.127	m^*_x = 0.18
		m^*_y = 0.06	m^*_y = 0.084
		m^*_z = 0.11	m^*_z = 0.167
$MAAg_{0.17}Pb_{0.83}I_3$	PBE-GGA	m^*_x = 0188	m^*_x = 0.188
		m^*_y = 0.39	m^*_y = 0.082
		m^*_z = 0.077	m^*_z = 0.16
$MACd_{0.5}Pb_{0.5}I_3$	HSE06	m^*_x = 0.095	m^*_x = 0.1
		m^*_y = 0.043	m^*_y = 0.045
		m^*_z = 0.082	m^*_z = 0.085

directions. The Figure shows the tendency:α($MAPbI_3$) = 1.07 × $10^5 cm^{-1}$>α($MAAg_{0.17}Pb_{0.83}I_3$) = 0.8 × $10^5 cm^{-1}$ >α($MACd_{0.5}Pb_{0.5}I_3$) = 0.7 × $10^5 cm^{-1}$. For this reason, $MAPbI_3$is being considered as absorber in thin film solar cells [30]. Its absorption coefficient value is greater than those observed in conventional PV inorganic p-n junction materials such as $CuInGaSe_2$, CdTe and GaAs, as described earlier [12].

Fig. 6 also shows that $MAPbI_3$, and $MAAg_{0.17}Pb_{0.83}I_3$ exhibit the same α trend and remain isotropic in all polarization directions over the visible range [1.65–3.1 eV]. On the other hand, the anisotropy slightly affects the photon absorption in $MAAg_{0.17}Pb_{0.83}I_3$ in the near and mid ultraviolet range [3.1–5.0 eV] along all polarization directions. Highest absorption values are observed along z (001) direction for all compounds. Like $MAPbI_3$, the 17% Ag doped system exhibits highest absorption peak at the same energy (3.6 eV).

3.3.2. Dielectric constant

The dielectric constant (relative permittivity) is a property that describes the ability of a medium to store electric field during dipole polarization. It is expressed as: $\varepsilon = \varepsilon' - i\varepsilon''$, where the real part ε' represents the charge storage ability and the imaginary part ε'' represents the energy loss. The electronic polarization characterizes the dielectric process at optical (ultrahigh) frequencies. The real and imaginary parts of dielectric constant values for $MAAg_{0.17}Pb_{0.83}I_3$, $MAPbI_3$and $MACd_{0.5}Pb_{0.5}I_3$ are illustrated in Fig. 8 (a)–(b). The figures show that all compounds have the same dielectric constant character and the same order of values in the visible spectrum. The $MAPbI_3$ has $\varepsilon'_{opt} = 7$ and $\varepsilon'' = 7.5$, in congruence with literature [31]. From Fig. 8(a and b), it is noted that doping $MAPbI_3$ with 17% Ag increases the dielectric real part, ε' to 8.2 and lowers the dielectric imaginary part ε'' to 6.5.

Fig. 8 shows that the $MACd_{0.5}Pb_{0.5}I_3$ has exception where the anisotropy affects the dielectric behavior along x and z polarization directions. It is also noted that outside the visible band all compounds suffer the anisotropy effect. The high dielectric constant values are observed along the z direction for both the real part and the imaginary part. Moreover, the Cd doped system maintains the same storage ability of $MAPbI_3$($\varepsilon'_{opt} = 7$), whereas loss lowering occurs along the y direction ($\varepsilon'' = 5.5$) and along both the x and z directions ($\varepsilon'' = 4$).

3.3.3. Refractive index

The refractive index (n) values in different polarization directions are shown in Fig. 9 (a), while the values of extinction coefficient are shown in Fig. 9 (b). The Figures show that the $MAPbI_3$, $MAAg_{0.17}Pb_{0.83}I_3$and $MACd_{0.5}Pb_{0.5}I_3$ behave similarly, with the exception in $MACd_{0.5}Pb_{0.5}I_3$ trend along x and z directions when interacting with the incident electromagnetic field. Moreover, the anisotropy influences each of these materials when responding to such specific polarization outside the visible spectrum.

For comparison purposes, Fig. 9(a and b) show that the 17% Ag doped system exhibits slightly increased reactive index n from 2.75 to 2.9 but inversely decreased wave attenuation or extinction coefficient κ (Im (n))from 1.8 to 1.4. Fig. 9(a) shows that $n_{MAAg0.17Pb0.83I3} > n_{MAPbI3} > n_{MACd0.5Pb0.5I3,}$ with highest value n = 2.9 observed for $MAAg_{0.17}Pb_{0.83}I_3$. The calculated values are comparable to literature [32], keeping in mind that the present results specifically describe orthorhombic $MAPbI_3$ source. Incorporating 50% Cd into $MAPbI_3$ maintains the high refractive index peaks n = 2.5 at 2.5 eV and 3.5 eV as in $MAPbI_3$, whereas the extinction coefficient κ is decreased from κ = 1.8 in $MAPbI_3$ to κ = 1.2, 1.1 and 1.0 along y,z and x directions, respectively, for the doped system.

Collectively, the study shows that partial substitution of lead ion in $MAPbI_3$ may affect its optoelectronic properties without changing the crystal structure itself. The Ag^+ ion increases the refractive index value by increasing the real part and decreasing the imaginary part. The band gap value is widened which makes the doped system suitable for visible light absorption. For the system substituted with Cd^{2+} ions, the study came out with more accurate optoelectronic property values reported in

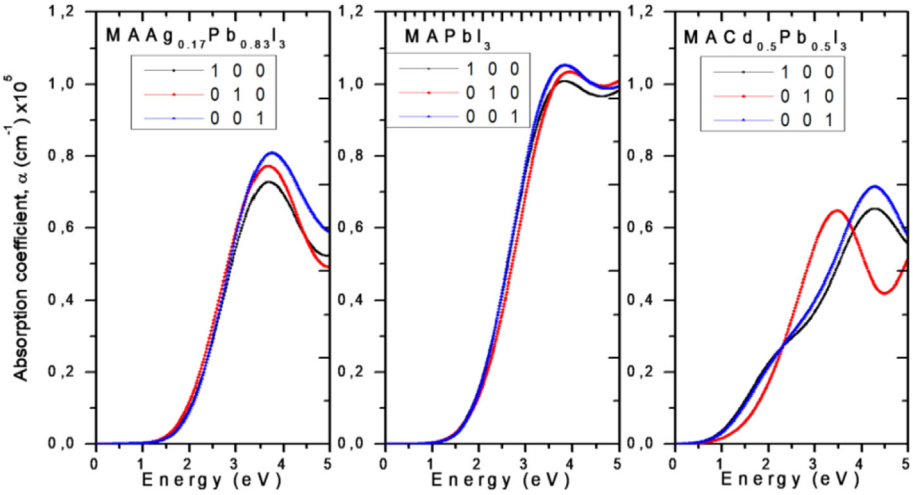

Fig. 6. Optical absorption coefficient(α) values for $MAAg_{0.17}Pb_{0.83}I_3$, $MAPbI_3$ and $MACd_{0.5}Pb_{0.5}I_3$ in different polarization directions.

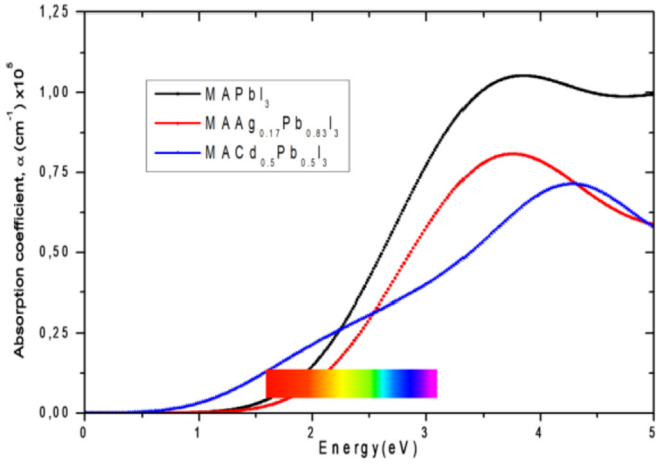

Fig. 7. Comparison of optical absorption coefficient, α values for $MAAg_{0.17}Pb_{0.83}I_3$, $MAPbI_3$ and $MACd_{0.5}Pb_{0.5}I_3$ at (001) polarization direction using PBE method.

earlier literature for $MACd_{0.5}Pb_{0.5}I_3$and $MACdI_3$[15] [23]. Investigating different substituent concentrations, to reach optimal compositions with best optoelectronic properties for solar cell manufacturing based on $MAAB_xPb_{1-x}I_3$, is underway in these laboratories, together with stabilizing effect of elemental partial substitution. Optimized substituent concentration for various elements is also worth to investigate.

4. Conclusion

$MAPbI_3$and $MAB_xPb_{1-x}I_3$(B_x = $Ag_{0.17}$or $Cd_{0.5}$) perovskites at their orthorhombic phase are basically described here, using DFT (PBE-GGA and HSE06) methods implemented in CASTEP. These sub families of perovskites are absorber materials, so their optoelectronic and properties are calculated. For $MAAB_xPb_{1-x}I_3$(B = 0.17Ag or 0.5Cd) group, the substitution of 17% Ag and 50% Cd concentrations into $MAAPbI_3$contracts the sizes of the new $MAAB_{0.17}Pb_{0.83}I_3$and $MAAB_{0.5}Pb_{0.5}I_3$perovskites.The results also show that partial substitution with Ag and Cd tunes the energy band gap. The obtained band gaps using different methods are comparable for $MAPbI_3$, E_g (PBE) = 1.620 eV and E_g (HSE06) = 1.77 eV and for $MAB_{0.17}Pb_{0.83}I_3$where E_g (PBE) = 1.732 eV and E_g (HSE06) = 1.694 eV.The calculated values for $MACd_{0.5}Pb_{0.5}I_3$are inconsistent, with E_g (PBE) = 0.753 eV and E_g (HSE06) = 1.288, albeit the HSE06 result better fits with Tauc plot optical band gap valueE_{opt} = 1.378 eV.

Furthermore, (MA^+)has no significant effect on bonding charge distribution that strongly occurs by Pb-6p andI-5p atomic orbitals in all

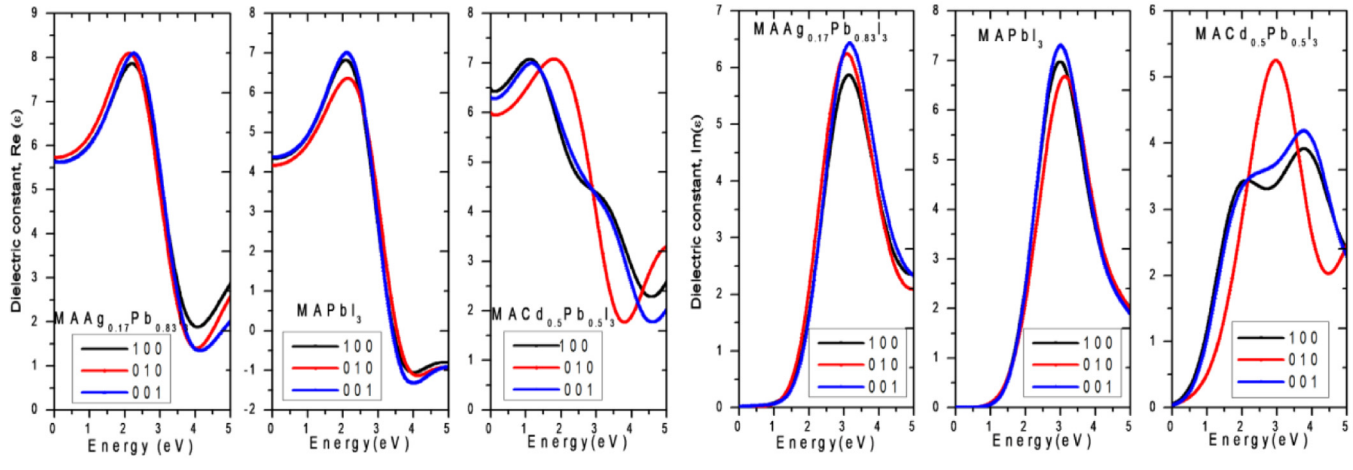

Fig. 8. Dielectric constant values (a) Re(ε) and (b) Im (ε) for$MAAg_{0.17}Pb_{0.83}I_3$, $MAPbI_3$and $MACd_{0.5}Pb_{0.5}I_3$ along different polarization directions.

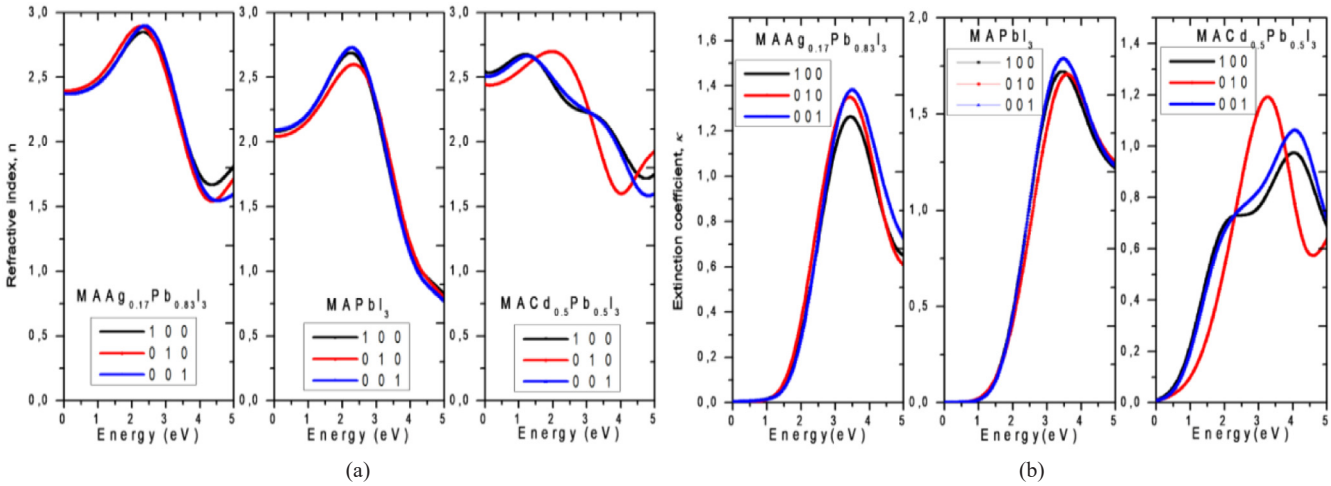

Fig. 9. Plots showing values of (a) Refractive index n and (b) extinction coefficient κ for $MAAg_{0.17}Pb_{0.83}I_3$, $MAPbI_3$ and $MACd_{0.5}Pb_{0.5}I_3$ along different polarization directions.

compounds. The results show that $MAPbI_3$ has the widest band and highest absorption coefficient ($10^5 cm^{-1}$) in the visible range [1.65–3.26 eV: 350–780 nm] compared to the other perovskites. $MAPbI_3$ exhibits broad and high light absorbance ($\alpha = 10^4$ - $10^5 cm^{-1}$) over the visible spectrum [1.65–3.26 eV: 380–750 nm], followed by $MAAg_{0.17}Pb_{0.83}I_3$ ($\alpha = 10^4$–$0.6 \times 10^5 cm^{-1}$) and least for $MACd_{0.5}Pb_{0.5}I_3$ ($\alpha = 1.5 \times 10^4 - 0.4 \times 10^5 cm^{-1}$).

The study shows that low anisotropic electron and hole effective masses characterize all compounds in the range of 0.043 m_o-0.188 m_o. In addition, the anisotropy slightly affects the optical properties, particularly $MAAPbI_3$and $MAAB_{0.17}Pb_{0.83}I_3$in the near and mid ultraviolet range [3.1–5.0 eV] but differently influences the $MAAB_{0.5}Pb_{0.5}I_3$ optical properties such as the absorption coefficient α, the dielectric constant ε and the refractive index n along x and z directions. Finally, the 17% Ag^+ substitution into the $MAAPbI_3$increases the refractive index (Re (n)) and decreases the extinction coefficient (Im (n) = κ). The observed n values are 2.90, 2.75 and 2.00 for $MAAg_{0.17}Pb_{0.83}I_3$, $MAPbI_3$ and $MACd_{0.5}Pb_{0.5}I_3$, respectively, at 2.5 eV energy peak value. The observed κ values are 1.4, 1.8, and 1.2 for $MAAg_{0.17}Pb_{0.83}I_3$, $MAPbI_3$ and $MACd_{0.5}Pb_{0.5}I_3$, respectively, at 3.5 eV energy peak value.

Conflicts of interest

This work carries no conflicts of interests.

Acknowledgment

Financial support by Université Amar Telidji de Laghouat, Algérie, is acknowledged.

References

[1] P. Kanhere, S. Chakraborty, C.J. Rupp, R. Ahujabd, Z. Chen, Substitution induced band structure shape tuning in hybrid perovskites ($CH_3 NH_3Pb_{1-x}Sn_xI_3$)for efficient solar cell applications, RSC Adv. 5 (2015) 1 07497.
[2] P.F. Ndione, Z. Li, K. Zhu, Effects of alloying on optical properties of organic-inorganic lead halide perovskite thin films, J. Mater. Chem. C 4 (2016) 7775–7782.
[3] Y. Zhou, F. Wang, H.H. Fang, M.A. Loi, F.Y. Xie, N. Zhoa, C.P. Wong, Distribution of bromine in mixed iodide-bromide organo-lead perovskites and its impact on photovoltaic performance, J. Mater. Chem. 4 (2016) 16191–16197.
[4] Y. Hsiao, T. Wu, M. Li, Q. Liu, W. Qin, B. Hu, Fundamental physics behind high efficiency organometal halide perovskite solar cells, J. Mater. Chem. 3 (2015) 15372.
[5] J. Chen, S. Zhou, S. Jin, T. Zhai, Crystal organometal halide perovskites with promising optoelectronic applications, J. Mater. Chem. C 4 (2015) 11–27.
[6] B. Qing, W. Wei, Y. Zhou, Y. Dong, Photoelectric performance and stability comparison of $MAPbI_3$ and $FAPbI_3$ perovskites solar cells, Sol. Energy 174 (2018) 933–939.
[7] D. Liu, S. Li, F. Bian, X. Meng, First principles investigation on the electronic and mechanical properties of Cs-doped CH3NH3PbI3, Materials 11 (2018) 1141.
[8] C. Quarti, E. Mosconi, J.M. Ball, V. D'Innocenzo, C. Tao, S. Pathak, H.J. Snaith, A. Petrozza, F.D. Angelis, Structural and optical properties of methylammonium lead iodide across the tetragonal to cubic phase transition: implications for perovskite solar cells, Energy Environ. Sci. 9 (2015) 155–163.
[9] T.B. Song, Q. Chen, H. Zhou, C. Jiang, H.H. Wang, M. Yang, Y.S. Liu, J. You, Y. Yang, Perovskite solar cells: film formation and properties, J. Mater. Chem. 3 (2015) 9032–9050.
[10] J.S. Manser, J.A. Christians, P.V. Kamat, Intriguing optoelectronic properties of metal halide perovskites, Chem. Rev. 116 (2016) 12956–13008.
[11] Q. Chen, N.D. Marco, Y. Yang, T.B. Song, C.C. Chen, H. Zhao, Z. Hong, H. Zhou, Y. Yang, Under the pot light: the organic-inorganic hybrid halide perovskite for optoelectronic applications, Nano Today 10 (2015) 355–396.
[12] X. Liu, W. Zhao, H. Cui, Y. Xie, Y. Wang, T. Xu, F. Huang, Organic-inorganic halide perovskite based solar cells - revolutionary progress in photovoltaics, Inorg. Chem. Front. 2 (2012) 315–335.
[13] J. Chang, H. Chen, H. Yuan, B. Wang, X. Chen, The mixing effect of organic cations on structural, electronic and optical properties of $FA_xMA_{1-x}PbI_3$perovskites, Phys. Chem. Chem. Phys. 20 (2017) 941–950.
[14] S. Zhou, Y. Ma, G. Zhou, X. Xu, M. Qin, Y. Li, Y. Hsu, H. Hu, G. Li, N. Zhao, J. Xu, X. Lu, Ag-doped halide perovskite nanocrystals for tunable band structure and efficient Charge transport, ACS Energy Lett. 4 (2019) 534–541.
[15] L. Jiang, T. Wu, L. Sun, Y. Li, A. Li, R. Lu, K. Zou, W. Deng, First principles screening of lead-free methylammonium metal iodine perovskites for photovoltaic application, J. Phys. Chem. C 44 (2017) 24395-24364.
[16] L. Zhang, J. Wang, J. Wu, M.S. iLong, F. Zou, Z. Gao Y, Crystal structure, optical behavior and electrical conduction of the new organic–inorganic compound $CH_3NH_3CdI_3$, J. Mater. Sci. Mater. Electron. 12 (2018) 9821–9828.
[17] J.P. Perdew, K. Burke, M. Ernzerhof, Generalized gradient approximation made simple, Phys. Rev. Lett. 77 (1996) 3865–3868.
[18] A.V. Krukau, O.A. Vydrov, A.F. Izmaylov, G.E. Scuseria, Influence of the exchange screening Parameter on the performance of screened hybrid functional, J. Chem. Phys. 125 (2006) 224106.
[19] N. Troullier, J.L. Martins, Efficient pseudopotentials for plane-wave calculations, Phys. Rev. B 43 (1991) 1993–2006.
[20] B.G. Pfrommer, M. Côté, S.G. Louie, M.L. Cohen, Relaxation of crystals with the quasi-Newton method, J. Comput. Phys. 13 (1997) 233–240.
[21] J. Cui, H. Yuan, J. Li, X. Xu, Y. Shen, H. Lin, M. Wang, Recent progress in efficient hybrid lead halide perovskite solar cells, Sci. Technol. Adv. Mater. 16 (2015) 036004.
[22] D. Ji, X.J. Xiao, C.M. Zhang, X.L. Liy, M.Z. Hu, Yin, Regulatory band gap of vacancy at the B sites in $CH_3NH_3Pb_{1-x}I_3$perovskite, Mod. Phys. Lett. B 30 (2016) 23.
[23] Y. Zhang, J. Feng, $CH_3NH_3Cd_{0.875}Pb_{0.125}I_3$ perovskite as potential photovoltaic materials, AIP Adv. 6 (2016).
[24] T.J. Jacobsson, J.P. Correa-Baena, M. Pazoki, M. Saliba, K. Schenk, M. Grätzel, A. Hagfeldt, An exploration of the compositional space for mixed lead halogen perovskites for high efficiency solar cells, Energy Environ. Sci. 9 (2016) 1706–1724.
[25] Q. Chen, L. Chen, F. Ye, T. Zhao, F. Tang, A. Rajagopal, Z. Jiang, S. Jiang, Y. Jen A, Y. Xie, J. Cai, L. Chen, Ag-incorporated organic-inorganic perovskite films and planar heterojunction solar cells, Nano Lett. 5 (2017) 3231–3237.
[26] Y. Ye, X. Run, X.H. Tao, H. Feng, X. Fei, W.L. Jun, Nature of the band gap of halide perovskites ABX_3(A = CH_3NH_3,Cs; B= Sn, Pb; X = Cl, Br, I): first-principles calculations, Chin. Phys. B 24 (2015) 11. 116302.
[27] M. Mladenovic, N. Vukmirovic, Effects of thermal disorder on electronic structure of halide perovskites: insights from MD simulations, Phys. Chem. Chem. Phys. 20 (2018) 25693–25700.
[28] W.J. Yin, J.H. Yang, J. Kang, Y. Yan, S.H. Wei, Halide perovskite materials for solar

cells: a theoretical review, J. Mater. Chem. 3 (2014) 8926–8942.
[29] R.A. Jishi, O.B. Ta, A.A. Sharif, Modeling of lead halide perovskites for photovoltaic applications, Cond. Mat. 49 (2014) 28344–28349.
[30] S.D. Wolf, J. Holovsky, S.J. Moon, P. Löper, B. Niesen, M. Ledinsky, F.J. Haug, J.H. Yum, C. Ballif, Organometallic halide perovskites: sharp optical absorption edge and its relation to photovoltaic performance, J. Phys. Chem. Lett. 5 (2014) 1035–1039.
[31] Z. Fan, K. Sun, J. Wang, Perovskites for photovoltaics: a combined review of organic-inorganic halide perovskites and ferroelectric oxide perovskites, J. Mater. Chem. 3 (2015) 18809–18828.
[32] A.M.A. Leguy, P. Azarhoosh, M.I. Alonso, M.C. Quiles, O.J. Weber, J. Yao, D. Bryant, M.T. Weller, J. Nelson, A. Walsh, M. VSchilfgaarde, P.R.F. Barnes, Experimental and theoretical optical properties of methylammonium lead halide perovskites, Nanoscale 8 (2016) 6317.